Accurate Computation of Steady Nonlinear Free-Surface Flows

David C. Scullen,
B.Sc. (Adelaide), Dip.Comp.Inf.Sci. (S.A.)

Thesis submitted for the degree of
Doctor of Philosophy
in
Applied Mathematics
at
The University of Adelaide
(Faculty of Mathematical and Computer Sciences)

Department of Applied Mathematics

SUB CRUCE LUMEN

February, 1998

To my parents.

ACKNOWLEDGEMENTS

I wish to thank Professor E.O. Tuck for his supervision throughout the course of my Ph.D. studies. His supervisory style has encouraged my independence, allowing me to pursue the research topics which I find most interesting, and has resulted ultimately in a greater sense of personal achievement. While allowing my freedom, it was always clear to me that he could be relied upon for advice, collaboration and support.

It has been a pleasure to be a part of the fluid-dynamics think tank that inhabited Room 110. The occupants have, over the years, included Dr. Whye Teong Ang, Mr. Leo Lazauskas, Dr. David Standingford, Miss Yvonne Stokes, and Mr. Leo Wiryanto, all of whom have been great to work with, the sources of many lively conversations, and much fun.

Thanks also to Professor R.F. Beck of the University of Michigan for the many discussions we shared while he visited during the last months of 1995. He was the source of a wealth of practical knowledge, and gave considerable direction to my work on submerged spheroids.

Thanks also to the people of the Department of Applied Mathematics at the University of Adelaide. In particular, I would like to thank the Departmental Head, Dr. Peter Gill, for his genuine interest and encouragement. His helmsmanship has been fundamental to fostering within the department an atmosphere in which it is a pleasure to study and work.

Extra special thanks go to my parents and siblings, for the encouragement and support that they have given to me over the years.

While studying for this Ph.D., I was in receipt of a University of Adelaide Scholarship, with some additional funding provided from an Australian Research Council grant held by Professor Tuck.

This work contains no material which has been accepted for the award of any other degree or diploma in any university or other tertiary institution and, to the best of my knowledge and belief, contains no material previously published or written by another person, except where due reference has been made in the text.

I consent to this copy of my thesis, when deposited in the University Library, being available for loan and photocopying.

12/2/98

CONTENTS

ABSTRACT

A method of solution of steady-state nonlinear free-surface potential-flow problems is presented. The effects of various parameters on the speed and reliability of the method and the accuracy of the solutions are investigated. The method is subsequently applied to several problems involving flows around submerged bodies, and the results are presented.

Specifically, a distribution of discrete sources located external to the fluid domain is used to represent the velocity potential. An iterative procedure is employed which successively refines approximations to the free surface and potential until the desired solution is obtained. The iterative procedure demonstrates a quadratic rate of convergence.

Parameters of choice, such as resolution of the free surface discretisation, location of singularities, formulation and application of the radiation condition, length of computational domain, formulation of the applied boundary condition, selection of surface-update procedure, the scheme for shifting singularities between iterations, and the test of convergence, are investigated for their effects on accuracy, reliability and speed. Recommendations are made for the selection of each of these parameters.

To verify the accuracy and utility of the method, it is applied to flows about submerged bodies. The wave-making properties of circular cylinders, both with and without circulation, are investigated. Emphasis is placed on the choices of circulation that significantly reduce the amplitude of the waves produced. Two circular cylinders are considered in tandem, and the special choices of depth of submergence and separation for which each cylinder is free of horizontal force are determined.

In three-dimensional flow, the wave-making of a prolate spheroid is investigated. Observations of the change in wake pattern with speed are made, and a quantitative investigation of the forces is undertaken. Some interesting cases, where the waves produced are steep and the submergence of the body is shallow, are shown. Flows about spheres and spheroids in a fluid of finite depth are then considered. Some interesting phenomena, including the widening of the wake, are observed. Comparison is made to the corresponding semi-infinite fluid cases, as well as to the appropriate linear theories. In each instance, the nonlinear effects produced by increasing body size are discussed.

INTRODUCTION

1.1 MOTIVATION

The present is a period in mathematical history when the possibility of accurately computing nonlinear free-surface flows is becoming realised. Before the advent of the computer, only theories involving significant simplification were available. These were the works of talented mathematicians, expert in the tools of their day, and were mostly analytic in nature. Indeed, these very same mathematicians were often stymied by their inability to numerically evaluate, with any great accuracy, the conclusions for which their theories and formulae held the key. Men of such great mathematical calibre include Bernoulli, Euler, Kelvin, Rayleigh, and Lamb, whose investigations into fluid dynamics laid the cornerstone from which we are now able to build our understanding.

Today, at least for some of us, an essential tool is the computer. We are able to concentrate on developing methods that solve more realistic problems, and as a fruit of our labour, results are produced which can be used in design and development. The advantages claimed of such an approach include that the time required for, and financial cost of, physical experimentation can be reduced significantly. It is in this context that the content of this thesis is best considered.

The overall intention has been to develop a numerical method, computer software, and the associated understanding, with which nonlinear free-surface flows can be accurately determined. Although the fundamental concepts have been around for a few decades, computers with the capacity to solve realistic problems in a timely manner are only just beginning to exist.

The age has come where significant amounts of investigation into the solution of such problems is feasible. Methods can be developed which, although they may currently be limited by computing capabilities, will in the near future, be speedy, economical and common-place. It is in this endeavour, it is hoped, that the current work contributes.

1.2 THE PROBLEM CLASS IN CONTEXT

The study of fluid dynamics is of major practical importance. So much of the world in which we live can be described under this heading. The complex interaction of weather systems is one example. Everyday forecasts, including storm warnings which are essential for safe sea and air transport, and other warnings including those of natural disasters such as cyclones and flood-causing rains, are dependent upon our understanding of fluid dynamics. Long-term weather prediction will, in the near future, be used when determining agricultural strategies, such as which crop should be planted in which future year, and when a given pasture should be spelled for rejuvenation. Forecasts are already being used to make estimates of the effects of global warming. Similarly, periodic changes in weather patterns, such as El Niño, will be predicted with greater certainty, perhaps allowing for strategies that will reduce the effects of the droughts and floods which it simultaneously produces in different regions of the world. Meteorological observations, coupled with an appropriate understanding of fluid dynamics, can be used to predict the likely courses of bush fires and oil slicks, and consequently aid in their containment.

The impact of a dam on river flow, both upstream and downstream, has important repercussions for water quality. The reduction of water pressure and supply due to the depletion of natural ground water resources, such as Australia's great artesian basin, have an influence on our ability to inhabit land that is remote from any other natural water supply.

Many industrial manufacturing processes, including injection moulding of plastics and the uniform reduction of iron to steel, draw largely upon fluid dynamics. With the increase in understanding of the undesirable side-effects of fossil-fuel use, more emphasis is being placed upon harvesting energy from both wind and water sources. Apparatus of greater efficiency are required for this task. Naturally, fluid dynamic effects are paramount in the design of aircraft, and of great importance in the design of watercraft. The associated techniques can aid in the design of better valves for use in an artificial heart.

Even pleasurable activities, such as sailing, surfing, golf and kite-flying, can be based upon the properties of fluids.

These are all examples of the ways in which we are touched every day by the physical laws that govern the motion of fluids. So, it is of little wonder that much effort has been given to the study of fluid dynamics in general.

Clearly, phenomena of such variety have properties that differ considerably, and are therefore described best in terms of different models. If the fluid is assumed to be inviscid, incompressible and of constant density, and the flow is assumed to be irrotational then the governing equations simplify to Laplace's equation. The simplification is significant, since much is known about methods with which Laplace's equation can be solved.

Any flow is, of course, subject to certain other conditions. If the flow is past or along an impermeable body, then the appropriate condition states that the fluid moves along the surface of the body, rather than through it. On a free surface, such as an air-water interface, two physical conditions are to be satisfied. Firstly, there is the kinematic boundary condition, which plays the same rôle as the body boundary condition. Secondly, the dynamic free-surface boundary condition prescribes the pressure distribution on the surface. In many cases, a realistic simplification is that the pressure is constant (that is, atmospheric) everywhere.

Flows with this formulation are in general unsteady, with the particles' motions being dependent upon time. Problems of interest that can be described under these assumptions include the motion of liquids in tanks (for example, oil, liquid chemicals or water being transported by truck and trailer), and the forces acting upon bodies in a system of waves (for example, those acting on the superstructure of a deep-sea oil rig, or the rolling motions of a sea-going vessel).

A further simplification of practical importance is that of the existence of a frame of reference in which the motion is seen to be steady. Such flows occur in the real world due to either bodies at rest in a stream, such as for the pylons of a bridge over a river, or for bodies moving with a constant speed and direction in an otherwise motionless body of water, such as ships and submarines. The particular solution that is usually of interest in these flows is the one for which there are not any waves far upstream of the disturber. It is this class of problems that will be considered in this thesis.

Specifically then, the flows being considered here can be described by the set of equations:

$$\begin{aligned}
\nabla^2\phi &= 0 && \text{in the fluid,} && (1.1)\\
\underset{\sim}{\nabla}\phi.\underset{\sim}{n} &= 0 && \text{on the body,} && (1.2)\\
\underset{\sim}{\nabla}\phi.\underset{\sim}{n} &= 0 && \text{and} && (1.3)\\
p &= 0 && \text{on the free surface, and} && (1.4)\\
\underset{\sim}{\nabla}\phi &\to U && \text{upstream.} && (1.5)
\end{aligned}$$

Here, ϕ represents the velocity potential, p is the pressure in excess of atmospheric, and U is the speed of the stream.

1.3 POSSIBLE METHODS OF SOLUTION

The class of problems can be attacked with a wide variety of approaches. One is to assume the perturbation of the free-surface from the plane is small, allowing for the implementation of a linearised boundary condition which is to be satisfied on the plane. Under this assumption, analytic results can been obtained for some simple geometries. Havelock [19] made extensive use of this method. However, the practical range of applications is limited, since the investigations often lead to integral equations which, without the aid of computational facilities, are difficult to solve. Never-the-less, analytic methods form the basis for the numerical solution procedures that are used now.

A conceptually simple method of numerical solution involves the discretisation of the entire fluid domain, as in finite-volume methods. However, significant simplifications can be made if the problem is transformed to one involving a boundary integral. The main advantage is the reduction of the dimension of the problem by one — three-dimensional fluid domains are replaced by two-dimensional boundaries.

As a special case of such transformations, it is possible to use conformal-mapping techniques to transfer two-dimensional flow problems into ones involving completely different boundaries of simpler geometry. Examples of the approach can be found in Vanden-Broeck and Keller [41], Dias and Tuck [8], and most recently, Wiryanto [43]. Naturally, conformal-mapping techniques can only be used when considering two-dimensional flows.

In the early 1960's, Hess and Smith [21] developed a method for calculating flows about arbitrarily-shaped non-lifting three-dimensional bodies, based upon a source distribution over the body, represented by plane quadrilateral surface elements. This pioneering work became the basis for many variations which followed. The method was generalisable to allow the use of singularities other than continuous source distributions. Dipoles and vortices were introduced later when considering lifting effects. The paper did not consider the implementation of a free surface, but the concept is of sufficient generality that it is entirely realisable.

Early numerical methods for solving free-surface flows considered a linearised boundary condition, enforced upon a plane, instead of the actual free surface. Dawson [7] developed a method used to solve flows about slow ships.

Even as recently as 1992, Hendrix and Noblesse [20] promoted the use of Kelvin-Havelock sources distributed on flat triangular hull panels, as an alternative to Rankine singularities. The advantage of the Kelvin-Havelock sources is that, since they automatically satisfy the linearised free-surface boundary condition, the free surface need not be represented at all. The advantage of triangular panels is of course that any body surface can easily be represented by them.

More recently, attacks have been launched on the nonlinear problem, in which the exact boundary conditions are to be satisfied on the unknown free surface. Jensen [23] developed a method which used discrete sources located above the free surface. The desingularised approach has advantages, since the corresponding integral equation is no longer singular, and allows for a simpler formulation of the source influences and associated derivatives. Another interesting point was that the potential and its derivatives were determined exactly, without the need for the quadrature rules usually associated with singularity panels.

Forbes [11] developed a method based upon the discretisation of a singular integro-differential equation coupled with an iterative scheme which used a Newton-Raphson technique. The scheme should demonstrate a quadratic rate of convergence.

Raven [30] used a desingularised panel method. Finite difference methods are used to solve Laplace's equation on the fluid boundaries, as opposed to the alternative of solving a system of simultaneous linear equations. The method demonstrates a linear rate of convergence [31].

Still more ambitious endeavours have included the solution of the nonlinear, time-dependent problem. Those tackling this task include Beck, Cao, Schultz and Scorpio [1]. Similar to the approach of Jensen, they use discrete sources located external to the fluid domain [6]. The advantage of including the time-dependency is of course that unsteady flow phenomena can be investigated ([3] and [2]). Scorpio [34] introduced to the approach a fast-multipole algorithm, which reduces the computational effort to order N, in comparison to the more usual N^3 requirement. They are, of course, not alone in their endeavours. For example, Sclavounos and others [24] are also active in the field.

So, there is considerable experience with methods for the solution of the problem as stated, and the options are many and varied. The method proposed in this thesis incorporates several of the more promising techniques utilised in the works mentioned above.

1.4 OUTLINE OF THE PROPOSED METHOD OF SOLUTION

The method adopts what the author considers to be desirable characteristics of several of the above methods, and combines them into one. It is based upon the desingularised boundary integral method, with its reduction in the dimension of the problem by one. It solves for the satisfaction of the nonlinear free-surface boundary conditions, without the simplifications of linearisation or the assumption of the location on which it is to be satisfied. The flow is assumed to be steady, and as such there is no time dependency in the formulation. Instead, an iterative procedure is adopted, in which approximations to the free surface and potential are refined successively until a solution with the desired accuracy is obtained. The procedure is developed with care, to yield a quadratic rate of convergence. In this way, solutions of high accuracy can be obtained after only a few iterations. It is in this niche that the approach adopted here has an advantage over the more versatile time-dependent methods mentioned above. For the case where the flow is steady, time-dependent methods must be executed until the results appear to be steady, and this presumably has an associated computational burden.

The potential is represented by a distribution of singularities, positioned external to the fluid domain. Their magnitudes are determined each iteration by the solution of a system of simultaneous linear equations, which represent the various conditions being enforced. In particular, the singularities used are discrete sources, although the method generalises simply to any type of singularity, discrete or continuous. The associated potential and its derivatives are calculated exactly. The boundary conditions are enforced exactly at collocation points, there being a one-to-one relationship between the number of conditions being implemented and the number of singularity strengths being determined.

1.5 CONTENT OF THE THESIS

This thesis can be described in terms of two parts and an appendix. Part 1 deals with the development of a method for solving fluid-flow problems, based upon the desingularised method for potential representation, coupled with an iterative scheme that successively refines approximations to the solution. It also investigates the parameters which control the accuracy of the solution, and the speed and reliability of the method.

Chapter 2 deals with issues regarding the accurate representation of the potential and free surface. It investigates the representation of the free surface indirectly, by solving the flow beneath a periodic and sinusoidal boundary of infinite extent. This approach allows for accurate determination of the associated error. It investigates the effects on accuracy of the number of points representing one period, the locations of the singularities, and the type of singularities used.

In Chapter 3, the formulation and implementation of the radiation condition is considered, along with the effects of domain truncation. The radiation condition is responsible for correctly selecting the particular solution which does not have waves far upstream. There are several reasonable physical conditions on which the constraint may be based, and these are investigated in detail. Naturally, the length of the computational domain also has an effect on the performance of the radiation condition, and this effect is investigated.

The final chapter of Part 1 (Chapter 4) investigates various formulations of the iterative procedure. Again there are several options available. It assesses, in terms of speed and reliability, the various boundary conditions that can be enforced, and the methods by which the new free-surface approximation can be determined. It also investigates the effects of shifting the singularities between iterations, and determines an appropriate test for convergence.

Part 2 of the thesis deals with a handful of applications of the method, with the intentions of verifying the method's ability to accurately determine such flows, and providing some insight into the physical properties of the solutions.

Chapter 5 investigates three topics, all related to the flow about circular cylinders submerged beneath a free surface. The first is the wave-making of a single circular cylinder. The second section deals with the effects of circulation about the cylinder, and investigates its ability to reduce the amplitude of the waves produced. The last section considers two circular cylinders in tandem. By appropriate arrangement of the cylinders' depth and separation, it is possible to find situations in which the horizontal force acting on either, both, or the combination of the two cylinders, is zero. In each section, the numerical results are compared with the appropriate linear theory, and nonlinear effects are discussed.

In Chapter 6, the wake produced by, and wave resistance of, a submerged prolate spheroid is investigated. A general description of the change in character of the wake with speed is given before a more thorough investigation is made. Results from a few interesting cases are presented.

The final chapter (Chapter 7) deals with the effects produced by finite depth in the fluid being considered. The problem is very interesting, since some fascinating effects can be observed — specifically, they are the widening of the wake near a critical speed, and the disappearance of transverse waves for supercritical flows. After a general discussion of such phenomena, the forces experienced by submerged spheres and spheroids in a fluid of finite depth are compared to numerical calculations and linear theories.

The appendix deals with the formulation of the iterative scheme and associated boundary conditions in greater detail than is provided in Part 1.

Collectively, the thesis is intended to describe a possible method for the accurate solution of steady nonlinear free-surface flows. It shows some applications of the procedure, compares results with existing linear theories where available, and discusses the nonlinear effects inherent in them.

PART I

ACCURACY, RELIABILITY AND SPEED

REPRESENTATION OF A WAVE-LIKE BODY

Two-dimensional flow beneath an infinite, sinusoidal body of finite period is considered. The intention is to determine appropriate choices for the resolution required to represent the body, and the locations of the singularities used to represent the potential. The normal velocity through the body's boundary is used as a measure of error, and accurate solutions are sought. It is believed that the conclusions drawn will provide reasonable guidelines for the accurate representation of a free surface.

2.1 INTRODUCTION

It is possible to remove complexities created by body representation, domain truncation, radiation condition and iterative procedure, by considering a wave-like body. Considering the flow produced beneath a fixed sinusoidal surface of infinite length, with an amplitude and wavelength similar to those expected for a real free surface, allows several issues to be addressed in detail, without the added complications produced by a true free surface, or the presence of another body. Specifically, the following questions can be investigated:

(i) How many collocation points per wavelength are required to adequately represent the shape of a wave?

(ii) Where should the singularities be located in order to accurately represent the velocity potential beneath a wave-like surface?

(iii) Which singularity type is best for representing the potential?

(iv) What is a suitable error measure to use when determining the accuracy of the representation?

Using a fixed and impermeable surface, that is, a Neumann boundary rather than a free surface, has the added advantage that no iteration procedure is required. The strengths of the singularities are determined by a single inversion of a system of simultaneous linear equations. This leads to significant savings in terms of computational effort.

With regard to the locations of the singularities, in principle there is nearly limitless variety — the only requirement is that the singularities are situated external to the fluid. Here, only discrete sources will be considered.

The potential can be represented by the superposition of the uniform stream and a periodic distribution of discrete sources, and can be described as

$$\phi\left(x,z\right)=Ux+\sum_{j=1}^{n_\lambda}\frac{\sigma_j}{4\pi}\log\left(\sin^2\left(\frac{\pi}{\lambda}\left(x-x_j\right)\right)+\sinh^2\left(\frac{\pi}{\lambda}\left(z-z_j\right)\right)\right)\ , \qquad (2.1)$$

where U is the speed of the stream, n_λ is the number of sources used per wavelength, σ_j is the strength associated with the j-th source which is located at (x_j, z_j), and λ is the wavelength of the surface. Within this thesis, for consistency with three-dimensional flows, two-dimensional flows will be described in terms of x and z-coordinates with z representing the vertical direction. In the following, and without loss of generality, lengths are made dimensionless by scaling with respect to the stream speed and gravitational acceleration g, so that $U = g = 1$, the wavelength is $\lambda = 2\pi$, and stagnation height is 0.5.

Within this context, several plausible schemes for the location of singularities come quickly to mind. One possibility is to restrict the singularities to a horizontal plane. An alternative is to follow the general contour of the wave. Within this second option, there is the possibility of placing the sources a set distance from the collocation points directly above the wave, or alternatively, along normals to the wave surface. In each instance, there is the choice of whether singularities should be positioned with respect to the collocation points, or midway between collocation points, or at some other proportion between these two extremes.

Considered here are four schemes for positioning the singularities.

(a) Sources distributed on a horizontal plane, at a predetermined height above the mean height of the surface.

(b) Sources distributed on a horizontal plane, at a predetermined height above the crest of the wave.

(c) Sources distributed at a predetermined height above the actual wave surface.

(d) Sources distributed at a predetermined distance along the upwards-pointing normal of the wave surface.

These will be referred to as schemes (a)–(d) in the following text. In each instance, the collocation points are evenly distributed with regard to their x-coordinate.

There is now a class of problems that can be described by a total of five parameters of choice. The wave amplitude A, the choice of singularity distribution scheme (a)–(d), the number of collocation points per wavelength n_λ, the vertical length parameter associated with each of the singularity distribution schemes (to be referred to as "offset height"), and the horizontal length parameter which describes the amount that the sources are shifted horizontally away from the collocation points (termed "offset shift"). It will be useful to refer to the ratio of offset height relative to the distance between collocation points (in the x-direction) as the "offset height ratio". Similarly, the term "offset shift ratio" is introduced to distinguish the relative value from the absolute, for the horizontal shift parameter. Under schemes (a), (b) and (c), an offset shift of zero indicates that singularities are placed directly above collocation points, and an offset shift ratio of 0.5 would have them placed above the points midway between collocation points. A similar situation applies for scheme (d), except that the singularities lie along normals to the point on the wave surface which is determined by the offset shift parameter. Figures 2.1 and 2.2 show these parameters diagrammatically.

As will be shown later, appropriate error measures can be based upon the magnitude of the normal velocities along the surface. The error measures of choice here are approximations to (i) the maximum absolute normal velocity anywhere along the wave surface, and (ii) the integrated absolute normal velocity along a period of the wave surface. In each case, normal velocities are calculated at 16 equally spaced points (in terms of the x-coordinate) per collocation point. Note that the normal velocity is zero at each of the collocation points. The maximum normal velocity anywhere along the free surface is then approximated by the maximum absolute value of the normal velocity at these points, and

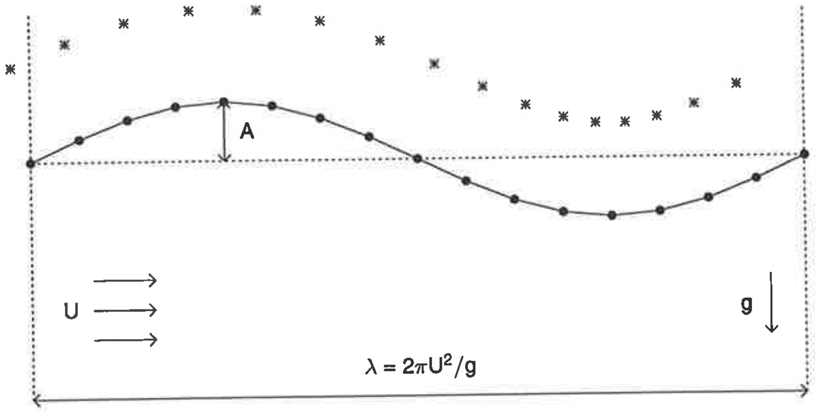

Figure 2.1: Parameters of the problem. There are n_λ collocation points per wavelength.

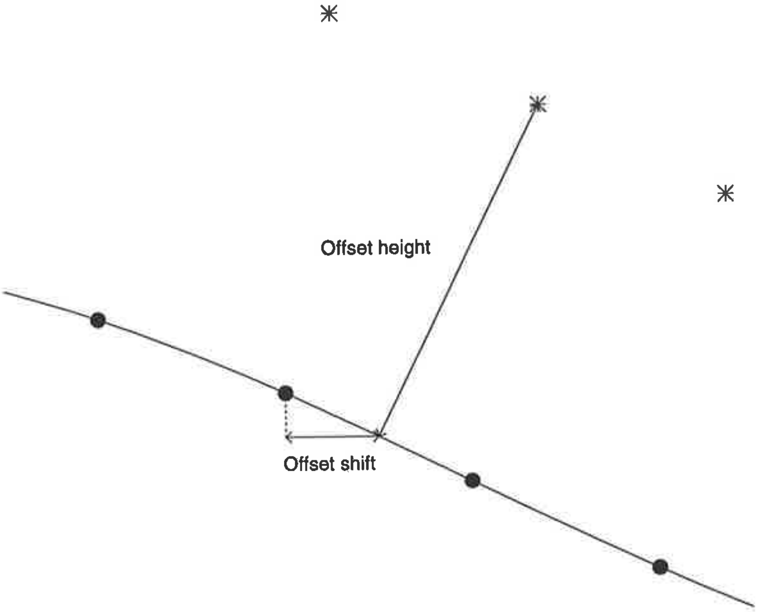

Figure 2.2: Definitions of offset height and offset shift under scheme (d).

the approximation to the integrated normal velocity is determined by numerical integration using the absolute values of the normal velocities, the integration being performed over a single wavelength, and with respect to x.

2.2 TEST CASES

Extensive tests were performed using a wide variety of choices for each of the input parameters. Considered were three cases of sinusoidal wave amplitude — a modest wave of amplitude 0.05, another of amplitude 0.25 which can be considered to be a moderately large wave, and a wave whose amplitude of 0.50 is an upper-bound for the amplitude which can be expected in real life. In the dimensionless units, water waves of amplitude 0.3 or more display distinctly non-linear characteristics which make them dissimilar to a sinusoidal wave. Also, the height of a water wave's crest cannot exceed 0.5, the stagnation height.

Each of the singularity location schemes (a) through to (d) were tested. Choices for the value of n_λ were 4, 8, 12, 16, 20, 24, 28, 32, 64 and 128. The offset height was chosen so that the offset height ratio was one of 0.5, 1.0, 2.0, 4.0, 6.0, 8.0, 10.0, 12.0, 14.0, and 16.0. The offset shift ratio was chosen from the values 0.00, 0.25 and 0.50.

2.3 RESULTS

It is convenient to represent the results graphically, using a single plot for each combination of wave amplitude, singularity location scheme, and offset shift ratio. The error measure can then be plotted as a surface, with one of the independent axes being n_λ, and the other being the offset height ratio. For the graphs that follow, the dependent axis is a base-10 logarithm of the error measure. An error measure of the order of 10^{-15} is comparable to machine precision, and will be seen to be the limiting factor for some of the results.

The test cases yield 36 graphs for each error measure. In general, the shapes of the two related graphs (one using the maximum, and the other, the integrated error measure) are strikingly similar for any given choice of amplitude, scheme and offset shift ratio, and so it is not necessary to display both. In the following, only the integrated error measure will be shown, and only a representative selection of the plots will be reproduced.

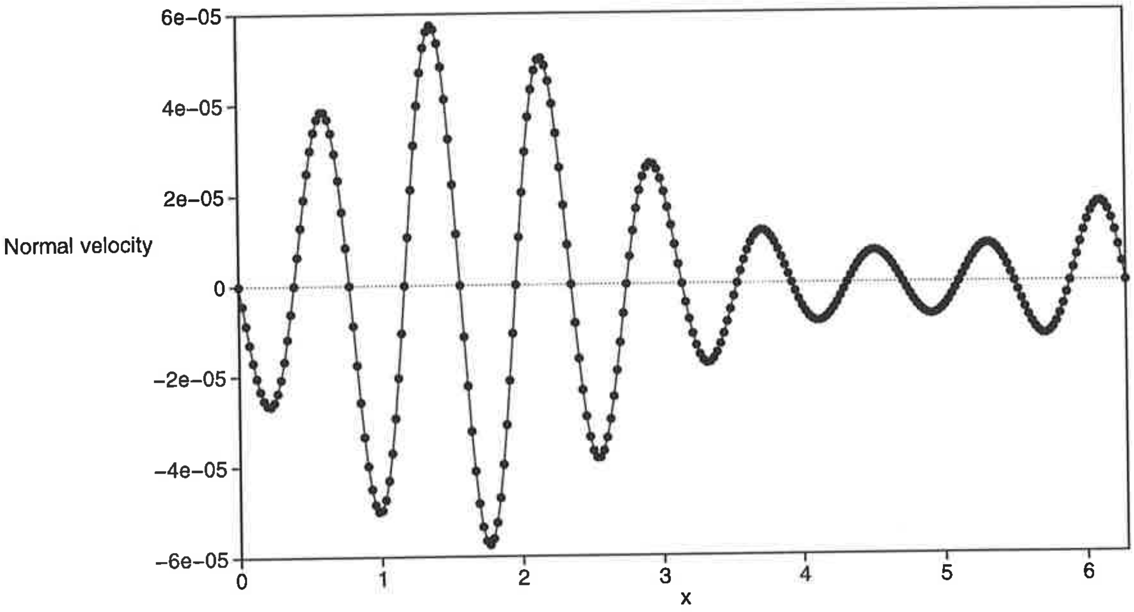

Figure 2.3: Normal velocity along a period of the wave-like surface.

2.3.1 NORMAL VELOCITY AS AN ERROR MEASURE

The first task is to justify the use of error measures based upon the normal velocities. Figure 2.3 shows the normal velocity through the surface as determined at 16 equally spaced points per collocation point. This particular case is for a wave of amplitude 0.25 represented by 16 collocation points per wavelength, with the singularities' locations determined using scheme (d), an offset shift of 0.00 and an offset height ratio of 8.0.

If the normal velocity were zero everywhere, the solution would be exact, and so, the extent to which the normal velocity is non-zero is a measure of the inaccuracies in the representation. The figure shows that the normal velocity is zero (or more precisely, of the order of machine tolerance) at the 16 collocation points, as is required by the enforced Neumann boundary condition. The normal velocity varies in a smooth manner between collocation points, indicating that behaviour of the normal velocity is being adequately resolved by the 16 points per collocation point. The maximum absolute value is approximately 6.0×10^{-5}, which should be compared to the value of Un_1 where n_1 is the component in the x-direction of the normal to the surface. Un_1 is the normal velocity if the flow is approximated by a uniform stream only, and for a wave of amplitude A, has a maximum of $UA/\sqrt{1+A^2}$. In this instance, that value is $1/\sqrt{17}$ or approximately 0.243. Clearly then, the error in this case is very small.

Also of interest is the general shape of the envelope in which the curve lies. It too is roughly sinusoidal in shape with a mean height of about 3×10^{-5}, and an amplitude of a similar magnitude. The envelope is largest at $x = \pi/2$, and smallest at $x = 3\pi/2$, which suggests that the wave is under-represented at its crest when compared to the representation of its trough. (Recall the free surface is a perfect sine wave, and so also has a maximum at $x = \pi/2$, and a minimum at $x = 3\pi/2$.) This then gives a clue as to how one could modify the spacing of the singularities to achieve a moderate increase in accuracy, without the need for more collocation points (by decreasing the spacing near the crest, and increasing it near the trough).

Never-the-less, the smooth behaviour of the normal velocity, coupled with the necessity that it vanishes for an exact solution, indicates that the normal velocity provides the basis for an accurate and reliable error measure.

2.3.2 AMPLITUDE 0.05

This is the case of a wave of modest amplitude, having a wave steepness of approximately 0.016. In fact, it is reasonable to expect that conclusions drawn from this case would apply equally well to a flat surface (used, for example, when considering the linearised free-surface boundary condition).

The first graph considered here (Figure 2.4) shows some of the best results. It serves as a basis for detailed analysis, as well as a benchmark by which the other graphs can be compared. It corresponds to the case where scheme (d) is used, and the offset shift is zero. That is, singularities are located along normals to the surface collocation points.

The plot can be considered as composed of three faces — a sloping face at the left hand rear, a steeply sloped face at the right hand rear, and a horizontal floor in the foreground. The roughly horizontal floor is a consequence of the limitations of machine accuracy. The rear right hand face shows an exponential decrease in error as the number of collocation points per wavelength is increased, until such a stage that machine precision is the limiting factor. Similarly, the rear left face also displays an exponential reduction in the error measure, again until machine precision comes into play.

The general shape of the plot is smooth, in that there are no oscillations in the order of magnitude of the error for neighbouring choices of n_λ and offset shift ratio. This case

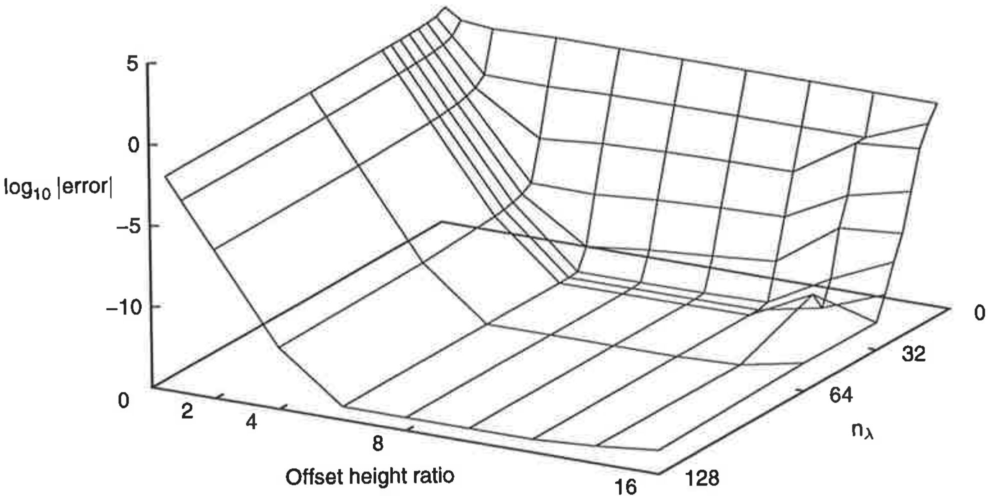

Figure 2.4: Integrated error measure for scheme (d) with offset shift 0.0. The wave amplitude is 0.05.

could be described as being well-behaved.

Clearly, in this case, choosing 24 or more collocation points per wavelength and an offset height ratio between 6.0 and 12.0 yields results that have normal velocities that are due to the limitations of machine precision.

2.3.2.1 EFFECTS OF OFFSET HEIGHT RATIO AND RESOLUTION

Focussing attention on lines of constant n_λ, an initial exponential reduction in normal velocity for increasing offset height ratio can be observed. Typically, small offset height ratio (2.0 or less) yields results of poor accuracy. As offset height ratio is increased (say to 6.0) the error reduces until it reaches a minimum value, at which is stays until the offset height ratio is of the order of 12.0, at which time the error grows, and continues to do so until the maximum offset height ratio that was tested (that is, 16.0) is reached. The expectation is that the trend of growth in error would continue for larger values of offset height ratio. For values of n_λ less than 24, the limiting factor is the resolution, whereas for values of n_λ greater than 24, the limiting factor is machine precision.

Similarly, the lines of constant offset height ratio show that the error decreases exponentially with increasing n_λ, until it reaches a minimum, at which it remains, regardless of further increase in resolution. In the cases where offset height ratio is less than 6.0, it is the limiting factor. For cases where the offset height ratio is greater than 6.0, the limiting factor is machine precision.

The intersection of the two non-horizontal faces produces a line along which the offset height is constant. This is the critical value at which the limiting factor switches between offset height ratio and resolution. In this instance, this height is approximately 1.5 or equivalently $\lambda/4$.

This suggests a method of determining the optimum offset height. Firstly, a moderate offset height and resolution are selected. Several cases are tested, with offset height increasing. When the error no longer decreases in an exponential manner, the optimum offset height has been reached. At this stage, the offset height is fixed and the resolution is increased until the desired accuracy is achieved, or the limits of machine accuracy come into effect.

The conclusion to be drawn is that an offset height greater than $\lambda/4$, coupled with of the order of 20 collocation points per wavelength, will yield results whose accuracy is limited by machine precision.

With this description serving as a benchmark, it is now possible to proceed to evaluate the effects of choice of scheme and offset shift ratio on the general behaviour of the error measures.

2.3.2.2 EFFECT OF OFFSET SHIFT RATIO

In all of the singularity location schemes, there is a periodicity of 1 associated with the offset shift ratio. For example, choosing an offset shift ratio of 0.75 is equivalent to using −0.25. The singularities will be located in exactly the same spot. Thus, only offset ratios in the range of −0.50 to 0.50 need to be considered, as this range represents all possible choices. Further, it is possible to use arguments of symmetry to show that results for a negative offset shift ratio are the same as those for the corresponding positive offset shift ratio. Thus, consideration can be restricted to cases in the range 0.00 to 0.50. Consequently, in the present study only the values of 0.00, 0.25 and 0.50 will be tested.

With the aid of Figure 2.5, it is possible to investigate the effect of offset shift ratio on accuracy. The figure shows three graphs for offset shift ratios of 0.00, 0.25 and 0.50, from top to bottom respectively.

Of immediate note is the strong similarity between the results for 0.00 and 0.25, and the marked difference (and degraded performance) displayed for the case 0.50. This suggests there is a rapid deterioration in the accuracy of the results as the singularities

Offset shift ratio 0.00

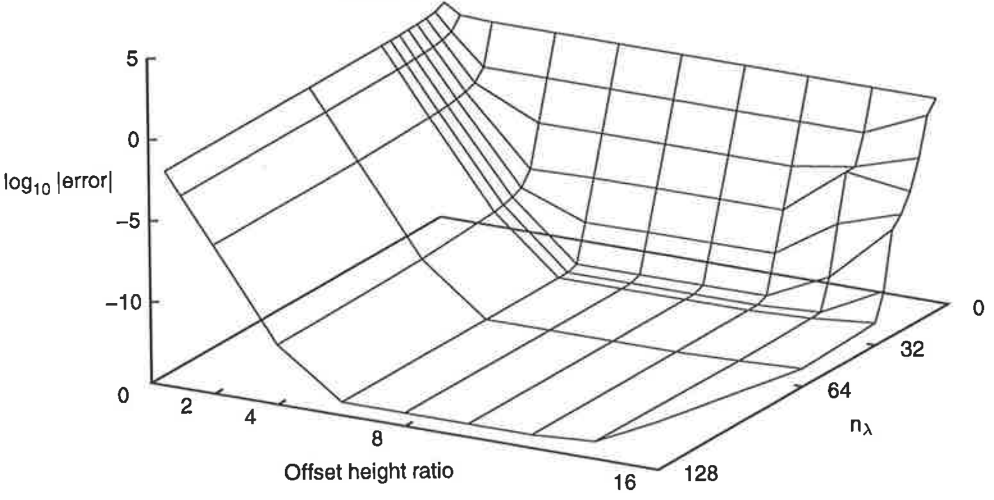

Offset shift ratio 0.25

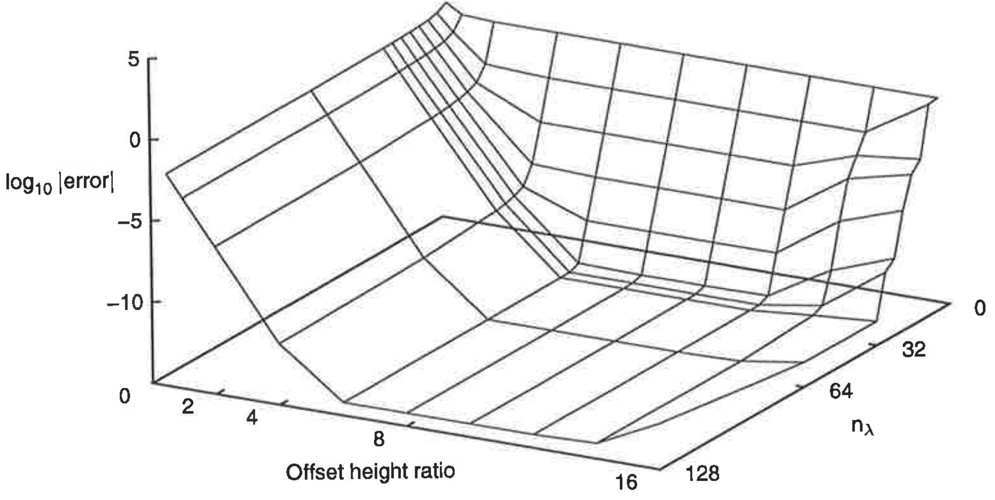

Offset shift ratio 0.50

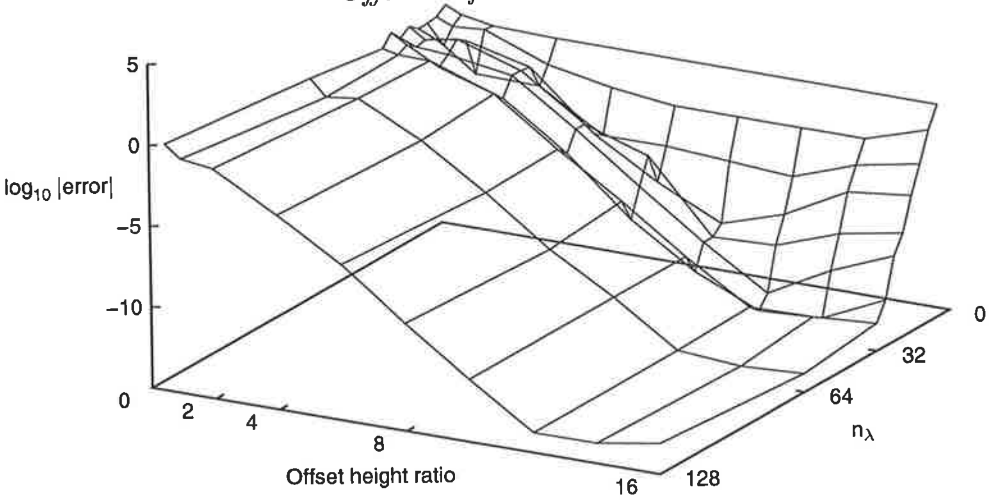

Figure 2.5: Integrated error measure for scheme (c) with offset shift ratios of 0.00, 0.25 and 0.50 respectively. The wave amplitude is 0.05.

approach the mid-points of the discretisation — but that the effect is localised to a small range of offset shift ratios around the value of 0.50. Note also that the error for the case with offset shift ratio 0.50 varies erratically, and so could be described as ill-behaved. The degradation is most noticeable for moderate choices of offset height ratio. To put this in context, it is important to recall that the results are poor for small offset height ratio in all cases, and that for the benchmark case, the limiting factor at high offset height ratio is machine precision. Both these factors are still at play in this case also. The reduced performance for moderate offset height ratio can be explained by the effect of offset shift ratio on the conditioning of the system, and will be discussed in greater detail in Section 2.4.

Similar trends are observed for schemes (a), (b) and (d). In each instance, there is a strong similarity between the results at offset shift ratio 0.00 and 0.25, with rapid degradation at 0.50. In fact, 0.00 and 0.25 are indistinguishable except for offset height ratios of greater than 8.0, and even then there is no clear preference for one or the other. Offset shift parameters near 0.50 can be ruled out, as they produce results of inferior quality.

2.3.2.3 EFFECT OF SINGULARITY LOCATION SCHEME

For a fixed offset shift ratio (either 0.00 or 0.25), the four graphs corresponding to schemes (a)–(d) are remarkably similar. So much is this the case that there is no need to reproduce them here — they all look like the first two graphs of Figure 2.5.

At this stage, it is relevant to point out that there is some redundancy between schemes (a) and (b). For any given offset height, there is a corresponding value of offset height ratio under scheme (a), and another (lower) corresponding value under scheme (b). This is observable within the graphs as slight differences in error for small offset height ratio and large n_λ. Scheme (a) is in general the poorer of the two. Any difference is not noticeable for large offset height ratio or small n_λ.

Another point to note is that under scheme (a), for large n_λ and small offset height ratio, the singularities may lie beneath the crests. That is, they may have entered the fluid domain. Such cases are unacceptable as they violate the requirement that the potential satisfies Laplace's equation everywhere in the fluid domain. This will only occur if

$$\frac{n_\lambda}{\text{offset height ratio}} > \frac{\lambda}{A}\,. \tag{2.2}$$

In this instance, this makes only three points on the graph for scheme (a) invalid: offset height ratio of 0.5 at $n_\lambda = 64$, offset height ratio of 0.5 at $n_\lambda = 128$, and offset height ratio of 1.0 at $n_\lambda = 128$. This becomes more significant, with more points being disqualified as the wave amplitude grows, and needs to be kept in mind when considering the results for the larger amplitude waves.

For a small amplitude wave, the normals are near vertical, and so there is little reason to expect any difference between schemes (c) and (d). Further, as the amplitude is small, there is little difference between schemes (c) and (a), except as noted above. Consequently, with the exception of regions where scheme (a) is invalid, at this stage there is no clear reason to believe that any one scheme is superior to the others.

2.3.3 AMPLITUDE 0.25

This case represents a wave of reasonably large amplitude. In practice, it is around this amplitude that water waves start to exhibit nonlinear properties, and waves of this amplitude will be considered when dealing with actual free-surface flows.

The graphs corresponding to this case (for various schemes and offset shift ratio) show properties similar to those for the case of wave amplitude 0.05.

Offset shift ratio 0.50 again produces results of inferior accuracy, and there is little difference between 0.00 and 0.25.

The results are qualitatively similar to those for amplitude 0.05. Again, there is an exponential decrease in error as either offset height ratio or resolution is increased, until a limiting factor is encountered, at which time no further increase in accuracy can be produced. The intersection of the two faces produces a line of critical offset height, and for this amplitude, the critical height is approximately 0.9, or equivalently $\lambda/7$. For combinations of offset height ratio and n_λ that produce an offset height less than this value, it is the offset height ratio that is the limiting factor. For combinations where the offset height is greater than this critical value, the resolution limits the obtainable accuracy. However, for combinations where the offset height ratio is greater than 6.0 and

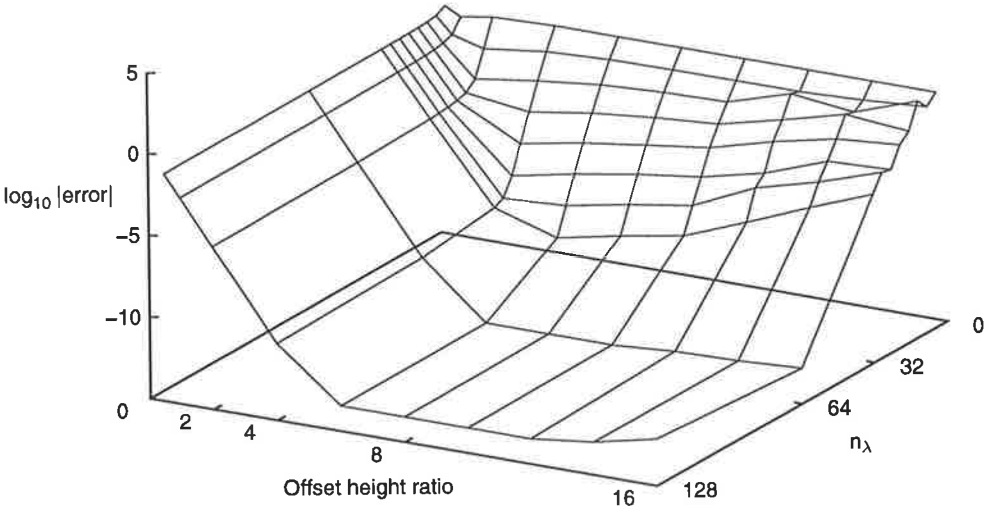

Figure 2.6: Integrated error measure for scheme (d) with an offset shift ratio of 0.00 for a wave-like body of amplitude 0.25.

the value of n_λ is greater than 64, machine accuracy is the limiting factor. Interpolation suggests that in some cases, machine accuracy is the limiting factor for $n_\lambda = 40$.

Although the results for schemes (a) and (b) are similar where (a) is valid, along lines of constant offset height ratio, scheme (c) displays a marginally better rate of decrease in error than does (b). Scheme (d) has the fastest rate of decay for the errors, and as it displays the smoothest results it appears to be the most reliable of the schemes. As such, scheme (d) is starting to become the preferred method for the location of singularities.

The results for scheme (d) at offset shift 0.00 are displayed in Figure 2.6.

2.3.4 AMPLITUDE 0.50

This case represents an upper-bound for the possible wave amplitude in the sense that free-surface waves can never have a crest height greater than stagnation height, which, when made dimensionless by scaling with respect to the stream speed and gravitational acceleration, is 0.5. In practice, waves of an amplitude near this limit exhibit strongly nonlinear characteristics (the troughs are raised relative to a sine wave, the crests become sharper, and the wavelength decreases slightly), and so a better test case would be a trochoid which would demonstrate similar properties. (Newman [29, p. 250] gives a brief discussion of the suitability of using a trochoid to approximate a nonlinear wave, and also several references to other relevant discussions.) This case is however still of value if considered as an upper-bound to the amplitude of those free-surface waves that demonstrate

Scheme (b)

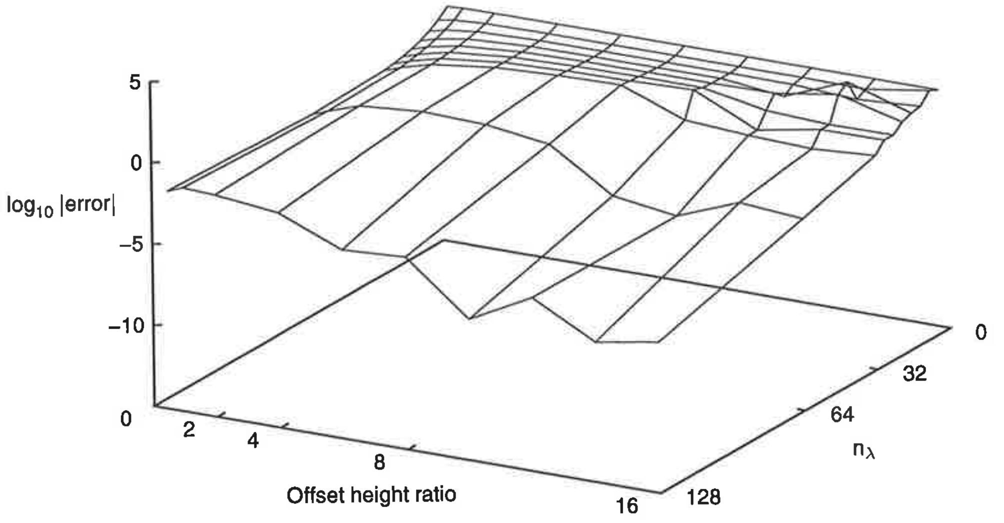

Scheme (c)

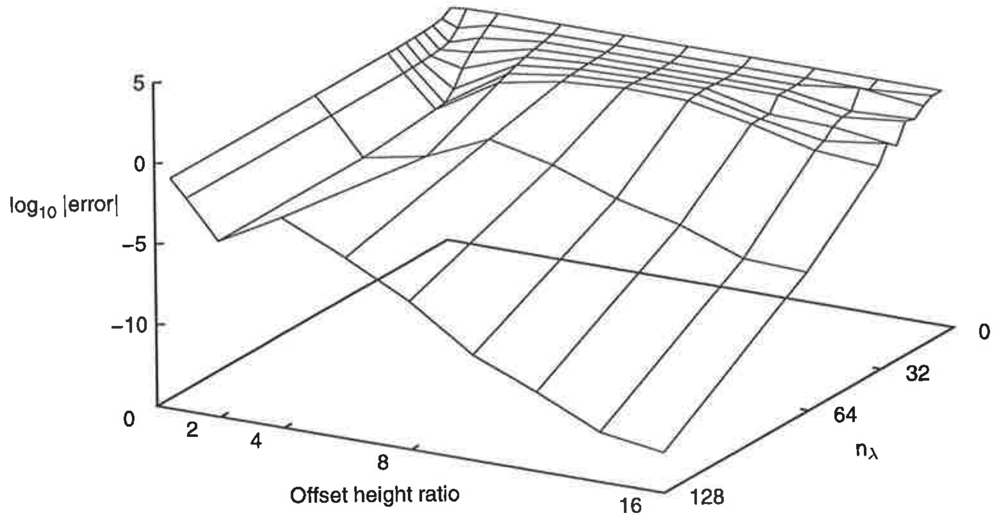

Scheme (d)

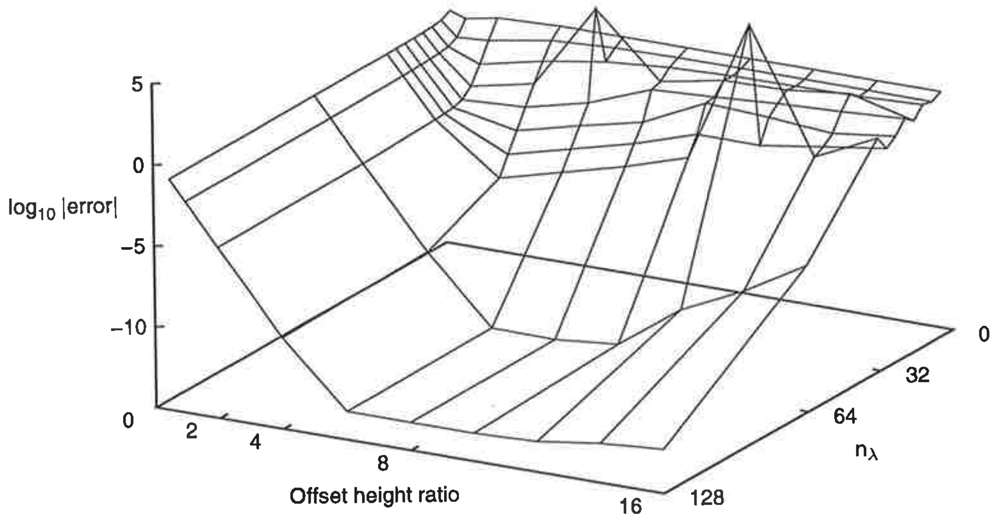

Figure 2.7: Integrated error measure for schemes (b), (c) and (d) with offset shift ratios of 0.00. The wave amplitude is 0.50.

sinusoidal characteristics.

Yet again the same patterns are observed. Offset shift ratio is best at 0.00. There is a slight variation in accuracy at 0.25, and the results are poor at 0.50. The critical value of offset height is 0.7, or equivalently $\lambda/9$. For combinations where the offset height ratio is greater than 6.0 and n_λ is greater than 64, the limiting factor is machine precision.

There is now a clear preference for scheme (d). Figure 2.7 shows graphs of schemes (b), (c) and (d) with an offset shift of 0.00. It is clear that scheme (d) is superior, and in comparison, relatively slow rates of reduction in error can be seen for schemes (b) and (c).

The graph for scheme (d) displays two points where the accuracy is dramatically reduced. These are for $n_\lambda = 16$, with offset height ratio 6.0, and for $n_\lambda = 32$ at offset height ratio 12.0. These are interesting peculiarities as they represent cases where the singularities are positioned at a distance that is very close to the radius of curvature of the trough. Consequently, several singularities are positioned closely (in fact in each case, two singularities are superimposed), and this leads to a poorly conditioned system, and a consequential increase in error. In practice, one must be wary to avoid the clustering or superposition of singularities, and this can usually be achieved by ensuring that the offset height is smaller than the local radius of curvature.

2.4 FURTHER ANALYSIS

Greater understanding of the conclusions reached in Section 2.3 can be attained by considering the nature of the influence produced by a discrete source on the surface.

The potential at some point (x, z) induced by a discrete source located at (x_s, z_s) and of strength σ is given by $\phi_s(x, z) = \frac{\sigma}{2\pi} \log r$, where $r^2 = (x - x_s)^2 + (z - z_s)^2$, and so the velocity produced is $\underset{\sim}{q}_s(x, z) = (\phi_{sx}, \phi_{sz}) = \frac{\sigma}{2\pi}((x - x_s)/r^2, (z - z_s)/r^2)$. The influence of a discrete source acts in a direction that is radial from the source, and with velocity proportional to r^{-1}. The two factors that effect the value of $\underset{\sim}{q}_s . \hat{\underset{\sim}{n}}$ at points other than the collocation point are the distance of the source from that point on the boundary, and the angle, θ, between the directions of the surface normal and the induced velocity at that point. Both of these are functions of the source location. Figure 2.8 shows the effect of these factors for the two offset height ratios of 0.5 and 2.0. It becomes immediately clear

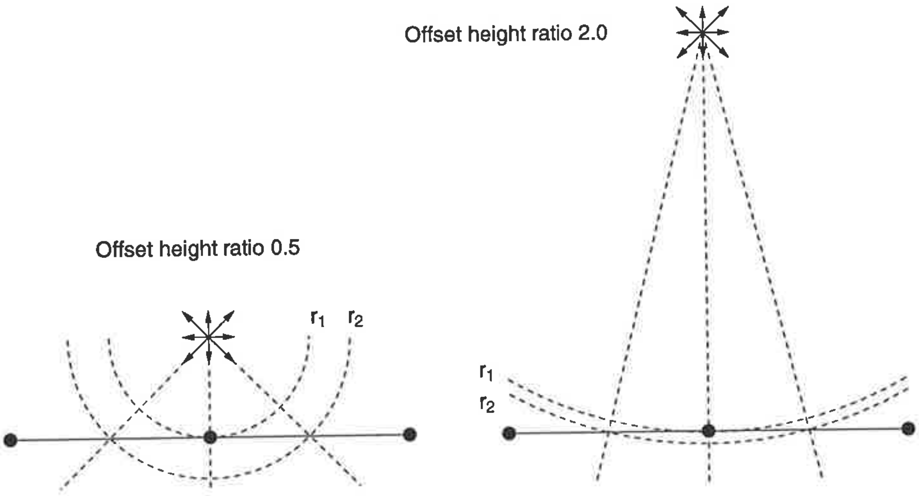

Figure 2.8: Diagram showing the effect of offset height ratio on the accuracy of the boundary condition in the neighbourhood of a collocation point.

that the value of $\underset{\sim}{q}_s . \hat{\underset{\sim}{n}}$ induced over the surface will vary less for larger offset height ratios. This is of course true regardless of the choice of offset shift ratio.

Suppose that in the absence of a source, the normal velocity everywhere along the boundary near a collocation point is C. To satisfy the kinematic condition $\underset{\sim}{q} . \hat{\underset{\sim}{n}} = 0$ at the collocation point, the strength of the source such that the velocity it induces will satisfy $\underset{\sim}{q}_s . \hat{\underset{\sim}{n}} = -C$ is sought. For the moment, a local coordinate system is employed, such that the origin is located at the collocation point, the x-axis lies along the tangent to the surface at the collocation point, and the z-axis lies in the direction of the outwards normal, so $\hat{\underset{\sim}{n}} = (0,1)$. Locating the source along the normal to the collocation point at an offset height of z_s, that is, at $(0, z_s)$, induces a velocity at the collocation point that is $\underset{\sim}{q}_s = \frac{\sigma}{2\pi}(0, -1/z_s)$. Thus, if the total normal velocity at this point is to be zero, then $\sigma = 2\pi C z_s$. With this choice of source strength, elsewhere on the boundary the normal velocity induced by the source is $\underset{\sim}{q}_s . \hat{\underset{\sim}{n}} = -C\left(z_s/r\right)^2$, so the total normal velocity at $(x, 0)$ is $\underset{\sim}{q} . \hat{\underset{\sim}{n}} = C\left(x/r\right)^2 = C \sin^2\theta$.

For large enough offset height ratio and near the collocation point, r can be approximated by z_s, and so the normal velocity behaves like $C\left(x/z_s\right)^2$. Three interesting points can be derived from this at once. Firstly, for fixed n_λ, the error measures are inversely proportional to the square of the offset height ratio, and hence the exponential decrease that is observed in the error on the left hand rear face of the graphs. Secondly, for fixed *absolute* offset height, the error is inversely proportional to the square of the number of points per wavelength. The combination of these two points yields the third — that *the error is constant for the same offset height ratio, relatively independent of the number of points per wavelength!* Once there are enough points to represent the *shape* of the surface, then, for the same offset height ratio, there is no increase in accuracy of the *potential* with increasing n_λ. Increased computational effort yields no improvement in accuracy. This is supported by the curves of constant offset height ratio along the left hand face of the plots. They lie parallel to the n_λ-axis indicating no change in error measure.

Although individual sources cannot really be considered in isolation from the remainder of the influences, this does at least provide some insight into why small offset height ratios will produce inferior accuracies. The fact that these conclusions are observed in practice provides support for the validity of this brief analysis.

It would appear that the larger the offset height ratio, the more accurate the results are. However, the fact that higher values of offset produce a more constant influence along the boundary, indicates that there will be a degree of coupling between neighbouring singularities in their effects upon a collocation point.

A low offset height produces a situation in which the satisfaction of the boundary condition at one particular node is predominantly influenced by the singularity that is nearest. This leads to a well conditioned system of equations, in that there is little coupling between the boundary condition at a collocation point and the strengths of sources other than the one nearest. Such a situation leads to singularity strengths that vary from each other by a small amount and in a smooth manner. As shown previously, this also produces inferior results.

This is in contrast to the case when offset height is large, because the boundary condition at a given collocation point is influenced by the strengths of not only its associated singularity, but also others nearby. This leads to a system of equations that is not as well conditioned, and is characterised by source strengths that vary by large amounts between neighbouring singularities, and in some cases oscillating in sign. In extreme cases, the system is so poorly conditioned that calculations become inaccurate. *It is the ill-conditioning of the system of equations that results in the degradation of accuracy as the offset height is increased beyond the optimum value.*

These two phenomena also provide the clues as to why results are most accurate when the offset shift is zero. Firstly, due to the fact that the magnitude of induced velocity decays at the rate proportional to r^{-1}, a slightly smoother representation will be gained (in the manner of Figure 2.8) if the singularities are located near the collocation points, rather than between them. Secondly, because the velocity acts in a radial direction, the influence is stronger when the direction is aligned with the normal, rather than at an angle to it. However, both of these effects are small for moderate choices of offset height ratio. The dominant factor is that *the system of equations is better conditioned if the singularities lie near collocation points*, rather than somewhere between them. This is why the the results display a degradation in accuracy for offset shift ratio of 0.50 with moderate choices of offset height ratio, and for offset shift ratio 0.25 at high offset height ratio, where the system is already poorly conditioned.

With this in mind then, it no longer comes as a surprise that the best scheme of those tested above is scheme (d) with offset shift 0.00. In this case, singularities lie directly along normals to the collocation points, ensuring a well conditioned system and accurate results for moderate choice of offset height ratio.

2.5 CONSIDERATION OF OTHER SINGULARITY TYPES

So far, only discrete sources have been used to represent the disturbance to the uniform-stream potential. There are, however, a variety of common singularity types that can be used. The list includes discrete vortices, discrete dipoles, panels of sources, vortex panels, dipole panels — and there is the possibility of using a combination of any or all of these. In this section, the anticipated consequences of using some of these singularity types will be discussed briefly.

2.5.1 DISCRETE VORTICES

The point vortex is the conjugate analytic function of the discrete source, having potential

$$\phi = \frac{\kappa}{2\pi} \arctan\left((z - z_s)/(x - x_s)\right). \tag{2.3}$$

Its influence acts in a circular fashion (rather than the radial manner of sources), so it acts in a direction normal to the surface when it actually lies on the surface. Thus, it will have the greatest influence on the kinematic boundary condition when it lies on the surface, and for a desingularised approach, this means between the collocation points. However, it is reasonable to expect that the boundary condition is not satisfied accurately between collocation points when the singularity lies close to the surface, as was seen to be the case with sources. Although in this instance, the normal and the direction of influence are aligned along the local surface boundary between collocation points, the effect of changing radius is much greater. As the radius decreases to zero (that is, as points on the boundary in the neighbourhood of the vortex are considered), the strength of its influence grows indefinitely, creating large normal velocities. Similarly, there are issues concerned with the conditioning of the system of equations when the singularity is placed midway between collocation points, as would otherwise seem to be the logical choice.

Consequently, it is expected that results of an inferior quality will be produced by vortices, in comparison to discrete sources.

2.5.2 DISCRETE DIPOLES

With discrete dipoles one need not only consider where the singularities should be placed, but also in which direction they should be aligned. If the axis of the dipole is aligned with the local surface, then in a manner that is similar to that of a vortex, the influence of the dipole will be in the general direction of the surface, rather than normal to it. In this direction, the dipole will have little capacity to satisfy the kinematic boundary condition.

If directed so that the dipole axis is normal to the surface, the influence will be such that it can be used to satisfy the kinematic boundary condition. However, an analysis similar to that performed for the discrete source of Section 2.4 would suggest that the effect of the change in radius along the nearby surface is greater (the velocity induced by a dipole is proportional to $1/r^2$), and also the angle between the surface normal and the direction of influence increases more dramatically. Consequently, the resulting normal velocity in the neighbourhood of a collocation point is likely to vary more than that for a discrete source, and the overall accuracy of the representation of the potential will be poorer.

2.5.3 SOURCE PANELS

As panels are continuous distributions of sources, it is expected that a smoother velocity distribution would be produced over a nearby body surface by a source panel than would a single discrete source. This would be of greatest advantage at small offset height, where discrete sources produce an influence that varies significantly over the body surface in the neighbourhood of the collocation point. However, increasing offset height to a moderate value where discrete sources perform well has no effect on the computational effort required, and as such, does not represent any additional expense. At moderate offset height, discrete sources produce accurate results, and panels are unlikely to be an improvement. At large offset height, the system of equations is ill-conditioned, and it is this that effects the quality — presumably, panels would suffer from the same problem.

It is unlikely however, that fewer panels will be needed than discrete sources, because, as shown previously, there is a minimum number of collocation points required to capture the shape of the surface, and it is this that is the limiting factor with regard to accuracy. It is hard to imagine that panels would do this more effectively.

Consequently, it appears likely that source panels offer little advantage over discrete sources for capturing the flow beneath a wave-like surface. (This conclusion is, however, unlikely to be reached for some other bodies. This applies in particular to those with sharp corners, where it is anticipated that discrete sources would prove to be inadequate.)

2.5.4 OTHERS

Vortex panels are unlikely to be of value as they suffer from the fundamental problem that for a desingularised panel, the influence is not in a direction normal to the surface.

Dipole panels can be shown to be identical to a superposition of a source and a vortex of suitable strengths located at each end of the panel, and as such offer no advantage over a distribution of discrete sources.

2.6 A NOTE ON COMPUTATIONAL EFFORT

It is important to realise that, in the search for results of greater accuracy, there is no change in computational effort unless the value of n_λ is changed. That is, modifying the value of offset height has no effect on the computational cost. As such, it is desirable to achieve maximum accuracy by ensuring that the offset height being used lies in a range which is optimal, before increasing the number of points used to describe the surface.

2.7 A WARNING ABOUT LARGE OFFSET HEIGHT

In this chapter so far, when discussing the optimal range of offset height ratio, the importance of operating in a region where the error appears to be a minimum has been stressed. In practice, one would be wise to operate in the lower end of such a range. Typically, this is a value such that the results are not yet inhibited by the machine precision. When calculations become affected by machine tolerance, it becomes difficult to determine an upperbound for the associated error. For example, the calculation of normal velocity is in fact a relatively straight-forward computation, requiring only the evaluation of the first derivative of the potential at the point due to each source. More elaborate computations may require significantly larger numbers of computations, and as such may be more susceptible to the accumulated effects of round-off error. In such instances, potentials determined where machine precision has been a limiting factor may yield inaccurate results. Thus, for instance, in the above where an offset height ratio in the range 4.0–8.0 appears to be satisfactory, one may be advised to use the offset height ratio of 4.0 as a preference.

2.8 CONCLUSION

It is clear that singularities are best located along normals to the surface and with an offset shift of zero. That is, they should be normal to collocation points. Discrete sources are found to provide accuracies for which the limiting factor is the capability of the computer to resolve small numbers.

A strategy for optimum location is to determine, for a given resolution, the offset height at which the error measure is a minimum, and then, using this offset height, increase the resolution until a result of the desired accuracy is achieved.

For the wave with amplitude 0.5, using an offset height of approximately 0.6 is appropriate. For values less than this, there is a loss of achievable accuracy. For greater values, ill-conditioning of the system of simultaneous linear equations results. Then, using 64 points per wavelength provides an accurate representation of the body. This combination corresponds to an offset height ratio of approximately 6.0. For smaller amplitude waves, one does not need such great resolution, and the offset height can be increased.

RADIATION CONDITION AND DOMAIN TRUNCATION

Various candidate radiation conditions are assessed for their ability to select the particular solution which does not have waves far upstream. The location at which the radiation condition is enforced, and the points of truncation of the computational domain, are assessed for their effects upon successful implementation of the radiation condition.

3.1 INTRODUCTION

The rôle of the radiation condition is to select from the infinite family of possible solutions the one which does not have any waves upstream of the disturber. One can base the formulation of the radiation condition on the behaviour that can be expected from that particular solution. It is however, reasonable to expect that different radiation condition formulations (based upon different aspects of that behaviour) will produce results of differing accuracies.

Also, the location at which the radiation condition is to be enforced is a matter of choice, but again, one can expect this to have an effect on the performance of the radiation condition. The length of the computational domain (in both the upstream and downstream directions) can also be expected to influence this.

The purpose of this chapter is to investigate several possible radiation condition formulations for their ability to accurately select the desired solution. After a brief discussion of the radiation condition, several alternatives will be formulated. They will then be assessed for accuracy, in conjunction with the locations at which they are applied. Finally, the effects of domain truncation will be investigated.

3.2 THE RADIATION CONDITION

Consider a steady-state free-surface potential flow past a body, as could be defined by equations (1.1)–(1.4) on page 4. There exists a family of solutions, each member of which corresponds to the body in an already disturbed stream. For example, if two bodies move in the same direction and with the same speed, and are positioned such that one is operating in the wake of the other, then the fluid surrounding the trailing body satisfies all the constraints *irrespective* of the disturbance produced by the upstream body.

Therefore, to uniquely determine the flow about a disturber, the nature of the flow upstream from the disturber must also be prescribed. Here, the interest is in the flow created by objects moving through what would otherwise be calm fluid, and so the desired particular solution has no waves far upstream.

This is prescribed loosely by the radiation condition, which is often stated as

$$\underset{\sim}{\nabla}\phi \to U \quad \text{upstream,} \tag{3.1}$$

but which can appear in any equivalent form that suggests the flow upstream is not disturbed.

For the two-dimensional case, each member of the family of solutions can be constructed by the superposition of the desired particular solution with an infinite wave train. The wave train is restricted in its wavelength so that its speed is consistent with the speed of the fluid, but it can be of arbitrary phase (relative to that of the waves that exist downstream in the particular solution), and have any amplitude (provided the resulting wave is non-breaking). Thus, this family of solutions can be described by two parameters, which may be thought of as the amplitude and phase of the upstream wave. This suggests that an additional two constraints are required to uniquely specify any given member of the family. The *two* constraints that select the desired particular solution are *collectively* the radiation condition.

In the three-dimensional case, the family of solutions has an infinite number of parameters that describe it. For a train of planar waves incident at angle θ (for all angles $-\frac{\pi}{2} < \theta < \frac{\pi}{2}$), the wavelength must be such that the component of its velocity in the direction of the body's motion is the same as that of the body itself, to ensure the satisfaction of the steady-state requirement. As with the two-dimensional case, each of these wave trains can be of arbitrary amplitude and phase. The increase of complexity results from the fact that the amplitude and phase are now functions of θ.

For the remainder of this chapter, attention will be restricted to the two-dimensional case. The extension to the three-dimensional case is straight-forward.

3.2.1 FORMULATION OF CANDIDATE RADIATION CONDITIONS

The task of a radiation condition is to select the desired particular solution, and reject any solution that has waves upstream. It is the last part of this statement that is the key in formulating candidate radiation conditions. The two constraints must be such that they are not satisfied simultaneously by a large upstream wave, but should still allow for the unknown disturbance to the upstream domain.

In general, suitable possibilities are based upon the elevation of the free surface far upstream, and the horizontal and vertical velocities found there. In this region the flow behaves in a linear manner, and as such, any nonlinear terms in candidate radiation conditions can be neglected without consequence. This provides a basis for reducing the set of candidate radiation conditions to those that are linear in the perturbation potential and its derivatives.

The assumptions of the linear theory for a free surface are that the wave amplitude and slope are small quantities in comparison to the stream speed (see Newman [29, page 238]). For the steady-state problem, the kinematic and dynamic free-surface boundary condition can be combined to yield the linearised boundary condition

$$U^2\phi_{xx} + g\phi_z = 0 \,. \tag{3.2}$$

Here we are assuming two-dimensional flow, with the z-coordinate representing elevation. It is consistent with the neglect of terms of second order or higher in the perturbation potential to apply the boundary condition on the surface $z = 0$.

It is an interesting consequence of the combination of the linearised free-surface boundary condition with the two-dimensional Laplace equation that *all* derivatives of the potential (when evaluated at the free-surface) can be directly related to either ϕ_x, ϕ_z, or ϕ_{xz}. This is based upon the observation that differentiation twice with respect to z is proportional to (by Laplace's equation) differentiation twice with respect to x, which is proportional to (as a consequence of the boundary condition) differentiation once with respect to z.

Also, under the assumptions of linearity, the free-surface elevation can be determined by

$$\zeta = -\frac{U}{g}\left(\phi_x - U\right) . \tag{3.3}$$

From this form, one can see at once that the free-surface elevation is proportional to the perturbation in the horizontal velocity.

Consequently, all derivatives of the free-surface elevation and potential can be shown to be proportional to one of ϕ_x, ϕ_z, and ϕ_{xz}. This equivalence is used to eliminate redundancy between candidate radiation conditions.

Plausible candidates for the radiation condition include requiring that far upstream:

(a) the free-surface elevation is zero,
(b) the vertical component of velocity is zero,
(c) the free-surface elevation decays exponentially, and
(d) the vertical component of velocity decays exponentially.

As the radiation condition is two constraints, a simple formulation requires that the given constraint is satisfied at two different points. A generalisation of this would be to require one of the above constraints to be satisfied at one point, while another constraint is satisfied at a second point. For the more general formulation, the two points need not be distinct. In the following, only the formulations where the same constraint is applied at two different points will be considered.

By equation (3.3), the formal definition of candidate radiation condition (a) can be shown to be

$$\phi_x - U = 0 . \tag{3.4}$$

Also, the formal definition of candidate (b) is

$$\phi_z = 0 . \tag{3.5}$$

In order to determine formal definitions of radiation conditions (c) and (d), it is useful to consider the nature of a function, f, that decays exponentially at the rate $-n$ as x decreases. That is,

$$f = A(-x)^{-n} . \tag{3.6}$$

Its derivative, f_x, has the form

$$f_x = nA(-x)^{-n-1} = -\frac{n}{x} f , \tag{3.7}$$

which can be rearranged to yield

$$x f_x + n f = 0 . \tag{3.8}$$

In this form, the condition is independent of the constant A, and depends only upon the choice of decay rate n. Inherent in this formulation is the assumption that the disturber is located near $x = 0$.

Considering candidate condition (c), where the surface elevation decays exponentially, the function $f(x)$ can be replaced by the perturbation to the horizontal component of velocity, $\phi_x - U$, and so

$$x\phi_{xx} + n(\phi_x - U) = 0 . \tag{3.9}$$

Making use of the proportionality between ϕ_{xx} and ϕ_z, this is equivalent to

$$kx\phi_z + n(\phi_x - U) = 0 , \tag{3.10}$$

where $k = g/U^2$ is the wave number. In this light, condition (c) is seen to be a combination of conditions (a) and (b). A consequence of this is that condition (c) with n chosen to be 0 is identical to radiation condition (b).

For candidate condition (d), the function is the vertical component of velocity, and so the formal definition is

$$x\phi_{xz} + n\phi_z = 0 . \tag{3.11}$$

Note that the rate of decay n is yet to be specified. In the following, for candidate radiation conditions (c) and (d), the value of n will be appended, so that, for example, condition (c2) refers to radiation condition (c), with $n = 2$.

3.2.2 TESTING OF THE CANDIDATE RADIATION CONDITIONS

In order to evaluate the effectiveness of the candidate radiation conditions, it is necessary to eliminate or reduce all possible sources of inaccuracies to as great an extent as is practicable. In Chapter 2, the accurate representation of the potential and free surface for a wave was discussed, and so the remaining concerns are representation of the domain of simulation, choice of iterative procedure, and representation of the body, as well as the selection of an appropriate error measure by which the performance of any particular radiation condition can be measured.

The error introduced by domain truncation can be reduced by using a domain that extends far upstream and downstream in comparison to both the wavelength and the size of the body. The effects of domain truncation will be investigated in Section 3.3.

The iterative procedure, provided it is correct in its formulation and implementation, should have negligible effect upon the solution. Consequently, it should have no effect on the ability of a candidate radiation condition to select the particular desired solution.

One can remove any errors that might otherwise be introduced by the presence of a body (for example, the inaccuracies associated with representing the body itself) by replacing the body with a dipole. In an infinite fluid the dipole reproduces a circular cylinder, and beneath a free surface the dipole produces a close approximation (although Tuck [37] showed that no closed body is produced). This simplification also has the advantage that the exact solution to the linearised problem is known, and can be used as an approximation to the solution of the nonlinear problem, from which suitable error measures can be derived. Such an approach is valid if the nonlinear effects are small, but this could be difficult to verify.

If however, the numerical solution of the *linearised* problem is sought, then the solution can be used for direct comparison. Another advantage is the removal of the iterative procedure, resulting in reduced computational effort, as the linear solution can be determined by a single inversion of a set of simultaneous linear equations.

3.2.3 THE LINEAR THEORY FOR A SUBMERGED DIPOLE

The exact solution for the potential of a flow about a submerged horizontal dipole and satisfying the linearised free-surface condition is well known. Havelock [16, page 26] restated the wave resistance of the dipole, which in the present notation is

$$R = \rho k^3 \mu^2 e^{-2F^{-2}} , \tag{3.12}$$

where ρ is the fluid density, μ is the moment of the dipole, and $F = U/\sqrt{gf}$ is the Froude number of the flow as based upon the depth f of the dipole.

The lift is also given by Havelock [15, page 391], and is

$$L = -\frac{\rho \mu^2 k^3}{8\pi} \left\{ F^6 + 2F^4 + 4F^2 - 8e^{-2F^{-2}} \mathrm{Li}\left(e^{2F^{-2}}\right) \right\} , \tag{3.13}$$

where Li is the logarithmic integral.

These formulae are suitable for use as the basis for error measures by which the effectiveness of candidate radiation conditions can be determined. In particular, reasonable error measures are the absolute values of the relative errors of the numerically determined force components.

3.2.4 THE TEST PROCEDURE

The effect of density is linear with respect to the forces and has no effect upon the solution potential. Variations in the dipole moment have a linear effect upon the perturbation potential and free surface, and an associated quadratic effect on the force. Each member of this class of problems can be identified by its Froude number as controlled by depth of submergence, f, with all other variations in ρ, μ, U and g only producing differences in scale. Therfore, without loss of generality, ρ, μ, U and g are held fixed at unity. In testing the candidate radiation conditions, Froude numbers of 0.5, 1.0 and 1.5 will be used.

As the boundary condition is to be applied upon the surface $y = 0$, it is consistent with the results of Section 2 to use 48 points per wavelength, with an offset height of 0.75 (which produces an offset height ratio near 6.0) and an offset shift of zero, in order to accurately represent the potential.

It is anticipated that a domain that extends 10 wavelengths upstream of the dipole, and another 10 wavelengths downstream is adequate for the current purposes. The error introduced by this assumption will be investigated in Section 3.3.

The accuracy of the solution is to be determined with respect to the influence of the choice of candidate radiation condition, and the two locations at which the constraint is to be enforced.

For candidate radiation conditions (c) and (d), it is reasonable to investigate the influence of integer values for n, ranging from 0 to 4. Thus there are in effect 11 distinct candidate radiation conditions to test, being (a), (b), (c1)–(c4), and (d0)–(d4).

The points at which the radiation condition is to be satisfied will be referred to as radiation condition implementation points 1 and 2, with point 1 being the furthest upstream. In principle, any points on the upstream portion of the free surface could be selected, but in the current test, the locations will be restricted to free-surface collocation points. Further, only those points that are a distance of one of 0, $\lambda/8$, $\lambda/4$, $\ldots$, λ from the upstream end of the domain will be used. As there are 48 points per wavelength, these implementation points correspond to nodes 1, 7, 13, ..., 49, the nodes being numbered from one, starting furthest upstream. These restrictions lead to 36 possible combinations.

As a technical matter, the additional two constraints create an imbalance between the number of conditions and the number of unknowns in the system of simultaneous linear equations. The method used to overcome this minor difficulty is to remove two of the surface collocation points, one at the upstream end of the domain, and one downstream.

For each of the three Froude numbers, each of the eleven candidate radiation conditions is applied using each of the 36 possible combinations of locations for enforcement. The solution potential is determined, and the lift and drag calculated by implementation of the Lagally theorem.

3.2.5 Force Calculations by the Lagally Theorem

The Lagally theorem is based upon the strengths and locations of the singularities that reproduce the potential, and is exact for the determined potential. In particular it is independent of the free-surface shape, which removes the possibility of errors that might otherwise be introduced by a surface determining procedure.

Robertson [32, p. 200] states the theorem as follows. "The force on a body in the presence of a source is equal to the product of the fluid density, the strength of the source, and the velocity induced at the location of the source by all causes except the source. The line of action of the force is through the source, and its direction is that of the induced velocity."

Milne-Thomson [27, p. 217] gives a simple derivation of the theorem for two-dimensional sources, from which it becomes clear that the stream velocity is not to be considered as a "cause", and therefore is not to be included when determining the velocity at the source. In addition, the derivation lends itself easily to the determination of forces due to other singularities, including vortices and dipoles. For vortices, the line of action is perpendicular to that of the induced velocity (that is, it is rotated anticlockwise by $\pi/2$). For dipoles, the interest is in the derivatives of velocity, and for two-dimensional panels of sources or vortices, the velocity potential and stream function are required.

The power of the theorem lies in the fact that the force on a body is simply the sum of all forces acting on the body due to singularities located external to it. In addition, there could be a component of vertical force associated with a circulation about the body, due to vortices contained within it.

In testing, there was found to be strong consistency between the forces as determined by the Lagally theorem, and those determined by integration of pressure over the body's surface. Given the relative ease with which the Lagally theorem can be applied to bodies of complex geometry, it is the method of force calculation that is used throughout this thesis.

3.2.6 RESULTS OF THE TEST PROCEDURE

The absolute value of the relative error is determined using the exact value for both drag and lift as given in equations (3.12) and (3.13) respectively, and the results are displayed as surface plots using a base-10 logarithmic scale. There are 33 graphs for each of drag and lift, based upon combinations of Froude number and candidate radiation condition, but only a representative sample is reproduced here for discussion.

In general, the radiation condition formulations perform well. There are, however, consistent differences between them. The accuracy of the various formulations is relatively independent of the locations of implementation points 1 and 2, except for one specification. The distance between the points at which the radiation conditions are enforced must not be an integer multiple of a half-wavelength, or a distance near these.

The more successful formulations are (b) and (d), and it is interesting to note that the accuracy of formulation (d) appears to be largely independent of the choice for decay rate. Formulations (a) and (c) prove to be somewhat poorer.

3.2.6.1 FROUDE NUMBER 1.5

Figures 3.1 and 3.2 make clear the distinction between the accuracies achieved by the radiation condition formulations. In each figure, the left half of the graph, including axes, represents the error in the drag force, while the right axes are to be used when interpreting the results for the lift.

The relative error in both the drag and lift for formulation (a) are displayed in Figure 3.1. Both forces show considerable variation in accuracy, with the most accurate values being of the order of 10^{-3}, which indicates four-figure accuracy, and the least accurate values having a relative error of the order of 1.

By comparison, formulation (d0), displayed in Figure 3.2, has a relative error for drag of the order of 10^{-4}, indicating accuracy to five significant figures. For lift, there is close to seven-figure accuracy. There is only minor variation of error with respect to the choices of implementation points 1 and 2.

Analysis of the other candidate radiation conditions for this Froude number shows formulation (b) produces results that are similar to (d). For formulations (c1)–(c4), there is a gradual degradation in accuracy as n is increased, with (b) being better than (c1), which is better than (c4), which is better than (a). There is little variation within the results for (d0)–(d4).

3.2.6.2 FROUDE NUMBER 1.0

Similar trends are seen at Froude number 1.0. Figure 3.3 shows the accurate results obtained using scheme (b). Figure 3.4 shows the poorer results delivered by scheme (c4). Again, the gradual increase in error in the results for (c) as n is increased is observed. This is of particular interest because of the relationship between the two classes of condition (b) and (c). As noted previously, the formulation (c0) is identical to (b), and the formulations (c1)–(c4) are in a sense a combination of formulations (a) and (b). It appears that the poorer behaviour of formulation (a) is the detrimental component of the class of radiation conditions (c), and it is this influence that becomes stronger as n is increased.

Note that at this Froude number, drag is obtained to at least four-figure accuracy, while lift is accurate to about five significant figures.

Ridges of increased error are displayed clearly for both drag and lift in both of these

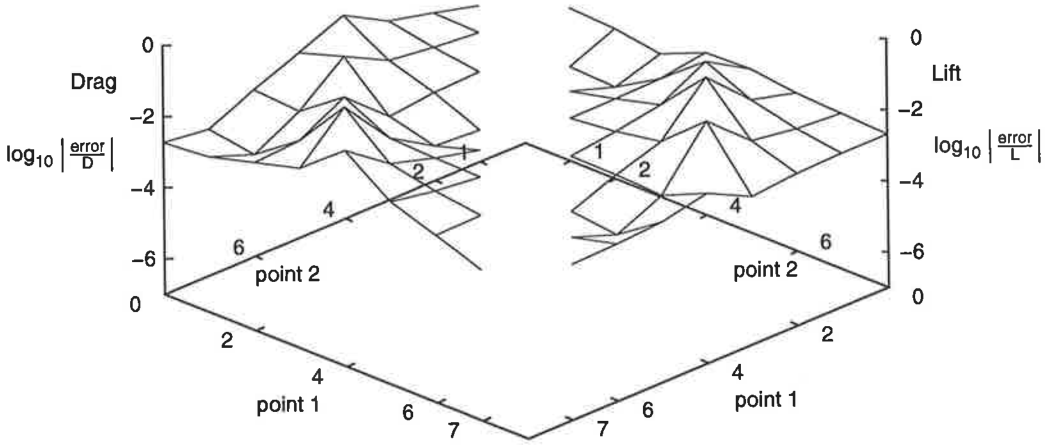

Figure 3.1: Error measures for drag and lift on a submerged dipole, using radiation condition formulation (a). The Froude number is 1.5. The left half (including axes) represents drag, and the right half represents lift.

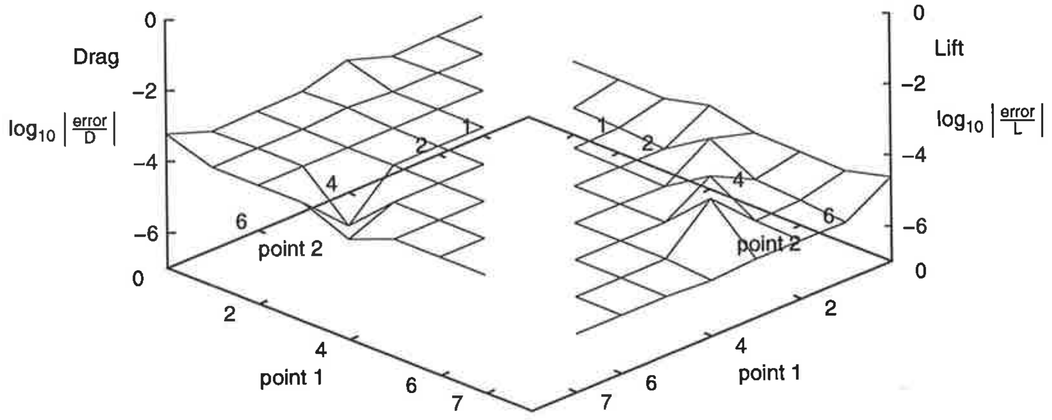

Figure 3.2: Error measures for drag and lift on a submerged dipole at Froude number 1.5, using radiation condition formulation (d) with decay rate $n = 0$.

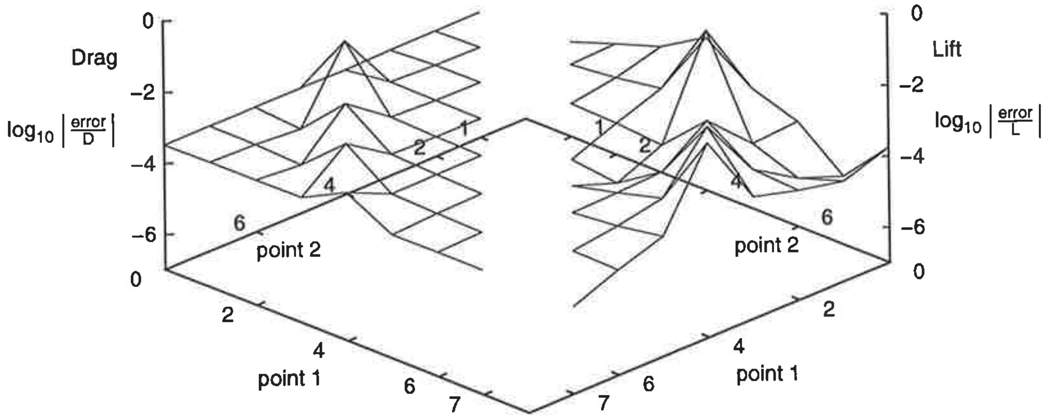

Figure 3.3: Radiation condition formulation (b) at Froude number 1.0. Note the ridges of increased error, which correspond to a half-wavelength separation between implementation points 1 and 2.

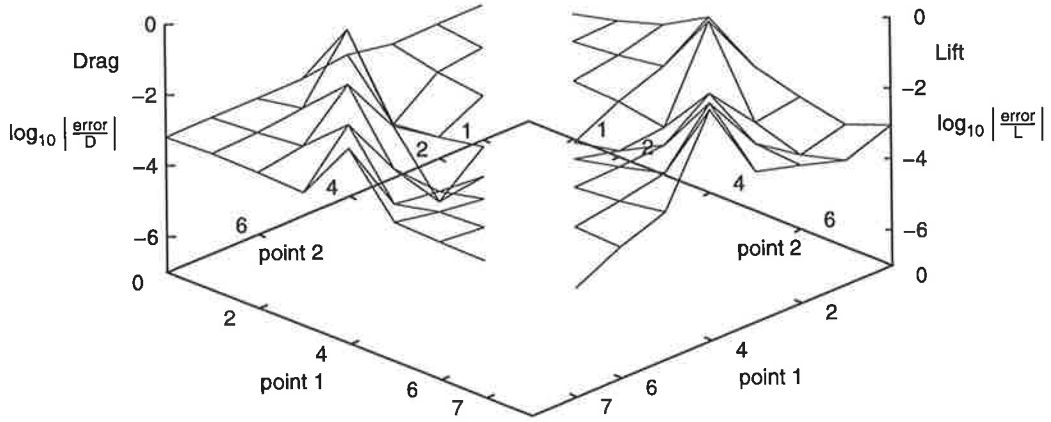

Figure 3.4: Results for radiation condition formulation (c4) at Froude number 1.0, displaying increased error in comparison to formulation (b).

graphs, and they coincide with the particular choices of implementation points 1 and 2 such that they are separated by a half-wavelength. In effect, if a particular candidate condition is satisfied at one point, then it is also nearly satisfied at points distributed at half-wavelength intervals from there. In essence then, enforcing the same condition at any of these points is redundant, and the associated degree of freedom results in a solution that has waves upstream, and hence a larger error.

3.2.6.3 FROUDE NUMBER 0.5

Figures 3.5 and 3.6 show the results obtained by conditions (a) and (d3) respectively. Recall that there is little difference for formulation (d), regardless of the choice of n, and so Figure 3.6 is indicative of the results for the formulations (d0)–(d4).

For formulation (d), there is insignificant variation of error with respect to the choices of implementation points 1 and 2. In particular, the ridges associated with a separation of a half-wavelength are not represented. This lack of variation is an indication that the accuracy is being limited by some other factor. It will be shown in Section 3.3 that the limiting factor is the truncation of the domain in the downstream direction.

3.2.7 EFFECTIVENESS OF THE CANDIDATE RADIATION CONDITIONS

The conclusion is that candidate formulations (a) and (c1)–(c4) are less successful in selecting the particular solution that does not have waves upstream. By comparison, conditions (b) and (d0)–(d4) behave well. There is little difference in the performance for formulation (d) with the different choices for the rate of decay n. Similarly, the accuracy that is achieved is independent of the locations at which the constraints are implemented, provided that they are not separated by an integer multiple of a half-wavelength.

A recurring pattern in the graphs for successful radiation conditions is that there is a minimum error achieved, and a lack of variation from this value. This suggests strongly that something other than the particular radiation condition being enforced is the limiting factor in attaining accuracy. It will be shown in the next section that the limiting factor is the length of the computational domain.

At this stage, there appears to be no consistent and significant difference on which to base a strong preference between the case (b) or the class (d).

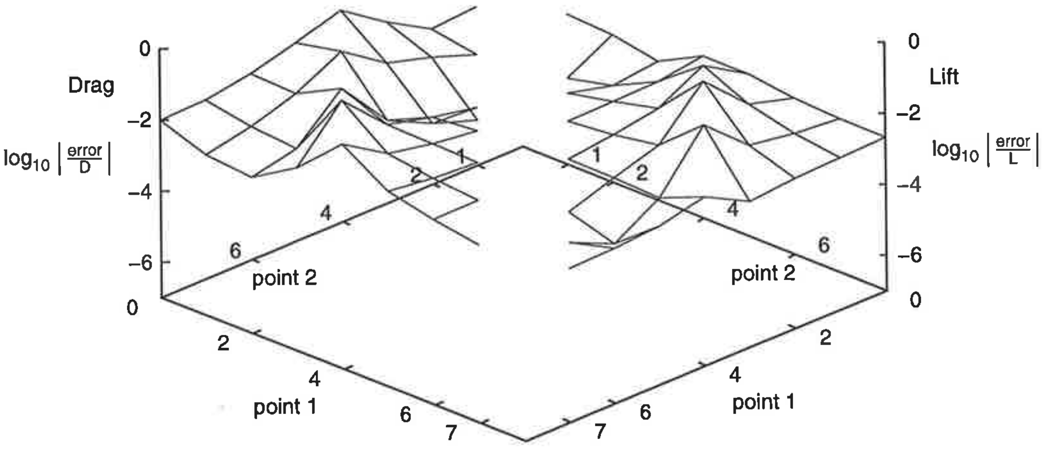

Figure 3.5: Radiation condition formulation (a) at Froude number 0.5.

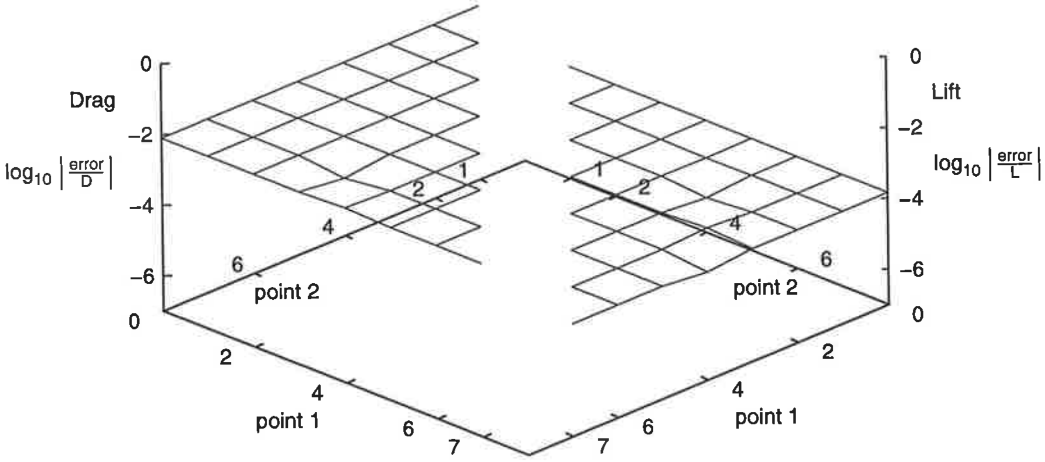

Figure 3.6: Radiation condition formulation (d) with n = 3 at Froude number 0.5. The lack of variation in the error suggests some other factor is limiting the obtainable accuracy.

3.3 TESTING THE EFFECTS OF DOMAIN TRUNCATION

It was the premise of the previous section on the formulation and application of the radiation condition, that a domain stretching from ten wavelengths upstream of the disturber to ten wavelengths downstream, is adequate for the successful implementation of the radiation condition. On this basis, it was possible to determine successful radiation conditions, and to reject less appropriate formulations. It is the aim of this section to investigate the error that is introduced by a truncated computational domain.

The appropriate test is straight-forward to design and implement. Again, a dipole submerged beneath a linearised free-surface is considered. Relative errors in the forces for drag and lift are determined, and their variation with the distance of domain truncation investigated.

For each Froude number 0.5, 1.0 and 1.5, the successful radiation conditions (b) and (d0)–(d4) were applied at implementation points 1 and 3, for a domain that extended ten wavelengths upstream. The distance of downstream truncation was varied from between $\lambda/8$ to 10λ in intervals of $\lambda/8$, and the solution potential determined in each instance.

Another similar set of tests were also run, with the upstream domain varying in length, while the downstream domain length was kept constant at ten wavelengths.

The results are quite interesting. Firstly, for each Froude number, there is no significant difference in the drag between each of the six radiation conditions. Secondly, there are only insignificant differences in the lift between each of the radiation conditions (d0)–(d4), while there is a significant difference produced by the condition (b).

In the graphs that are to follow only two curves will be shown. One is the curve produced by radiation condition (b), and the other is produced by condition (d2), with all other conditions of type (d) lying sufficiently close to this curve to warrant the simplification. In each instance, it is (b) that produces the poorer result. With this distinction in mind then, the curves are not individually labelled on the graphs.

3.3.1 FROUDE NUMBER 0.5

Figure 3.7 shows the four graphs of the base-10 logarithm of the absolute value of the relative errors for drag and lift as the domain length is varied in the upstream and downstream directions. In this case, the Froude number is 0.5. The figure is arranged such that

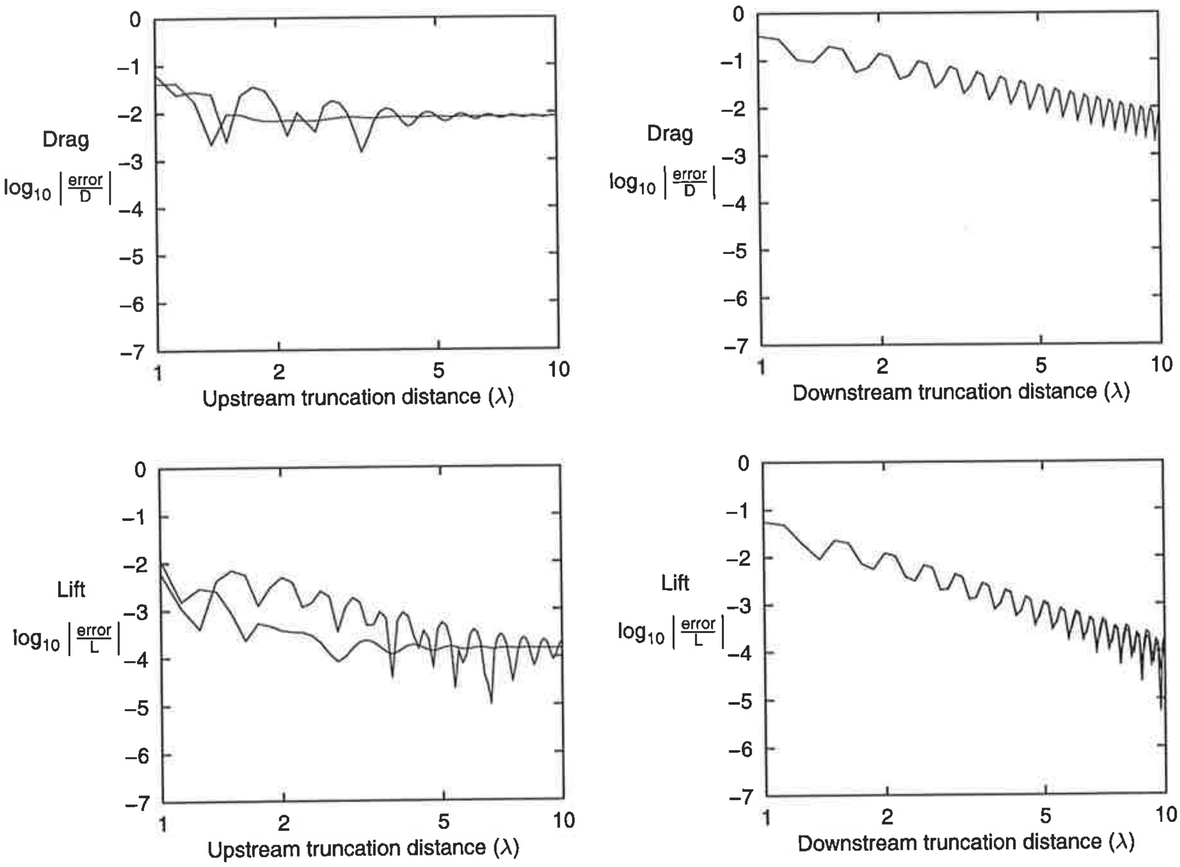

Figure 3.7: Relative errors in drag and lift as the domain length is varied in both the upstream and downstream directions. The Froude number is 0.5.

the top graphs represent drag, while the bottom graphs represent lift. In each case, the dependence upon variation in the upstream domain is the left graph, and the dependence upon the downstream length is the right graph. The four graphs should be considered in unison to accurately interpret the results. In addition, the horizontal axes are logarithmic, so as to facilitate the determination of exponential rates of reduction in error measures. Each curve shows an oscillation in error that is related to the phase at which the domain is truncated. Such an oscillation is to be expected, and it is the envelope produced by the maxima that is important here.

Observation of the graph for drag as it depends upon the upstream truncation, reveals a limitation on the accuracy attained for upstream domains of length longer than approximately two wavelengths. In comparison, the corresponding graph for downstream domain displays a *quadratic* rate of reduction in error as the domain length is increased. The consistent interpretation of these two graphs is that the downstream truncation is

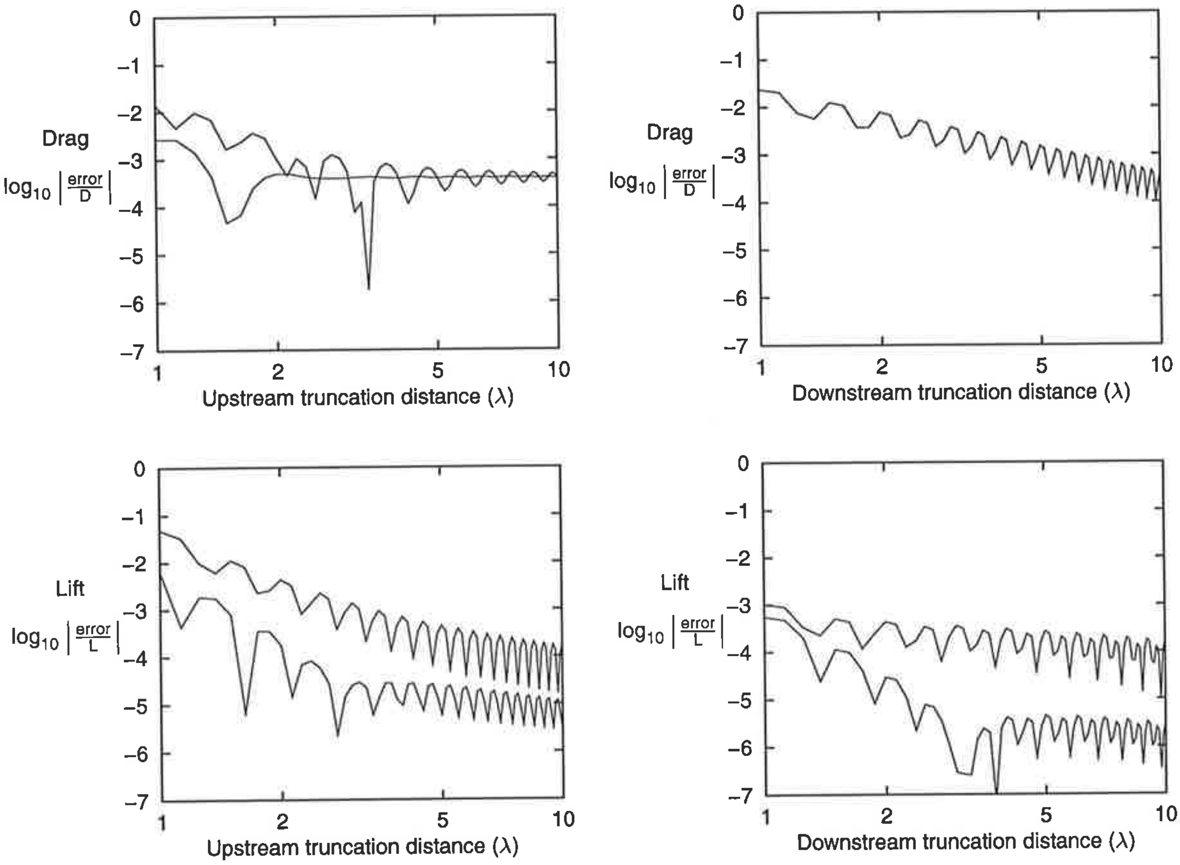

Figure 3.8: Relative errors determined for a Froude number of 1.0. The lift calculations reveal that the radiation condition is limiting the achievable accuracy.

limiting the achievable accuracy, and that in order to increase the accuracy, one would need to extend the downstream domain further.

Similar trends are observed in the graphs for lift, although the performance of radiation condition (b) is moderately poorer than that for (d), requiring a larger domain upstream to obtain results of the same accuracy. Also worthy of note is the *cubic* rate of reduction in error as the downstream domain length is increased.

3.3.2 FROUDE NUMBER 1.0

Figure 3.8 displays the results for Froude number 1.0. Again there is a clear quadratic rate of reduction in error for drag as the downstream domain is extended, and observation of the graph for upstream indicates that the length of downstream truncation is restricting the accuracy in the drag measurement.

The graphs for lift are particularly interesting. They display large differences between the different radiation conditions. It is clear from the downstream truncation graph that the accuracy acquired by both radiation conditions is limited by some other factor well before the end of the ten-wavelength range tested. Similarly, the accuracy is limited for the upstream graph. The limiting accuracy that is achieved is significantly different for the two different radiation condition formulations, being of the order of 10^{-4} for formulation (b), and 10^{-5} for formulation (d2). The conclusion is that the accuracy achieved is not restricted by the length of downstream truncation, nor the length of upstream truncation, but it is limited by the ability of the *radiation condition* to diminish the amplitude of the waves upstream. In each case, the radiation condition has selected a solution that has very small waves upstream, as opposed to none, and it is this inaccuracy that is dominating the calculations.

3.3.3 FROUDE NUMBER 1.5

Figure 3.9 displays the error measures for Froude number 1.5.

They are essentially similar in behaviour to the previous case, where the Froude number was 1.0. For drag, there is a quadratic reduction in error as the downstream truncation distance is increased, and at ten wavelengths, this error is the dominating factor. The graph for upstream truncation indicates that radiation condition (d2) behaves better than (b), as it reached its limiting accuracy when the upstream domain is only two wavelengths in length.

For the lift, it is again the actual radiation conditions that are the limiting factor, with accuracies of $10^{-4.5}$ being achieved by condition (b), and $10^{-5.5}$ being achieved by condition (d2).

3.3.4 SUMMARY OF THE EFFECTS OF DOMAIN TRUNCATION

In general the drag displays a quadratic rate of decrease in error as the downstream domain is increased in length. For drag calculations, it is the downstream length that is the limiting factor in determining the force accurately.

For lift, which for all these cases is more accurate than the drag, the limiting factor for both Froude number of 1.0 and 1.5 is the ability of the radiation condition to reduce the amplitude of the upstream wave. For the remaining case of Froude number 0.5, a

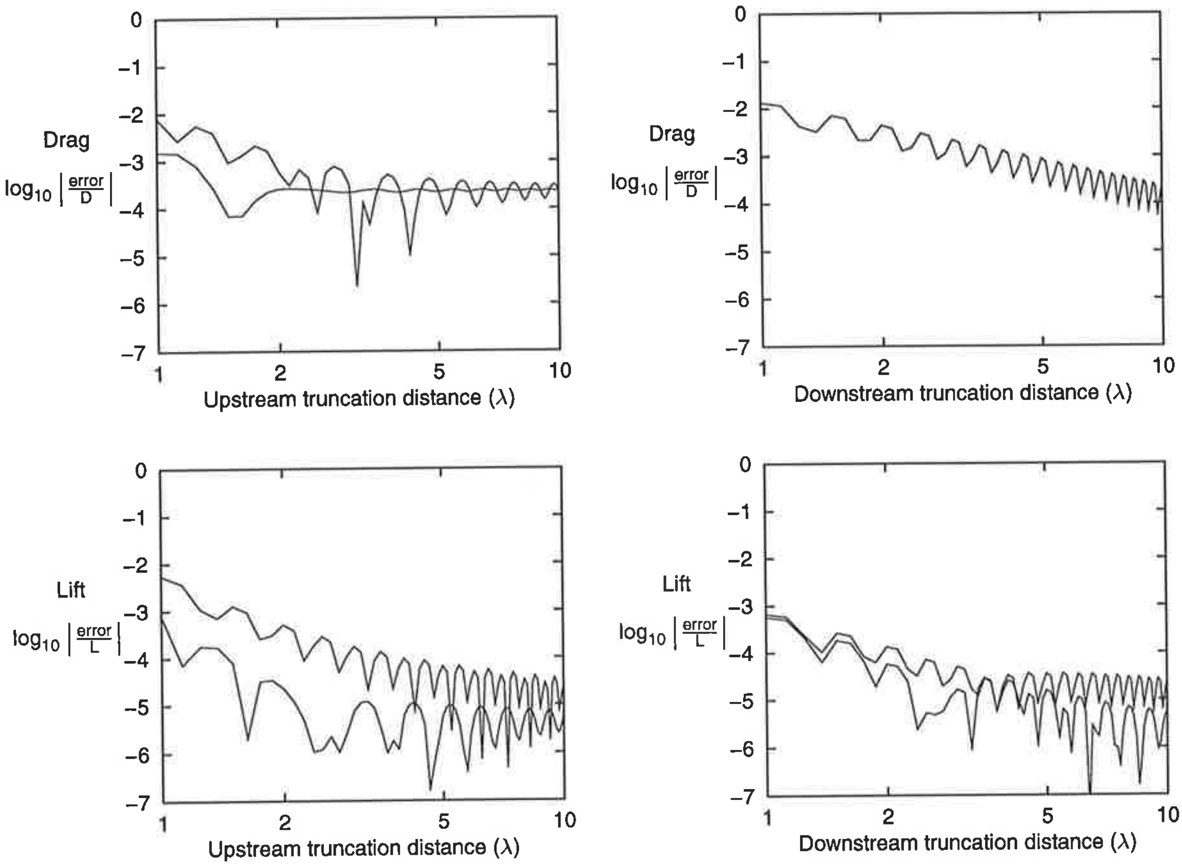

Figure 3.9: Relative errors in drag and lift as the domain length is varied in both the upstream and downstream directions. The Froude number is 1.5.

cubic rate of decay in error is observed, and the length of downstream truncation is the limiting factor.

In none of the three cases was it the length of the upstream domain that was the limiting factor in achieving results of high accuracy.

3.4 CONCLUSION

Radiation conditions of the class (d) are more successful in selecting the particular solution which does not have waves far upstream, than is radiation condition formulation (b), which is superior to the other alternatives considered. Formulation (d) is based upon the exponential decay in the upstream direction of the vertical component of fluid velocity. Accuracy appears to be reasonably independent of the rate at which the vertical velocity is required to decay.

The condition can be enforced at any two points near the upstream end of the computational domain with reasonable success, provided the two points are not separated by a length close to an integer multiple of a half wavelength.

Investigations of the effect of truncation of the computational domain indicate that the accuracy of the wave resistance is (for most of the examples tested) limited by the extent of the downstream domain. That is, the radiation condition is not the limiting factor. For the vertical component of force (for which the relative error is significantly less than that for the wave resistance), the formulation of the radiation condition is the limiting factor.

THE ITERATIVE PROCEDURE

Several possible algorithms for the iterative procedure are considered. The boundary condition formulations, surface update procedures, and singularity location schemes are assessed for their effects on the accuracy of the solution and the reliability and speed of the algorithm. Also, appropriate convergence criteria are defined.

4.1 INTRODUCTION

One of the difficulties associated with determining flows beneath a free surface is that the free surface is not known in advance, and yet an exact formulation requires that the free-surface boundary conditions are satisfied on it. The standard method of dealing with this is to adopt an iterative procedure whereby successive refinement of an approximation is used to determine the actual free surface.

An initial approximation is made for the free surface, and certain conditions are enforced upon this boundary. The potential that satisfies these conditions is determined, as is a better free-surface approximation. This procedure is repeated until the appropriate free-surface boundary conditions are satisfied to within a desired tolerance, at which stage it is claimed that the solution potential and free surface have been determined.

4.2 THE COMPONENTS OF AN ITERATIVE SCHEME

This process can be described by four components. The first is the condition that is to be enforced on the approximate free surface. The second is the method by which the new free-surface approximation is determined. It may be preferable to allow the singularities to shift between successive iterations of the procedure, and the process of determining their locations is the third component of the iterative procedure. The final component is the test by which convergence is established.

4.2.1 FREE-SURFACE BOUNDARY CONDITIONS

The boundary conditions that are to be satisfied on the free surface are

$$\frac{Dp}{Dt} = 0 \qquad \text{and} \tag{4.1}$$

$$p = 0\,, \tag{4.2}$$

on $\zeta = \zeta^*$ with $\phi = \phi^*$. Here $\frac{Dp}{Dt}$ is the material derivative of pressure, ζ^* represents the free-surface solution, and ϕ^* represents the solution potential. The physical interpretation of equation (4.1) is that the free surface is both a streamline and an isobar. The second condition, (4.2), requires that the excess pressure on the isobar is zero. Clearly, together they prescribe a free surface.

From this, one can immediately suggest several conditions to enforce on the approximate free surface, in order to evaluate the potential and a better free-surface approximation.

For clarity, the following notation is introduced. The free-surface approximation on which the boundary condition is to be enforced is denoted by ζ^0, and the refinement to this approximation is ζ^1, so that $\zeta^0 + \zeta^1$ is a better approximation to ζ^* than is just ζ^0.

One simple scheme is to use the condition

$$\frac{Dp}{Dt} = 0 \qquad \text{on} \qquad \zeta = \zeta^0\,. \tag{4.3}$$

In the following, this will be referred to as boundary condition formulation 1.

A second scheme is to use the condition

$$p = 0 \qquad \text{on} \qquad \zeta = \zeta^0\,, \tag{4.4}$$

and will be termed boundary condition formulation 2.

A more sophisticated scheme involves applying a combination of the two conditions. A truncated Taylor series expansion of $\frac{Dp}{Dt} = 0$ (as evaluated at the solution) in the free-surface elevation shows

$$\frac{Dp}{Dt} + \zeta^1 \frac{\partial}{\partial \zeta} \frac{Dp}{Dt} \approx 0 \qquad \text{on} \qquad \zeta = \zeta^0 \,, \tag{4.5}$$

and similarly, the expansion of $p = 0$ yields

$$p + \zeta^1 \frac{\partial}{\partial \zeta} p \approx 0 \qquad \text{on} \qquad \zeta = \zeta^0 \,. \tag{4.6}$$

Eliminating ζ^1 from these, neglecting terms in the approximation which are of order $\mathrm{O}((\zeta^1)^2)$, and rearranging, yields the combined condition

$$\frac{Dp}{Dt} \frac{\partial}{\partial \zeta} p - p \frac{\partial}{\partial \zeta} \frac{Dp}{Dt} = 0 \qquad \text{on} \qquad \zeta = \zeta^0 \,. \tag{4.7}$$

This is boundary condition formulation 3.

A fourth formulation is to use both free-surface conditions *simultaneously* with the first-order transfer terms included. That is,

$$p + \zeta^1 \frac{\partial}{\partial \zeta} p = 0 \qquad \text{and} \tag{4.8}$$

$$\frac{Dp}{Dt} + \zeta^1 \frac{\partial}{\partial \zeta} \frac{Dp}{Dt} = 0 \qquad \text{on} \qquad \zeta = \zeta^0 \,. \tag{4.9}$$

Under this scheme, the perturbation to the approximate free surface is determined automatically. The simple formulation of this scheme presumes that the singularities remain fixed in their location. As such, the only influence on the boundary conditions is due directly to the free surface shifting. This is boundary condition formulation 4.

A more complicated version of this process is to presume that there is a vertical linking system between nodes and singularities. In this case, any modification to the free surface has a two-fold effect. Firstly, that which is due directly to the change in free-surface elevation, and secondly that due to the associated change in the potential representation as the singularities are shifted. This will be referred to as boundary condition formulation 5, and the concept of vertical linking will be dealt with in greater detail in Section 4.2.3.

A further extension is to account for the effects on the boundary conditions where the singularities are normally-linked to the free-surface nodes. This formulation is quite complicated, and is not considered further. Again, a clarification of normal linking will be given later.

In summary then, there are five different boundary-condition formulations that will be considered here.

(1) The material derivative of pressure free-surface condition, $\frac{Dp}{Dt} = 0$.

(2) The dynamic free-surface condition, $p = 0$.

(3) The combined condition, $\frac{Dp}{Dt}\frac{\partial}{\partial\zeta}p - p\frac{\partial}{\partial\zeta}\frac{Dp}{Dt} = 0$.

(4) The extended system in which both the potential and free-surface are determined simultaneously using both $p + \zeta^1\frac{\partial}{\partial\zeta}p = 0$ and $\frac{Dp}{Dt} + \zeta^1\frac{\partial}{\partial\zeta}\frac{Dp}{Dt} = 0$. This formulation presumes that there is no linking between the free-surface nodes and the singularities.

(5) The extended system which presumes that the singularities are linked to nodes in the vertically-linked sense, but otherwise is similar to boundary condition formulation 4.

Note that these boundary conditions are to be satisfied by the solution potential ϕ^*, but that within the iterative procedure, only an approximation to the desired potential will be known. An iterative procedure involving successive refinement of the potential (without modification of the free-surface approximation) could be implemented to determine the potential to a desired tolerance. However, significant savings in computational effort can be gained if one presumes that an approximation to the potential is satisfactory when determining the new free-surface approximation. The potential approximation is refined as the free-surface approximation is, so that eventually both are satisfactory.

4.2.2 SURFACE UPDATE PROCEDURES

Three possible methods by which the new free-surface approximation can be determined are:

(1) based upon the dynamic free-surface boundary condition,

(2) based upon the material-derivative free-surface boundary condition, and

(3) to directly determine it as part of the potential solution procedure.

In the first method, use is made of a truncated Taylor series expansion of the pressure as a function of free-surface elevation. If the free-surface approximation for which the potential has been determined is ζ^0, and on this approximate surface the pressure is non-zero, then a surface on which the pressure is closer to zero can be determined from equation (4.6), and is given by

$$\zeta = \zeta^0 - p \Big/ \frac{\partial}{\partial \zeta} p \,, \tag{4.10}$$

the pressure and its derivative being evaluated on the free-surface approximation ζ^0.

Similarly, under the second method, the new free-surface approximation can be obtained from equation (4.5), and is

$$\zeta = \zeta^0 - \frac{Dp}{Dt} \Big/ \frac{\partial}{\partial \zeta} \frac{Dp}{Dt} \,. \tag{4.11}$$

In the third method, the system of equations, (4.5) and (4.6), that is solved when enforcing the approximate free-surface boundary condition also determines the free-surface elevation $\zeta^0 + \zeta^1$ on which the boundary conditions are better satisfied. Consequently, the new free-surface approximation is automatically determined as part of the boundary condition enforcement process.

4.2.3 SINGULARITY LOCATION SCHEMES

As mentioned in the introduction, it may be advantageous to shift the singularities between iterations of the solution procedure. Three distinct possibilities for determining their locations will be considered here. They are

(1) fixed singularities,
(2) vertically-linked singularities, and
(3) normally-linked singularities.

The first of these is trivial, in that the singularities are fixed in their location and are therefore independent of the free surface. Their locations are supplied at the outset, and never change.

The second method is slightly more sophisticated. The singularities are "linked" to free-surface nodes, and any change in the surface elevation is reflected by a similar shift in the height of the associated singularities. In general the linking is such that any number (including zero) of singularities may be associated with a given node. The only restriction is that a singularity cannot be associated with two or more nodes. Not all singularities need to be associated with nodes, and vice-versa. As changes in the free-surface elevation influence only the vertical location of the singularities, they are said to be vertically-linked. Note also that this says nothing about the relative locations of a singularity and the node to which it is associated. In practice however, each singularity is linked to the free-surface node directly below it. Those at the extremes of the domain are linked to the end nodes.

The third method is to locate singularities along normals to the free surface. The distance along the normal remains constant between free-surface approximations, and is determined from the initial locations. The locations of the singularities at the edges of the domain are determined by presuming extensions to the free surface, with the same slopes as the end segments. This is the normally-linked singularity location scheme.

These three methods are likely to have distinct relative advantages and disadvantages. Firstly, there is likely to be an effect on the accuracy of the potential for the solution. It was shown in Chapter 2 that for waves of large amplitude it is preferable to have singularities located along normals to the free surface. This can only be achieved by the normally-linked scheme. The second preference is for the singularities to be located above the nodes, but at a set distance so that they follow the shape of the free surface. This can be achieved by the vertically-linked scheme. However, the process of shifting the singularities may prove to be disruptive to the iterative process, possibly resulting in either a decreased rate of convergence, or even the failure to obtain a converged solution. It is anticipated that the effects will be most pronounced in the normally-linked scheme as it is that scheme which shifts the singularities the most. Consequently, the schemes that are most likely to behave well in the iterative process may well result in a potential representation of decreased accuracy, and vice-versa.

4.2.4 CONVERGENCE CRITERIA

The iterative scheme is declared to have converged to a solution when the appropriate criterion is met for each of the free-surface boundary conditions.

The dynamic boundary condition is considered to be satisfied when the absolute value of pressure at all of the free-surface nodes is less than a prescribed tolerance. For the current purposes, this tolerance is set to $10^{-8}\left(\zeta_{\max}-\zeta_{\min}\right)g$. Here, $\zeta_{\max}$ represents the maximum elevation of the free-surface, and $\zeta_{\min}$ is the minimum, so that $\zeta_{\max}-\zeta_{\min}$ is an approximation of the wave height. A variation in pressure of approximately $\left(\zeta_{\max}-\zeta_{\min}\right)g$ will be observed along any horizontal line near the free surface. Thus, the term indicates that a *relative* error in excess of approximately 10^{-8} of the wave height will not be tolerated in the free-surface nodes' elevations. Note that this criterion has dimensions the same as those for pressure, and therefore scales appropriately.

For clarity of reference, the tolerance as defined above will be termed the absolute pressure tolerance, in comparison to the relative pressure tolerance, which in the above is 10^{-8}. It is generally more convenient to refer to relative tolerances.

A similar criterion is required for the boundary condition that is based upon the material derivative of pressure. In this instance, the tolerance is set to $10^{-8}\,(\zeta_{\max} - \zeta_{\min})\,g^2/U$. A variation in $\frac{Dp}{Dt}$ of approximately $(\zeta_{\max} - \zeta_{\min})\,g^2/U$ will be observed on a horizontal line near the free surface, and so the condition can again be interpreted as one of the accuracy required by the free-surface nodes. This condition is dimensionally similar to $\frac{Dp}{Dt}$, and so, scales appropriately.

The iterative scheme is deemed to have failed if as a result of the surface update procedure, any free-surface node is positioned at an elevation greater than stagnation height.

As a practical matter, the iterative procedure is halted if neither convergence nor divergence occur before some maximum number of iterations. This value is set to 30 for the current purposes. In such an instance (which occurs only twice in the results that are to follow), it is possible to assess the history of the errors, in an attempt to determine the likelihood of obtaining a converged result.

4.2.5 ITERATIVE-SCHEME COMBINATIONS

The five boundary condition formulations, three surface update procedures and three singularity location schemes can be combined in various ways. Clearly, it is nonsensical to use the same condition when updating the free surface as that enforced on the approximation, as the result would be a boundary on which only the originally applied condition was satisfied, which would not be a free surface at all.

Sixteen meaningful possibilities are displayed in Table 4.1. In the following, these iterative schemes will be referred to as 1.1.1 etc., to indicate clearly their formulation. The first digit represents the boundary condition formulation, the second indicates the surface update procedure, and the last gives the singularity location scheme.

Boundary condition formulation	Surface update procedure	Singularity location scheme
1	1	1
1	1	2
1	1	3
2	2	1
2	2	2
2	2	3
3	1	1
3	1	2
3	1	3
3	2	1
3	2	2
3	2	3
4	3	1
4	3	2
4	3	3
5	3	2

Table 4.1: Combinations of boundary condition formulation, surface update procedure and singularity location scheme for various plausible iterative schemes.

Each of these iterative schemes can be expected to have different properties with regard to their ability to converge to the desired solution and the rate at which this convergence is achieved.

For example, one can anticipate a linear rate of exponential decay in the error for scheme 1.1.1. This scheme is based upon the use of boundary condition formulation 1 (equation (4.3)) on the approximate free-surface, followed by surface update procedure 1 (equation (4.10)) to determine the new free-surface approximation. A Taylor series expansion of the equation $\frac{Dp}{Dt} = 0$ (as evaluated at the solution) in the free-surface indicates that the error in boundary condition formulation 1 is of order $O(\zeta^1)$. The surface update procedure 1 is of order $O((\zeta^1)^2)$. Consequently, the combined procedure is first order in ζ^1, and hence the anticipated linear rate of exponential decay in the error.

A similar analysis to the above (with the only change being that the roles of p and $\frac{Dp}{Dt}$ are reversed) indicates that a linear rate of convergence can also be expected for iterative scheme 2.2.1.

By comparison, the boundary condition formulation 3 (equation (4.7)), has an error of the order of $O((\zeta^1)^2)$. Consequently, combining with either of surface update procedures 1 or 2 (to produce schemes 3.1.1 and 3.2.1 respectively) yields an iterative scheme that should display a quadratic rate of exponential decay in the error.

Similarly, boundary condition formulation 4 also has an error of order $O((\zeta^1)^2)$. Recall that under this scheme, the perturbation to the approximate free surface is determined automatically. Consequently, the scheme should have a quadratic rate of convergence.

These rates of convergence should apply if the singularities are held fixed throughout the solution process. As noted previously, shifting the singularities may reduce the rate of decay, so that more iterations are required to achieve convergence. In the cases of boundary condition formulations 3 and 4, the quadratic rate of convergence may be destroyed.

However, boundary condition formulation 5 is special in the sense that it has the effect of shifting the singularities in a vertically-linked manner built in, and a quadratic rate of convergence should result. Indeed, this is the sole purpose of this formulation, and also the reason why only singularity location scheme 2 is considered in conjunction with it.

Each iterative scheme eventually solves a system of linear equations. In the cases of boundary condition formulations 1, 2 and 3, this system is used to determine the potential, with the strengths of the singularities being the unknowns. Under boundary condition formulations 4 and 5, both the refinement to the potential and free surface are simultaneously determined, and the number of unknowns is increased by the number of nodes used to represent the free surface. This can potentially double the size of the system, and the associated computational cost of doing this may be considered to be the price of quadratic convergence.

By comparison, to achieve its quadratic rate of convergence, boundary condition formulation 3 requires the determination of higher-order derivatives of the potential.

4.3 TESTING FOR SPEED AND RELIABILITY

It is the purpose of this section to investigate the properties of convergence of these plausible iterative schemes, with the intention of drawing a conclusion as to which are most suitable for use, in terms of speed and reliability.

4.3.1 THE ITERATIVE-SCHEME TEST PROBLEM

The horizontal dipole submerged beneath a nonlinear free surface in a two-dimensional fluid again serves as a suitable test, this time for the properties of convergence for these candidate iterative schemes. In essence, the properties of the iterative scheme are independent of the actual disturber, but are likely to depend upon the steepness of the resulting wave. The submerged dipole removes any difficulties associated with the representation of the body, and provides an easy method for varying the wave steepness. In the previous chapters, reasonable choices with regard to domain length, free-surface resolution, singularity location and radiation condition have been established, and consequently adequate accuracy in the representation of the free surface and potential can be assured.

As noted before, the linear theory for a submerged dipole can be parameterised by a single dimensionless quantity, being the Froude number based upon the dipole's depth. As shown by equation (3.12) on page 38, the wave resistance is proportional to the square of the dipole's moment, and hence the amplitude of the resulting wave is directly proportional to the moment. Thus, varying the moment provides a simple mechanism by which the wave steepness can be controlled. For the nonlinear problem, the proportionality between moment and amplitude will not be direct, although a close correlation can still be anticipated.

It seems unnecessary to investigate the properties for more than one Froude number, since in a two-dimensional flow there is really only one parameter of interest, being the steepness of the waves produced. It is reasonable to expect that there would be some variation in the free-surface shape in the region of the body at different Froude numbers, but the downstream characteristics will be similar for waves of the same steepness, irrespective of Froude number (with the exception of phase). Consequently, in the results that are to follow, the Froude number is 1.0 throughout.

To establish the suitability of the various iterative procedures, several tests are employed. The first of these is to establish that a converged solution can be obtained at a modest wave amplitude. The second deals with the rate of convergence for different representations of the surface and potential, including the effects of singularity offset height, free-surface resolution, and domain length. The third test deals with the ability to capture waves of large steepness, for which the nonlinear effects are considerable.

4.3.2 CAPTURING A WAVE OF MODEST AMPLITUDE

The standard parameters adopted are $U = 1$ and $g = 1$, which in the linear theory gives a wavelength of 2π and a stagnation height of 0.5. The domain is of length 20π, with the dipole located beneath the centre of the region at depth 1.0. In each interval of length 2π, 48 nodes are used to represent the free surface. Discrete sources are positioned at an offset height of 0.6 above the initial free-surface approximation $\zeta^0 = 0$. The offset shift ratio is zero. The radiation condition (d2) is enforced at the two free-surface nodes at distances of $\pi/4$ and $3\pi/4$ from the upstream end of the domain.

A brief exercise was undertaken, in which it was found that a dipole of moment 0.1 produced a wave of amplitude approximately 0.075. It is considered essential that any nonlinear free-surface determining procedure should be able to capture the solution for this case. Each of the 16 iterative-scheme combinations of Table 4.1 were tested using a dipole of this moment. The results are shown in Table 4.2.

Of the 16 candidate iterative schemes, 10 are able to determine a converged solution. All of the 6 that do not converge use the surface update procedure 2. None of the successful 10 use this update procedure. The conclusion that is to be drawn is that to determine the new free-surface approximation using equation (4.11) produces divergent behaviour. That is, although the formulation is consistent, the update procedure is unstable.

With surface update procedure 2 removed as unusable, there then becomes a strict relationship between the boundary condition formulations and surface update procedures. Boundary condition formulations 1 and 3 must use surface update procedure 1, while formulations 4 and 5 must use procedure 3. Also, formulation 2 need not be considered further, since it requires the use of surface update procedure 2, and hence cannot provide a converged solution.

It is also worth noting that all 10 successful schemes produce free surfaces of the same

Iterative scheme combination	Converged solution obtained?
1.1.1	Y
1.1.2	Y
1.1.3	Y
2.2.1	N
2.2.2	N
2.2.3	N
3.1.1	Y
3.1.2	Y
3.1.3	Y
3.2.1	N
3.2.2	N
3.2.3	N
4.3.1	Y
4.3.2	Y
4.3.3	Y
5.3.2	Y

Table 4.2: Ability to converge to a solution for a dipole of moment 0.1 for each of the candidate iterative schemes. "Y" indicates a solution can be determined, "N" indicates a failure to converge.

shape, and that the force on the dipole is close to that expected from the linear theory, indicating that these are indeed the correct solutions.

4.3.3 CONVERGENCE RATES

Given that the iterative scheme does converge to a solution, it becomes of interest to determine the rate at which convergence is achieved. As previously noted, the singularity shifting scheme is likely to have some influence over this, as are the other parameters associated with representing the free-surface and potential.

4.3.3.1 RATES OF CONVERGENCE FOR A STANDARD TEST CASE

The same test case as for the previous section is used, although the dipole moment is doubled to 0.2, to enable a clearer distinction between the convergence properties of the iterative-scheme combinations to be made. The values of pressure and its material derivative are evaluated at each node for each iteration. These values represent the extent to which the free-surface boundary conditions are not satisfied, and therefore are suitable error measures for each iteration. Figure 4.1 shows the error measure for iterative scheme 3.1.1. One can see the overall decrease in error at the free-surface nodes with successive iterations. In general, the maximum error occurs either above the dipole (near $x = 0$), or at the downstream end of the domain, as is most obvious for $\frac{Dp}{Dt}$ at iteration 5. A quadratic rate of decay in the maximum error can be observed. The error in pressure at iteration 5 is limited by the precision to which the calculations can be determined.

The maximum absolute value of pressure and its material derivative for each iteration are displayed in Figure 4.2 for each of the four main candidate iterative schemes. These schemes are 1.1.1, 3.1.1, 4.3.1, and 5.3.2, and are the main candidates in the sense that the singularity location scheme being implemented is the one which is the most natural for the given boundary condition formulation, and hence should yield the greatest rate of convergence. Schemes 3.1.1 and 4.3.1 display clearly a quadratic rate of decay in the maximum error for successive iterations, and both obtain a converged solution in 5 iterations.

In contrast, scheme 1.1.1 shows a linear rate of convergence, with 11 iterations required to reach a satisfactory solution.

The curves for scheme 5.3.2 show poor linear rates of convergence, with considerable oscillation in the maximum errors, and requiring 21 iterations. The poor linear rate of convergence is quite surprising, since the boundary condition formulation takes into account the effect of shifting the singularities in a vertically-linked manner, and a quadratic rate of convergence could have been expected.

The author suspects that the additional terms in the system introduced by this formulation introduce a destabilising effect and destroy the quadratic rate of convergence. This conclusion is supported by the observation that the scheme 4.3.2 shows a near-quadratic rate of convergence, with the only difference being the removal of these terms. Also, there

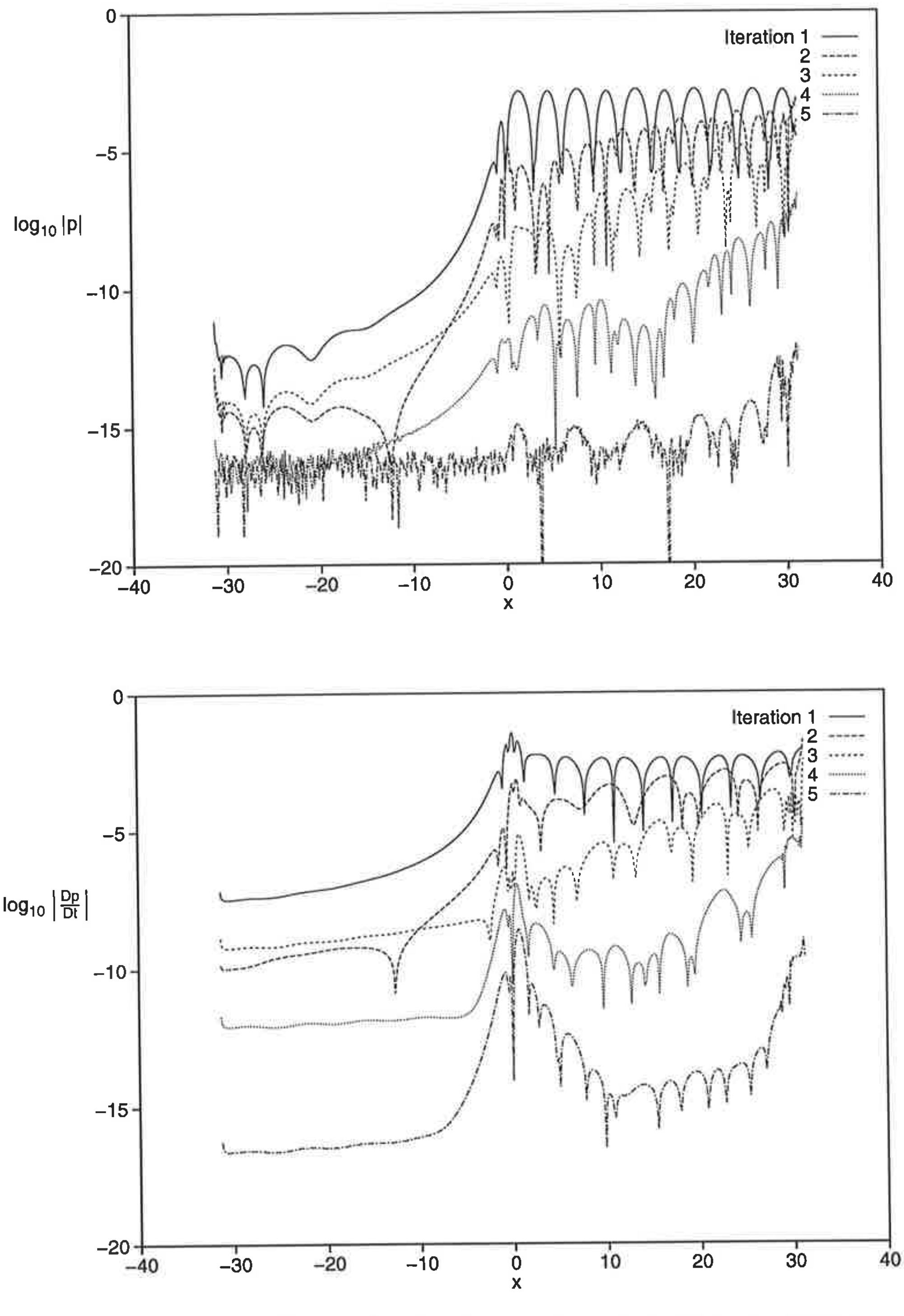

Figure 4.1: Errors in the free-surface boundary conditions at each node for successive iterations under iterative scheme 3.1.1. Note that the maximum error occurs either above the dipole or at the downstream end of the domain, and shows a quadratic rate of decay.

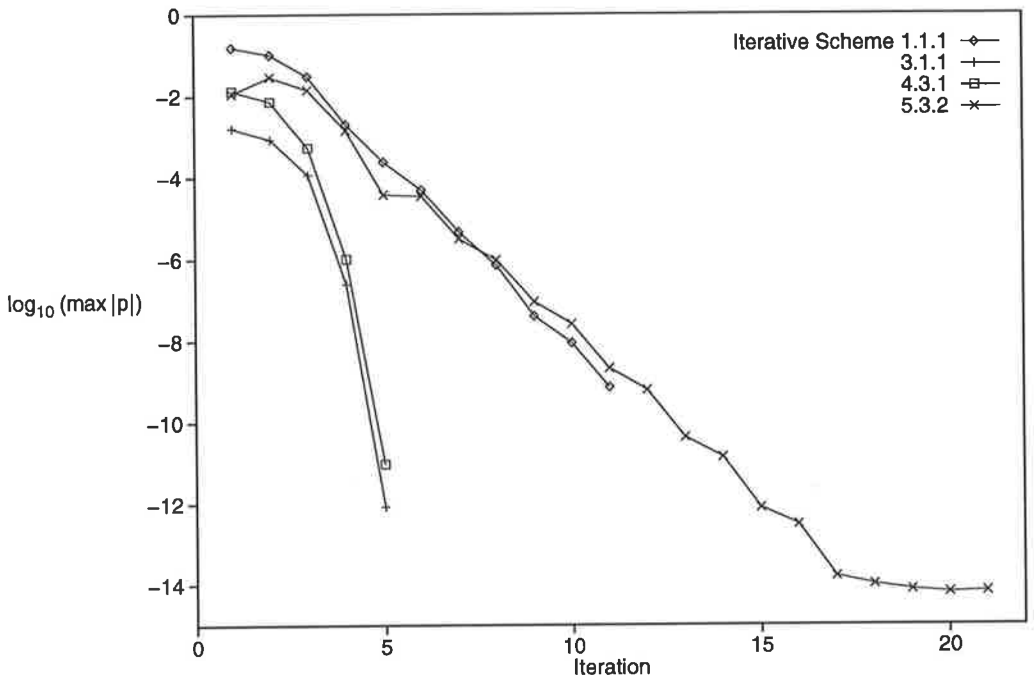

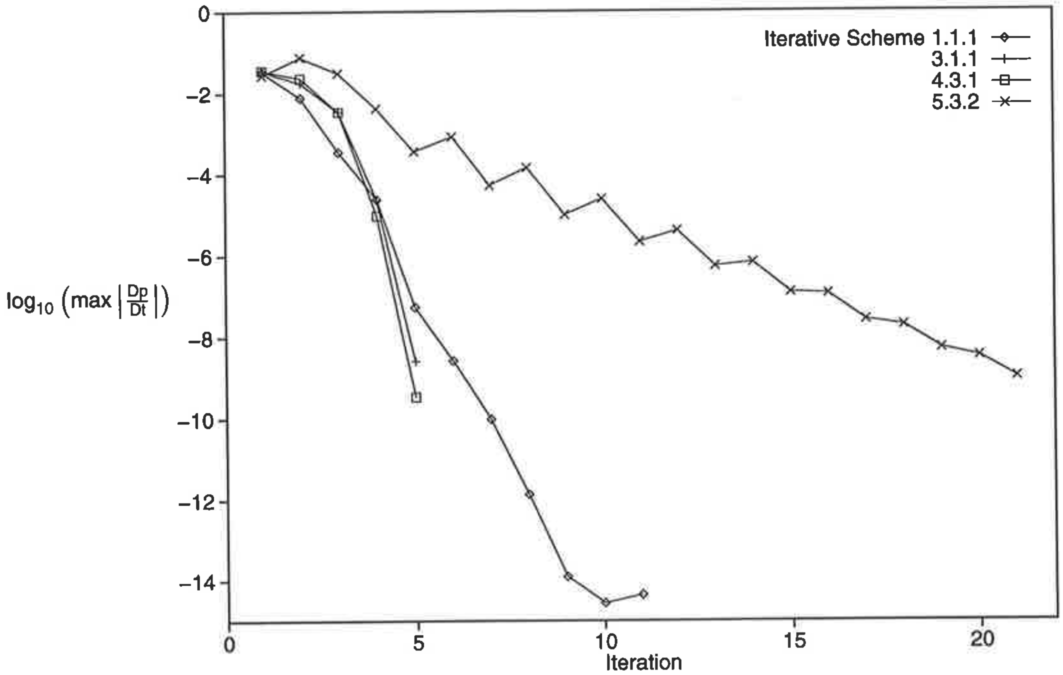

Figure 4.2: Maximum errors (for each iteration) in the free-surface boundary conditions for the various boundary condition formulations.

is a close analogy between some of these terms and the formulation of the surface update procedure 2. Recall that the only cases in the previous section where a converged solution could not be obtained were those that implemented this surface update procedure, which indicates that an instability is introduced by this approach.

Another point of interest is the balance between the magnitudes of the errors for pressure and its material derivative. Boundary condition formulation 1 produces an iterative scheme where the error in pressure is always greater than that for its material derivative. The remaining three formulations are in opposition to this. This observation holds irrespective of the singularity location scheme, and is most likely related to the stage of the iterative process at which these quantities are determined. When using boundary condition formulation 1, it is intended that the boundary condition is enforced, convergence is checked, and then, if failing the convergence test, the free-surface approximation is modified. The boundary condition formulation applies the material derivative of pressure condition, and hence it is reasonable that at the time of checking for convergence, the error should be small in comparison to that for the pressure. Under boundary condition formulations 3 and 4, the potential is determined and the free-surface approximation updated (in a manner that reduces the pressure to near zero) before testing for convergence. Consequently, the surface on which the errors are determined is one for which the pressure is small.

Figure 4.3 shows the effect on the error of shifting the singularities for schemes 4.3.1, 4.3.2 and 4.3.3. Formulation 4.3.1 should be quadratic in convergence since the singularities are not moved, and this is supported by its curve. Schemes 4.3.2 and 4.3.3 show a rate of decay that although initially quadratic, settles down to be linear in nature. This is due to the shifting of the singularities, which destroys the quadratic behaviour. In these cases, an additional two iterations are required to achieve the converged solution. Similar behaviour is seen for boundary condition formulation 3, for which the performance is quadratic if the singularities remain stationary. Again, an additional two iterations are required if the singularities are shifted. For boundary condition 1, which has a linear rate of convergence, the error is increased only slightly for singularity location schemes 2 and 3, and no increase in the number of iterations is required to achieve a converged result.

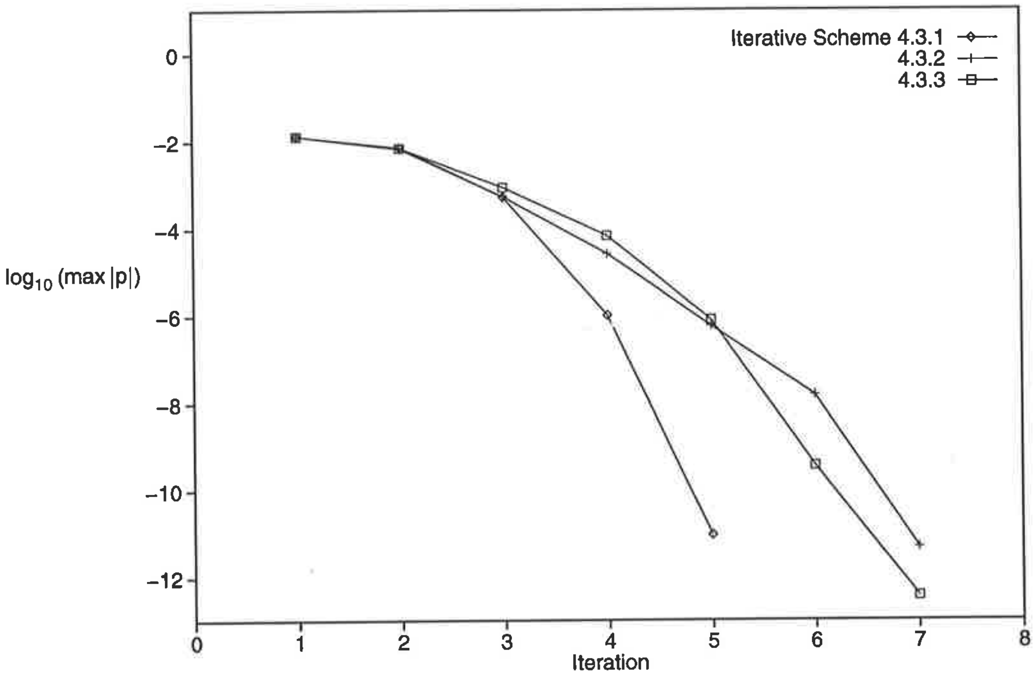

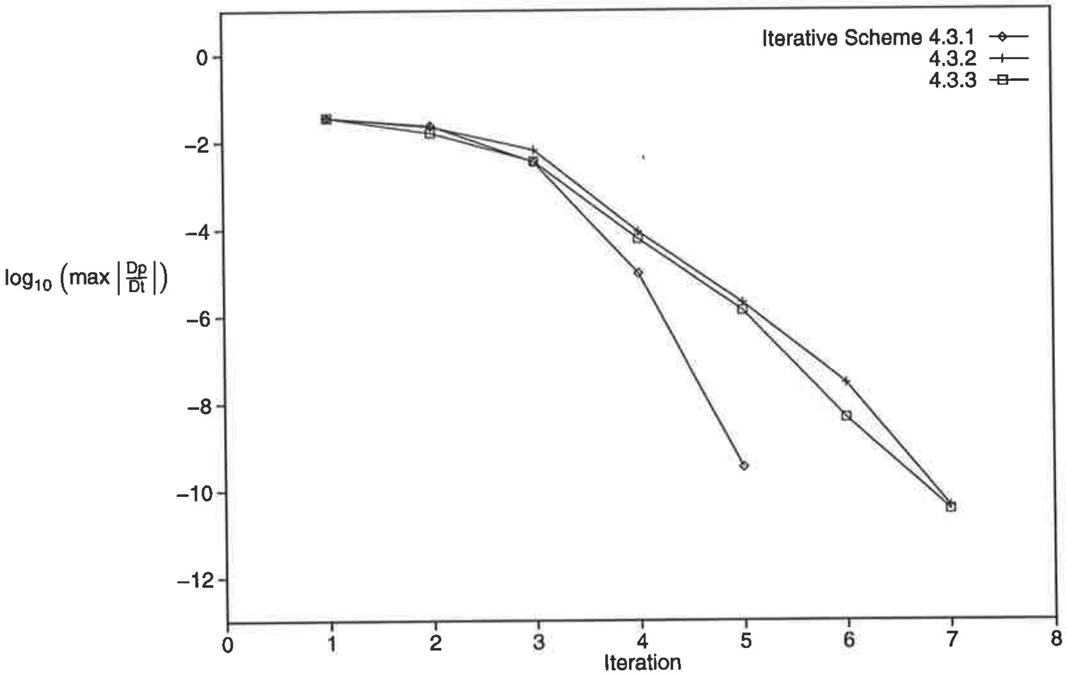

Figure 4.3: The effect of shifting the singularities under location schemes 2 and 3 on the satisfaction of the free-surface boundary conditions, in comparison to stationary singularities. The boundary condition formulation is 4.

Iterative scheme	Short domain	Standard domain	Extended domain
1.1.1	10	11	11
1.1.2	10	11	12
1.1.3	10	11	12
3.1.1	5	5	7
3.1.2	6	7	9
3.1.3	6	7	9
4.3.1	5	5	6
4.3.2	5	7	8
4.3.3	6	7	8
5.3.2	14	21	28

Table 4.3: The number of iterations required to achieve convergence using the shortened, standard and extended domains for each of the iterative schemes.

4.3.3.2 DEPENDENCE UPON FREE-SURFACE AND POTENTIAL REPRESENTATIONS

Several other test cases were also considered. The standard test used the parameters as described in the previous section. In addition to this set of parameters, two tests were run with the domain length doubled and halved. Similarly, tests were run with the resolution doubled and halved. Also, singularity offset heights of 0.3 and 0.9 were considered in addition to the standard 0.6.

The most obvious result of these tests is that the domain length dominates the number of iterations required. The shorter the domain, the fewer iterations required. This is largely due to the nonlinear effect of shortening wavelength as amplitude is increased. As the iterative scheme successively approximates the free surface, the amplitude is modified, and hence also the wavelength. This leads to large changes in free-surface elevation several wavelengths downstream, which consequently require more iterations. Table 4.3 shows the number of iterations required to achieve convergence under each of the iterative schemes using the shortened, standard and extended domains.

Another interesting observation is that converged solutions cannot be obtained using the higher resolution free-surface representation if the singularities are shifted. (The only exception to this is scheme 4.3.3, where a converged result is obtained, but the convergence rate is considerably diminished.) Conversely, if the singularities are held fixed, then convergence is achieved. The conditioning of the system is poorer using the higher resolution, and it is possible that the effect of shifting the singularities is too disruptive and causes the iterative scheme to fail.

For singularity location scheme 2, using the higher offset height of 0.9 results in either considerably degraded performance or else a lack of convergence. Again, this is most probably related to the conditioning of the system. This difference is not observed for singularity location scheme 3. This apparent enigma is likely to be related to the conflicting roles of shifting the singularities with regard to disrupting the iterative procedure, but obtaining a better-conditioned system of equations, and will be dealt with in greater detail in section 4.3.4.

4.3.4 THE ABILITY TO CAPTURE WAVES OF LARGE STEEPNESS

One of the more interesting applications of a free-surface flow determining method is to investigate flows which exhibit strongly nonlinear behaviour. Consequently, it is of interest to investigate the ability of the method to converge to a solution as the moment of the dipole in increased in magnitude.

This section is divided into two parts. In the first, the initial approximation for the free surface is the plane $z = 0$, and the initial approximation to the potential is the uniform stream, $\phi = Ux$. In the second section, the solution from a similar problem is used as the initial guess.

4.3.4.1 CONVERGENCE FROM A UNIFORM-STREAM INITIAL APPROXIMATION

Using the base potential and planar surface as the initial approximations, a brief attempt to determine a solution for a dipole of moment 0.4 was shown to be unsuccessful for each of the iterative schemes. This suggested the possibility of using a bisection method to determine the maximum strength for which a converged solution could be obtained. The interval $[0.2, 0.4]$ is bisected 5 times, in a manner such that a converged solution can be obtained at the lower value of the interval, but not for the higher value. Hence, the end result is an interval of length 0.00625, which contains the maximum dipole moment for

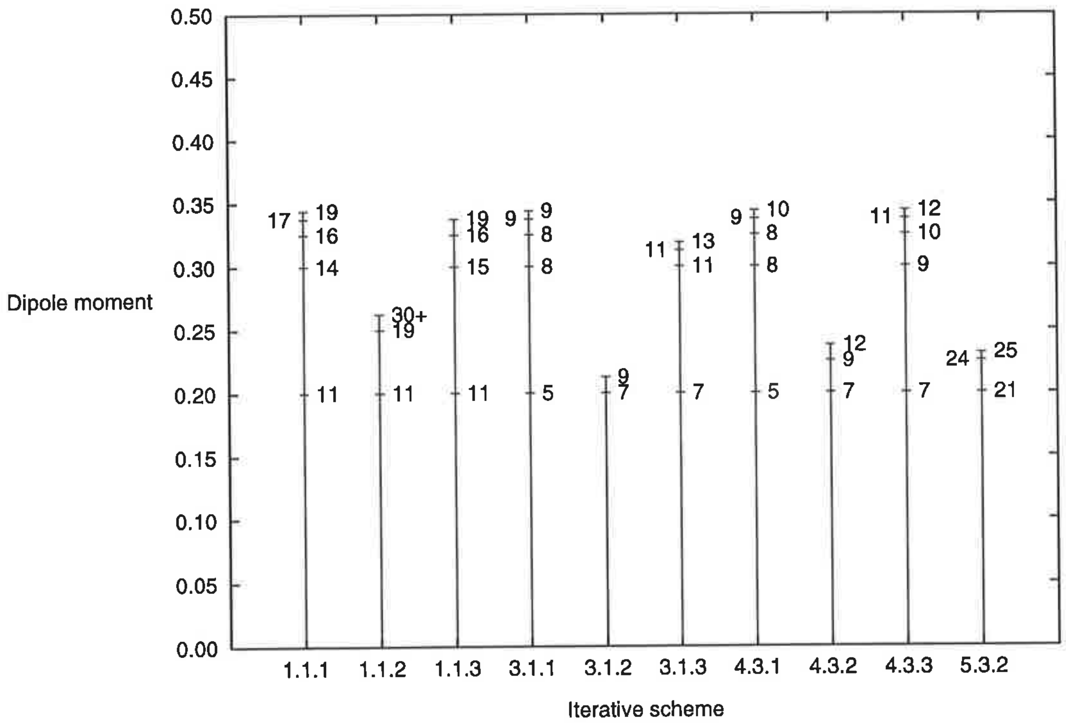

Figure 4.4: The range of dipole moments μ for which a converged solution can be obtained and the number of iterations required to do so, for each of the candidate iterative schemes.

which a solution can be obtained by the given iterative scheme. This interval is expected to be approximately 1–2% of the maximum dipole strength, since at a Froude number of 1 and for small dipole strengths there is an approximate equivalence in magnitudes between the dipole strength and the resulting dimensionless wave amplitude.

Figure 4.4 displays the results of this trial. A vertical line is given for each iterative scheme, the height of which indicates the maximum dipole moment for which a converged solution can be obtained. The points that are superimposed on these lines represent the various other solutions obtained during the bisection process. The number displayed next to each of these points indicates the number of iterations that are required to do so. In the only case (iterative scheme 1.1.2) where the limitation on the number of iterations was enforced, the number of iterations is designated as 30+ to indicate this. Assessment of the errors for this case indicates that convergence would have been achieved if the iterative scheme were allowed to continue.

In general, those iterative schemes that use singularity location schemes 1 and 3 perform well in comparison to those that use singularity location scheme 2. Iterative schemes

1.1.1, 3.1.1, 4.3.1 and 4.3.3 all achieve the solution for $\mu = 0.34375$, with scheme 3.1.1 requiring the least iterations at only 9, and scheme 1.1.1 requiring the most at 19. This figure reinforces the observation that shifting the singularities causes an increase in the number of iterations required by those schemes that would otherwise display a quadratic rate of decrease in error.

The reason for the poor performance of singularity location scheme 2 relative to that of both 1 and 3 is at first unclear. It appears, however, that two conflicting forces are at play. Firstly, there is a tendency to disrupt the iterative procedure when shifting the singularities, and this accounts for the larger number of iterations required by schemes 2 and 3 to achieve convergence, as was shown previously in Figure 4.3. In some instances, this disruption is so great that no converged solution can be obtained, as was noted with the high singularity offset used in Section 4.3.3.2. Secondly, there is a tendency to produce a better-conditioned system of equations, especially when the normally-linked location scheme is used. This results in a more stable iterative procedure, as the effects of modifying the free surface and singularity locations and strength are localised. These two components, one detrimental and the other beneficial are both at play in singularity location schemes 2 and 3. However, it appears that for the vertically-linked scheme, the detrimental component outweighs the beneficial component, and hence the significantly poorer range of dipole moments for which a solution can be obtained.

4.3.4.2 CONVERGENCE FROM A SIMILAR SOLUTION

An alternative method that can be employed when trying to achieve convergence for waves that are steep, is to use a more reasonable starting approximation in an attempt to decrease the likelihood of divergence. For this problem, one might choose to use the solution from a flow that has a slightly smaller dipole moment.

For each iterative procedure, the maximum dipole moment for which a solution can be obtained using the naïve initial approximations of the previous section is used as a starting point for the searching algorithm. Using the converged solution from that case, the flow about a dipole of increased moment is sought. The initial increase is 0.1. If a converged solution is obtained, then the new solution is used as an initial approximation for the next case, which again has a dipole of moment increased by 0.1. If, however, no solution is obtained, then the increment for the dipole moment is halved, and the process

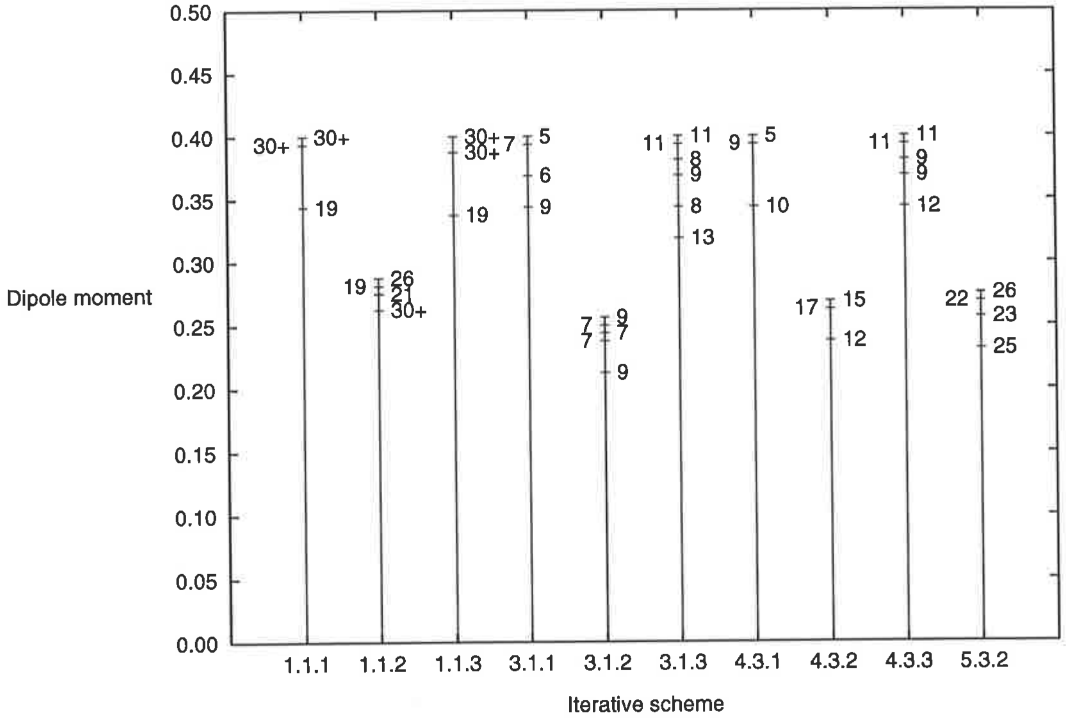

Figure 4.5: The range of dipole moments μ for which a converged solution can be obtained, and the number of iterations required to do so for each of the candidate iterative schemes. In this case, the converged solution from the previous smaller dipole moment is used as the initial approximation.

is repeated. The process of searching for a solution is to be continued until the incremental strength has been halved four times, from 0.1 to 0.00625, at which time the process is to be halted. Figure 4.5 shows the results of using this algorithm.

For each iterative scheme, the smaller value of dipole moment is the maximum that could be achieved in the previous section using the uniform stream as the initial approximation for the surface and potential. Again, the numbers beside the individual points indicate the number of iterations required to achieve convergence, but this time the converged results from the previous case are used as the initial approximation. So, for example, to achieve the converged solution for $\mu = 0.39375$ using scheme 4.3.1, it was first necessary to get the solution at $\mu = 0.34375$ which required 10 iterations, and then to use that solution as an initial approximation and *another* 9 iterations.

Iterative schemes 1.1.1, 1.1.3, 3.1.1, 3.1.3, 4.3.1 and 4.3.3 all achieve solutions for dipoles of moment 0.4, for which the free surface is strongly nonlinear, and the tallest crest has a height of 0.4. All six iterative schemes fail to achieve results at $\mu = 0.40625$, and yet the last four have converged quickly (requiring 5, 11, 5 and 11 iterations respectively) to the solution at $\mu = 0.4$. These observations cast doubt on the *existence* of a solution for a dipole of moment greater than 0.40625.

By comparison, schemes 1.1.2, 3.1.2 and 4.3.2 are poor, all failing to converge to a solution for dipoles of moment greater than 0.3. The reasons for the poor performance of singularity location scheme 2 were discussed in the previous section.

Scheme 5.3.2 also performs poorly due to the destabilising nature that is inherent in its formulation.

As an aside, it is worthwhile to mention that a third test was completed, which used the solution free surface and singularity strengths from a previous case as the initial approximations, but *not* the singularity locations. Under this rather odd and inconsistent scheme, results can be obtained for iterative schemes 3.1.2 and 4.3.2 for dipoles of moment up to $\mu = 0.4$, but again no higher. It is surprising that this is more stable for singularity location scheme 2 than is the above, but it is an interesting observation which may prove to be useful.

Another possible variation that may be useful is to reduce the change made in the first few iterations under the quadratically converging schemes. Divergence usually occurs in these first iterations, before the approximation is close enough to start on its quadratic reduction in error. The likelihood of divergence can be reduced if the amount by which the free surface, singularities and their strengths are modified, is reduced. Although not investigated here, the author has found this to be an important tool in the quest for strongly nonlinear waves.

Figure 4.6 displays the free-surface for the horizontal dipole of moment 0.4 as determined by iterative scheme 3.1.1. Note the strongly nonlinear characteristics which include the sharpened crests, flattened troughs and decreased wavelength. The free surface displays a wavelength of 5.596, which is only 89% of the linear theory wavelength of 2π. The maximum height is 0.401 (80% of stagnation height) and the minimum is -0.267, which yield a steepness of 0.119. For comparison, the theoretical maximum wave steepness for a Stokes wave is approximately 0.14 (Wehausen and Laitone [42]). The points of inflection on either side of the crests are approximately a distance of 1.047 apart, which is a third of that expected for a small amplitude wave. At these points the surface has a slope of

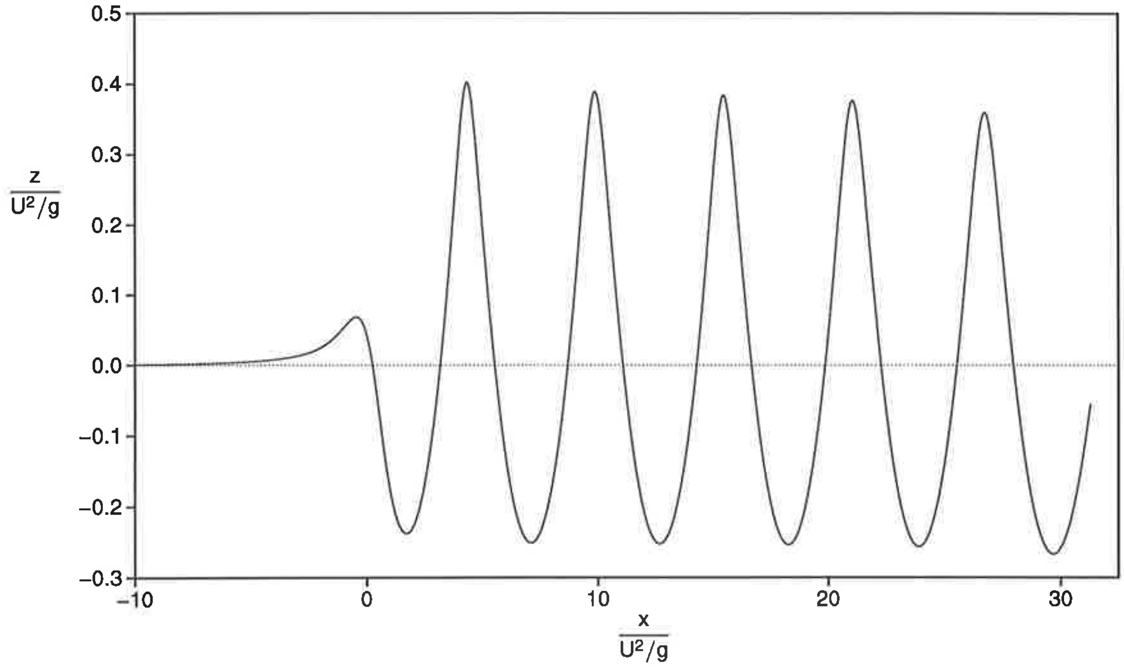

Figure 4.6: Free surface as produced by iterative scheme 3.1.1 for a dipole of moment 0.4.

22.6°, which is 75% of the maximum (30°) which can be expected for a wave that reaches stagnation height.

4.4 CONCLUSION

The four components of an iterative scheme are the boundary condition that is to be enforced on the approximate free surface, the surface update procedure used to determine the next approximation, the singularity location scheme used to shift the singularities between iterations, and the criteria by which convergence is assessed. In this section, five boundary condition formulations, three surface update procedures and three singularity location schemes have been combined in a total of 16 iterative schemes, and their properties relating to speed and reliability of convergence have been tested.

The surface update procedure 2, which is based upon the material derivative of pressure, is found to be unstable, and as such cannot be used. A direct consequence of this is that the boundary condition formulation 2, based upon the pressure, also cannot be used, since any iterative scheme that uses this formulation also requires surface update procedure 2.

Boundary condition 5, which is based upon the simultaneous satisfaction of both free-surface boundary conditions, and incorporates terms associated with the effects of shifting singularities under singularity location scheme 2, is found to be weakly unstable, having a poor rate of convergence and a limited range of values of wave steepness for which a solution can be obtained.

Boundary condition formulations 1, 3 and 4 (based respectively upon the material derivative of pressure, a combination of the two free-surface conditions, and the two free-surface conditions simultaneously) are found to be reliable in application, each having a similar range of wave steepness values for which a solution can be obtained. Formulation 1 has a linear rate of exponential decay in error, whereas both 3 and 4 display a superior quadratic rate. However, boundary condition formulation 4 requires the solution of a larger system of equations, and as such is computationally expensive by comparison. Consequently, boundary condition formulation 3 is the formulation of choice. Its implementation in an iterative scheme requires the use of surface update procedure 1, which is based upon pressure.

Singularity location scheme 1 (which doesn't actually shift the singularities) is stable and efficient, yielding converged solutions for a large range of wave steepness in the minimum number of iterations, but as was shown in Chapter 2, may suffer from inaccuracy in the final potential representation. Singularity location scheme 2 (which shifts the singularities in a vertically-linked manner) is disruptive to the iterative procedure, resulting in a greater number of iterations required, and a smaller range of values of steepness for which convergence can be achieved. By comparison, singularity location scheme 3 (which shifts the singularities in a normally-linked manner) performs well, due to the improvement in condition of the system of equations that results. This scheme is likely to produce solutions with the most accurate potential.

The overall conclusion is that iterative scheme 3.1.1 is preferred, due to the speed at which it is able to converge to results over a large range of wave steepness values. For very large amplitude waves, for which the resulting potential may be inaccurate, iterative scheme 3.1.3 may be best.

PART II

APPLICATIONS FOR SUBMERGED BODIES

SUBMERGED CIRCULAR CYLINDERS

The circular cylinder with and without circulation is discussed for ranges of radii and depths of submergence. For cases without circulation, emphasis is placed on flows with large amplitude waves. For cases with circulation, those flows for which the amplitude of downstream waves is reduced are investigated.

Two identical circular cylinders are then submerged to the same depth and in tandem. There are combinations of separation distances between the cylinders and depths of submergence such that one or both of the cylinders is free of horizontal force. The parameter range for this phenomenon is explored.

5.1 THE SUBMERGED CIRCULAR CYLINDER

The submerged circular cylinder in a steady stream of infinite depth without circulation is a very old problem. Early solutions were for deeply submerged bodies, or more specifically, for small ratios of cylinder radius to submergence depth. In the limiting case, the flow near the cylinder is unaffected by the free surface, and hence can be represented by a Rankine dipole of known strength, placed at the centre of the circle, in a uniform stream of fluid which is of apparently unlimited extent in all directions. On the other hand, in the neighbourhood of the free surface, the leading-order flow is that for the same dipole,

---

The content of this chapter has been discussed previously by the author and his supervisor in two published papers, the first being Scullen and Tuck [36], and the second being Tuck and Scullen [38].

but now it is submerged beneath a Kelvin free surface linearised for small departures from the undisturbed plane surface, for which the solution is well-known (Wehausen and Laitone [42]).

Havelock [14] attempted to find second-order corrections to this linearised result by modifying the dipole singularity structure in order to more accurately satisfy the boundary condition on the cylinder. However, this does not provide a consistent second-order theory, since it is also necessary to simultaneously correct for nonlinear free-surface effects. This was done by Tuck [37].

The solution method as developed in Part 1 is applied to the circular cylinder. For sufficiently small radius-to-depth ratios, the linearised theory is confirmed, as is the second-order theory of Tuck [37]. In fact, the latter theory seems to be quite accurate up to close to the limiting configurations beyond which no solutions can be found.

At any fixed radius-to-depth ratio, the wave amplitude (and hence wave resistance) possesses a maximum as a function of Froude number based on submergence. When that maximum is sufficiently low, linearisation is justified, and converged results in agreement with the consistent second-order theory are obtained for all Froude numbers. However, as the radius-to-depth ratio is increased, that maximum wave amplitude increases until nonlinear effects are very strong, and eventually the largest crest (nearest to the cylinder) in the generated wave is nearing stagnation height. This happens at about a radius-to-depth ratio of 0.2, when there is a small range of Froude numbers around 0.7 where the iterative scheme fails to converge, and where it is believed there may not be a steady potential solution. For larger radius-to-depth ratios, the range of Froude numbers for which solutions cannot be obtained widens.

5.1.1 WAVE RESISTANCE AND THE LINEAR THEORIES

As an initial exercise, verification of consistency of the method with existing approximate theories is sought. Tuck [37] investigated the wave resistance of a submerged circular cylinder by a consistent second-order expansion in the small parameter a/f, where a is the radius of the cylinder and f is the depth of its centre beneath the undisturbed free surface, and compared the results to the first-order theory. For comparison with these approximations, results are produced for a variety of a/f ratios and Froude numbers F

based on submergence depth f.

The representations of the free surface and body are as follows. The computational domain is the x-interval $[-30, 30]$, with 301 sources distributed along the plane $z = 0.8$ at equal intervals of 0.2. The 299 free-surface collocation points are located directly beneath each of the source points (with the exception of the two most outlying sources) and initially along the x-axis. The cylindrical body is centred about the point $(0, -f)$ and is represented by 128 collocation points, on equally distributed rays. Sources are also located within the cylinder on each of these rays, at a radius of $0.85\,a$. The free stream velocity U and gravity g are kept constant at 1, with the Froude number F being varied by its dependence on f. In effect then, there are approximately 30 collocation points per wavelength. The results of Chapters 2 and 3 indicate that these choices are acceptable, and the limiting factor for accuracy is the length of the domain being represented.

The location of nodes and singularities in representing the body was investigated in a manner similar to that in which the wave-like body of Chapter 2 was investigated, using the residual velocities along the known body as a measure of the accuracy that can be obtained. It was found that the maximum error in the Neumann boundary condition on the body using the representation described above was significantly less than that which can be expected for the free surface.

Figure 5.1 shows the results of these computations in graphical form. The vertical axis is given in terms of the dimensionless quantity

$$\overline{R} = \frac{R}{\pi \rho g a^2 \left(a/f\right)^2} \,, \tag{5.1}$$

where R represents the wave resistance. With the wave resistance expressed in this form, the first-order linear theory consists of a single curve versus Froude number. Specifically, it is the graph of

$$\overline{R} = 4\pi F^{-4} e^{-2F^{-2}} \tag{5.2}$$

and is independent of the radius-to-depth ratio, but is valid only when that ratio is small. The consistent second-order approximation requires a different curve for each radius-to-depth ratio, the difference between each such curve and the first-order linear theory being proportional to the square of a/f at fixed F.

As can be seen from the figure, the results are in close agreement with the linear theory for sufficiently small radius-to-depth ratio. In fact the results are graphically indistinguish-

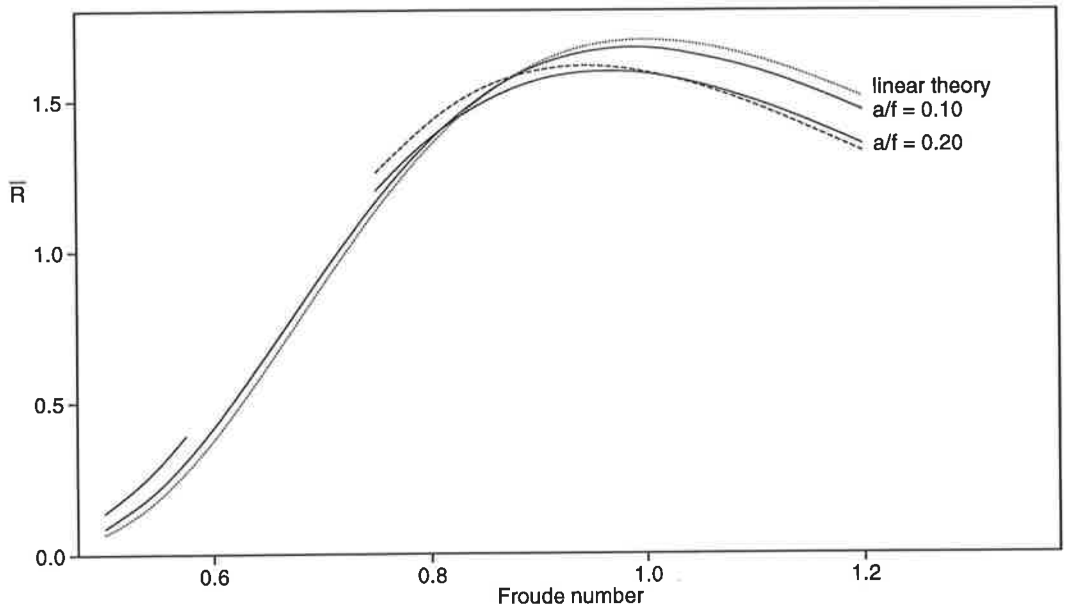

Figure 5.1: Scaled wave resistance for submerged circular cylinders. The solid lines are the results for $a/f = 0.1$ and $a/f = 0.2$. The dotted curve is the first-order linear theory (independent of a/f), and the dashed curve is the second-order linear theory for $a/f = 0.2$.

able from the second-order theory for $a/f = 0.1$, and the departure from the first-order theory still shows good correlation with the second-order theory for larger cylinders over the range of Froude numbers investigated. However, for sufficiently large disturbances, including $a/f = 0.2$, the procedure fails to converge for some Froude numbers near 0.7, and a break in the curve for $a/f = 0.2$ has been made to indicate this. Even for $a/f = 0.2$ though, there is still reasonable agreement with the second-order theory for those Froude numbers at which results can be produced, with the strongest disagreement being for the smaller Froude numbers near 0.5.

The Froude number $F = 0.7$ is significant since, in the first-order linear theory, it is at the value $F = 1/\sqrt{2} \approx 0.7$ that the wave resistance is a maximum (for fixed U, g and a/f). Consequently, this is the Froude number that gives the steepest waves, and therefore the region in which wave breaking occurs first. (This maximum in the actual resistance is obscured by the use of $a^2(a/f)^2$ rather than $(a/f)^4$ in the denominator of equation (5.1), the effect of which is to shift the maximum in the scaled resistance to the Froude number 1.0, as is observed in the figure.)

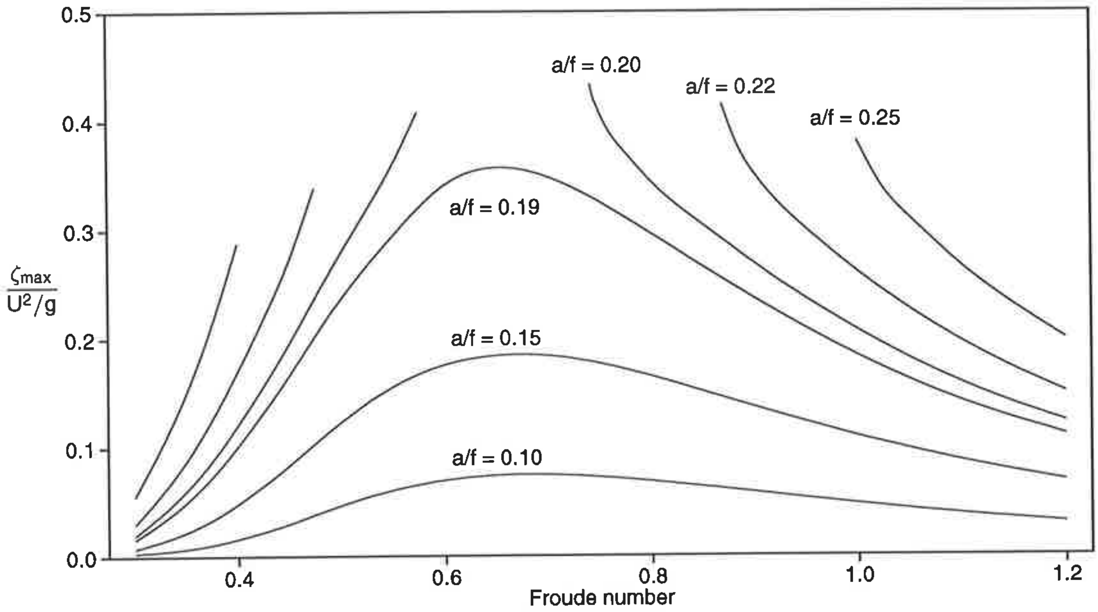

Figure 5.2: Scaled height of the highest point on the free surface. 0.5 represents a possibly unobtainable upper-bound.

5.1.2 SOLUTIONS WITH LARGE AMPLITUDE WAVES

For large enough disturbances, one can expect that the physical solution to the problem will produce a breaking wave. One can justifiably question if such cases can be modelled by a potential flow method, or indeed any steady method. As the non-linearity of the disturbance increases, it is more difficult to obtain a solution, and whether this is due to the non-existence of a steady potential solution or else due to some other complication such as a numerical artefact is not always clear.

Figure 5.2 is a plot of the highest point of the free surface, which is usually the height of the first crest, for various values of a/f and Froude number. All of the results have been scaled with respect to the length U^2/g, so that the highest possible free-surface point, which has the stagnation height $U^2/(2g)$, scales to 0.5. It is important to note that there may not exist a steady potential solution for which the crest actually reaches the stagnation height. Therefore, 0.5 is an upperbound for the quantity plotted in the figure.

For small cylinders, with $a/f = 0.10$, 0.15 and 0.19, there are always steady-state solutions, throughout the entire range of Froude numbers. However, for the larger cylinders with $a/f = 0.20$, 0.22 and 0.25, it is clear that the wave height is increasing rapidly near some particular Froude numbers, and there is a range of Froude numbers about 0.7 for which the method does not produce any solution. In particular, the fact that the curves are approaching the upperbound height of 0.5 at the edges of this range, suggests that steady potential solutions may not exist. On this basis it is estimated that for $a/f = 0.22$, solutions may not exist for Froude numbers between 0.50 and 0.85. For the even larger cylinder with $a/f = 0.25$, the range of Froude numbers could possibly be as wide as from 0.45 to 0.95.

Another point to note is that it is difficult to compute waves with a maximum scaled height greater than about 0.430, which corresponds to a (far-downstream) wave steepness of approximately 0.114. In fact, to produce results with a maximum scaled height larger than approximately 0.375 requires care and considerable computational effort, whereas for smaller waves the results can be produced to within relative tolerances of 10^{-8} in just 6 or 7 iterations.

As mentioned previously, one of the main causes of divergence in the iterative procedure is due to the non-linear effect of wavelength reduction, as the early approximations in the iteration scheme have crests where the final converged solution has troughs. The required correction is then larger, and this can lead to divergence. It should be noted that this change in wavelength is a "sub-harmonic perturbation" (Longuet-Higgins [26]) whose effect on pure Stokes waves is (weakly) unstable even for small waves, but strongly unstable for waves of steepness greater than about 0.13. As a consequence, one should not expect to be able to compute very steep waves by the present method without fixing the wavelength, as was done for the Stokes-wave computations of Scullen and Tuck [36].

Relaxing the amount by which the potential is perturbed at each iteration can often delay this instability sufficiently for the iterations to settle down with the correct wavelength, although the quadratic rate of convergence of the process is then destroyed. Also, all of the results given here take the undisturbed plane free surface and uniform-stream potential as their initial approximations. For significantly non-linear cases, using a closer approximation to the final free surface and potential (as in Section 4.3.4.2) could reduce the number of iterations required, and increase the likelihood of obtaining a converged solution for some of the more nonlinear cases.

For very steep waves, the resolution near the peaks is poor. This could be improved by decreasing the distance between neighbouring points, and may require the shifting of sources away from the plane above the wave to a shape that more closely follows the wave. The preference would be to use a normally-linked singularity location scheme, as

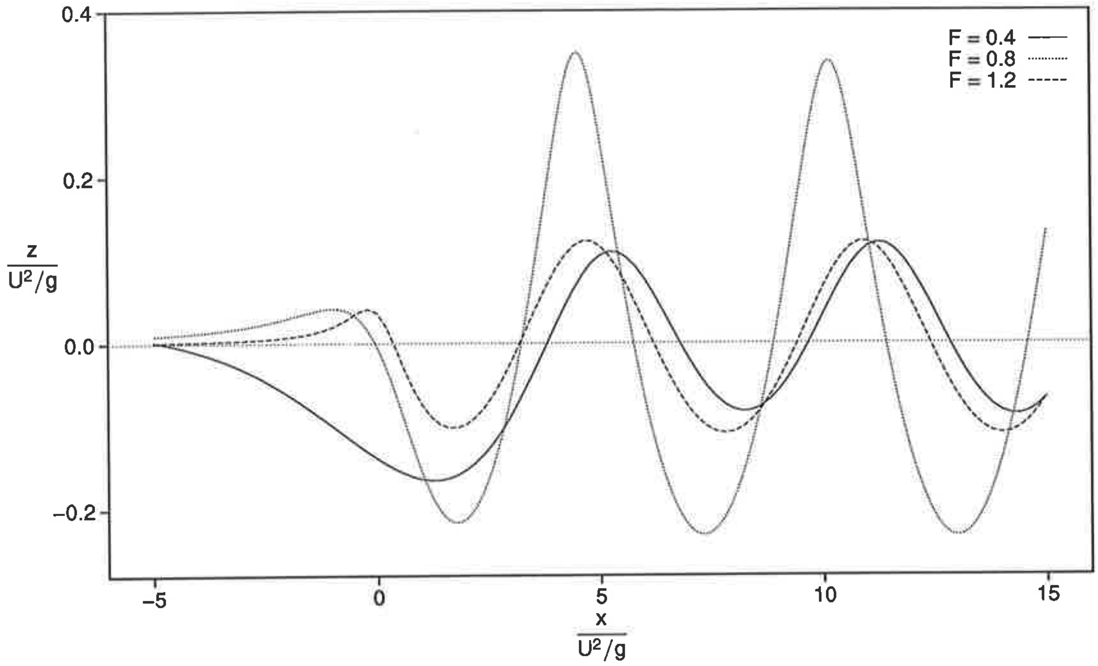

Figure 5.3: Examples of waves produced by the cylinder for which $a/f = 0.2$ at Froude numbers 0.4, 0.8 and 1.2.

discussed previously in Section 4.2.3.

Figure 5.3 shows examples of the free-surface shape computed at $a/f = 0.2$, for low (0.4), medium (0.8), and high (1.2) values of the Froude number. Note that the steepest waves are at the medium Froude number (which is closest to $1/\sqrt{2}$), and that these are significantly non-sinusoidal. Note also how the predominant local free-surface displacement ahead of the cylinder is a (strong) depression at low Froude numbers but this changes to a (weak) elevation at high Froude numbers.

As a final point, Figure 5.1 suggests that wave resistance may not be greatly affected for cases in which a converged solution cannot be obtained. The wave resistance may not vary dramatically from that which could be expected from interpolation of these curves, at least for those cases in which solutions have been determined except in a narrow band of Froude numbers.

5.2 CIRCULAR CYLINDERS WITH CIRCULATION

Circulation is particularly interesting in this problem since (Tuck and Tulin [39]) it is apparently capable of cancelling the trailing wave pattern. In fact, in the first-order linearised theory (Wehausen and Laitone [42]), the trailing wave amplitude is a linear function of the circulation, vanishing at an anticlockwise value of circulation that generates a negative lift of exactly twice the buoyancy of the circular cylinder. The motivation of the present study is to examine the extent to which nonlinear effects alter this conclusion.

5.2.1 THE LINEAR THEORY

As mentioned above, Tuck and Tulin [39] observed that the linear theory suggested that there exists a circulation about the submerged cylinder for which waves are not produced downstream, and hence the body feels zero wave resistance. They found that linear waves are totally eliminated for a particular circulation $2\pi\kappa_0$ such that

$$\kappa_0 = a^2 g/U \, . \tag{5.3}$$

They also noted that for this circulation a force acting downwards of magnitude equal to twice the buoyancy is produced. Therefore, no unsupported body can produce such a circulation.

The linear theory also indicates that as circulation, κ, is increased from zero to the critical value κ_0, the amplitude of the waves produced by the disturbance decreases linearly and becomes zero. If the circulation is increased further still, waves reappear and grow in amplitude but they have the opposite phase to those for which $\kappa < \kappa_0$. Crests now appear where there used to be troughs, and vice-versa. All of this occurs without any change in wavelength according to the linear theory, and the only change in phase is a change of π as the circulation passes through the critical value.

Results for a variety of combinations of submergence depths and circulations have been produced using the current method. For cylinders of sufficiently small radius-to-depth ratio, the results are in agreement with the linear theory, and the phenomena mentioned above are observed. Figure 5.4 shows the results for the very small cylinder $a/f = 0.02$. A local hump is produced on the free surface above the cylinder, which grows in amplitude as the circulation is increased. Although this hump can be large in magnitude compared to the amplitude of the downstream waves, it is of a symmetric form, with the waves superimposed upon it. As a result, the submerged cylinder feels no drag due to this hump, the only source of drag being due to the energy imparted to the downstream waves. The local hump does however introduce a down-force proportional to the circulation.

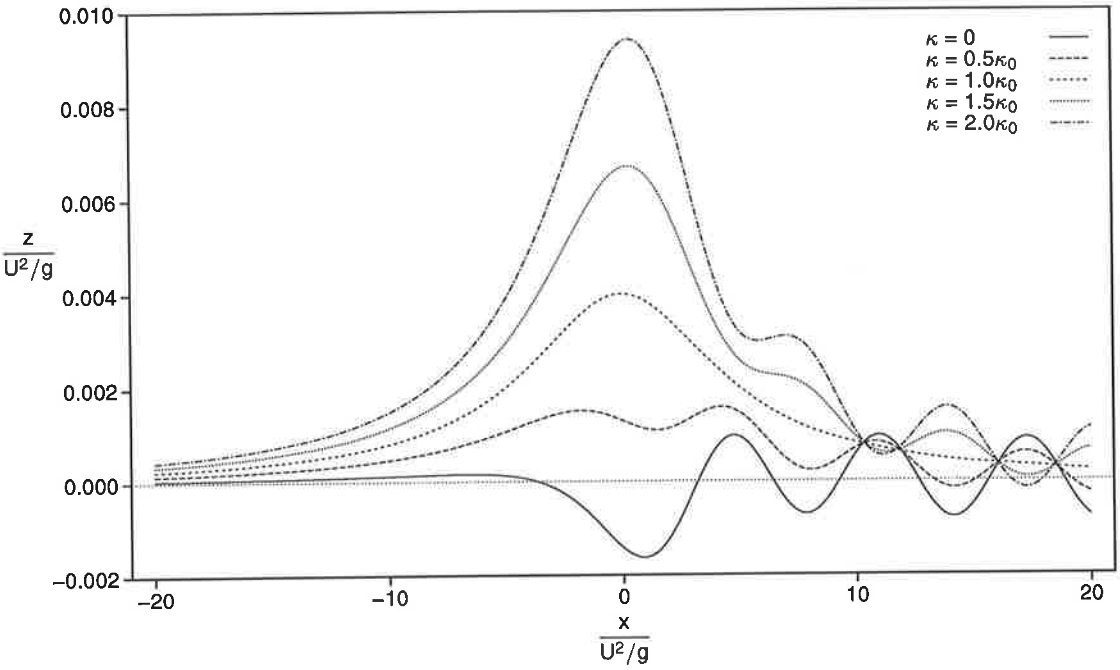

Figure 5.4: Almost linear waves produced by cylinders with $a/f = 0.02$ for differing circulations at Froude number 0.4472.

5.2.2 WAVES PRODUCED BY LARGE CYLINDERS

Some interesting results are found for cases in which nonlinear effects become apparent. In some cases, notably for relatively high Froude numbers, the wave amplitude (and hence wave resistance) is dramatically reduced over a range of circulations from considerably less than $2\pi\kappa_0$ to considerably more. In other cases (for lower F values), waves cannot be made to reappear at all when κ is increased above κ_0. Figure 5.5 gives such results for $a/f = 0.1333$ and $F = 0.3651$. If the circulation is increased still further, the local hump grows in amplitude until it is so large that converged solutions cannot be produced, even though the far-downstream waves are quite small. This typically happens when the height of the local hump is 80–90% of the stagnation height. Again, it is unclear that a solution actually exists in the cases where one cannot be obtained by the present method.

5.2.3 WAVE RESISTANCE AND LIFT FORCES

Of special interest are the results for $\kappa = \kappa_0/2$, as in this case the first-order linear theory implies that the net lift on a massless body is close to zero. The down-force due to the circulation exactly cancels the buoyancy in that theory, and the only remaining effect is due to the free surface. The theory also suggests that the wave resistance at

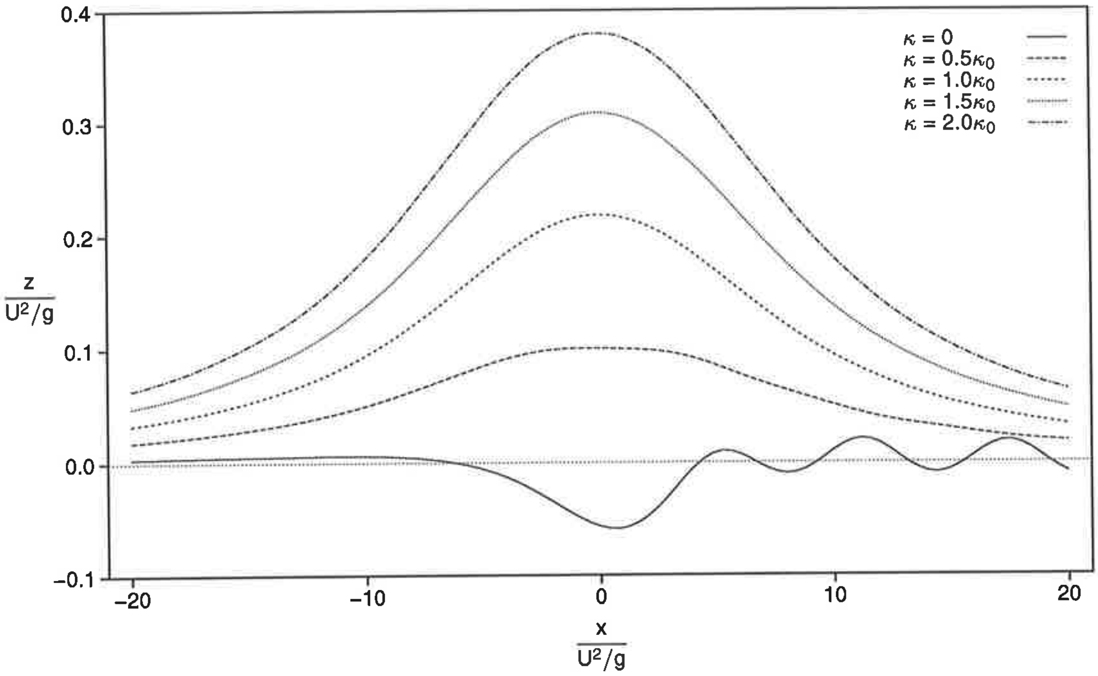

Figure 5.5: Waves produced by cylinders with $a/f = 0.1333$ at $F = 0.3651$ for differing circulations.

this circulation is one quarter of the wave resistance for the case without circulation. Thus it is possible to have an unsupported cylinder which experiences a much lower wave resistance than it would without circulation. The nonlinear computations show that for larger cylinders, and for Froude numbers near 0.5, the reduction in wave resistance can be substantially greater. Figure 5.6 shows the wave resistance for varying Froude number at a circulation of $\pi\kappa_0$ for the same a/f values as in Figure 5.1 for which the circulation is zero. It also has an additional curve corresponding to the even larger cylinder $a/f = 0.25$, for which converged solutions with circulation can be obtained throughout the range of Froude numbers, whereas with zero circulation, converged solutions do not always exist. The solid curves are the nonlinear results at $a/f = 0.1$, 0.2, and 0.25. The dotted curve is the first-order linear theory. Note that large cylinders at low Froude numbers have substantially lower wave resistance than is predicted by the linear theory.

The wave resistance at the critical choice $\kappa = \kappa_0$ can be computed, but its magnitude is so small that the results are not significant. If the circulation is increased even further to $\kappa = 3\kappa_0/2$, the linear theory predicts a wave resistance identical to that for $\kappa = \kappa_0/2$. Figure 5.7 shows this result in comparison to the nonlinear computations for various a/f values. The nonlinear results seem to imply a much lower wave resistance than that for $\kappa = \kappa_0/2$, especially at low Froude numbers.

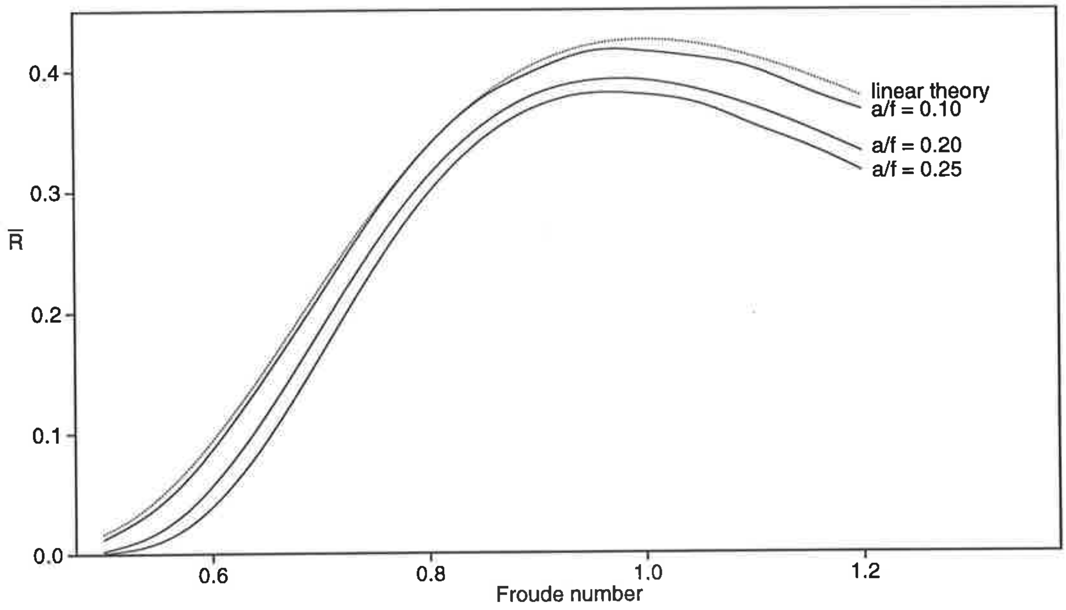

Figure 5.6: Dimensionless wave resistance for submerged circular cylinders with circulation given by $\kappa = \kappa_0/2$. Solid curves are the nonlinear results at a/f = 0.1, 0.2, and 0.25. The dotted curve is the first-order linear theory.

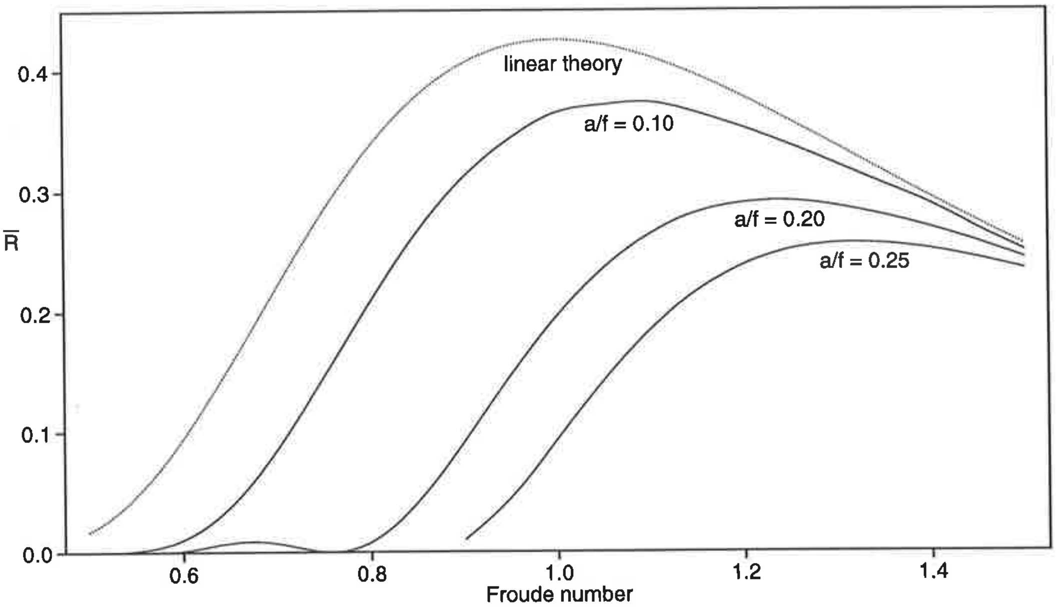

Figure 5.7: Dimensionless wave resistance for circular cylinders with circulation given by $\kappa = 3\kappa_0/2$. The solid curves represent nonlinear results at a/f = 0.1, 0.2, and 0.25. The dotted curve is the first-order linear theory.

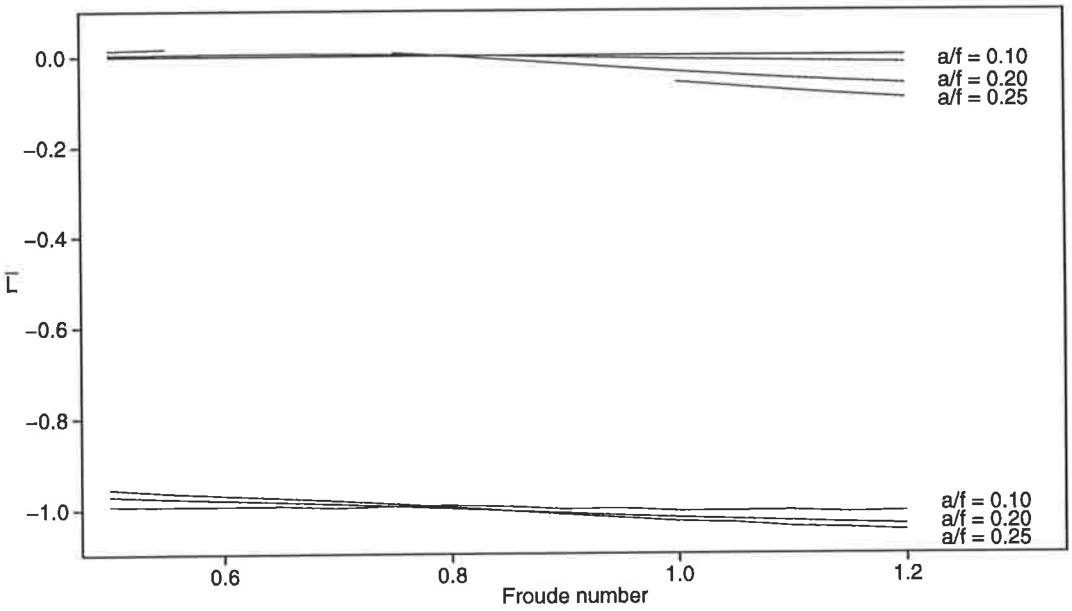

Figure 5.8: Dimensionless lift for submerged circular cylinders with $a/f = 0.1$, 0.2,and 0.25, both without circulation and with circulation given by $\kappa = \kappa_0/2$.

With the lift expressed in terms of the dimensionless quantity

$$\overline{L} = \frac{L}{\pi \rho g a^2} \tag{5.4}$$

where the denominator is the buoyancy of the cylinder, linear theory predicts

$$\overline{L} = -a^2 \left[0.5h^{-3} + h^{-2} + 2h^{-1} - 2e^{-2h} \Re \operatorname{Ei}^-(2h)\right] - 2\kappa/\kappa_0 \, . \tag{5.5}$$

The terms not involving κ are as in Tuck [37], but in general if $\kappa \neq 0$ these terms are dominated by the last term involving the circulation. Hence, $\overline{L}$ is close to zero in the absence of circulation, and close to -1 for $\kappa = \kappa_0/2$.

Figure 5.8 displays the lift computed for the cases $a/f = 0.1$, 0.2, and 0.25, for both of these values of circulation. Again, the results are consistent with the linear theory for the sufficiently small cylinder $a/f = 0.1$ and show the expected small variation for the more nonlinear cases.

5.2.4 SUMMARY OF OBSERVATIONS

When anticlockwise circulation is included, the downstream waves may be reduced in amplitude, although the local disturbance is increased. The local free surface takes the shape of a large and wide hump with the downstream waves superimposed on it. This hump does not in itself affect the wave resistance, but it does produce a down-force on the submerged body. The wave resistance will, however, be reduced if the circulation results in downstream waves of smaller amplitude. In some circumstances, this reduction can be substantial, and some interesting results are found.

There are (as linear theory predicts) values of circulation for which waves are eliminated and the wave resistance is zero. However, linear theory suggests that for any particular combination of radius, free-stream speed and gravitational acceleration, that value of circulation is unique, and for other circulations the wave amplitude is directly proportional to the difference in circulation from this unique value. Non-linear effects modify this conclusion to the extent that there may exist a range of circulations for which the resulting waves have an amplitude that is diminished significantly beyond that which would have been expected. This range may incorporate circulations for which an unsupported body need not be thrust downwards.

5.3 TANDEM SUBMERGED CYLINDERS

If two bodies are placed in a stream U in tandem, there are grounds for anticipating a repulsive force of interaction between them. For example, if a single body is placed in a stream, it would have stagnation zones ahead of and behind it, and hence a pressure gradient in the stream-wise direction. If one then places another body in either zone, one would expect this pressure gradient to push the two bodies apart. It is this force that helps dolphins to coast in the bow wave of fast-moving ships. This property has nothing to do with wave generation, gravity, or the presence of a free surface (Newman [28]).

However, wave generation makes it possible for there to be a force of attraction between two bodies in tandem near a free surface, since the trailing body may utilise some of the energy inherent in the waves produced by the leading body. This is essentially a gravity-wave phenomenon.

For submerged bodies, each of these two distinct and opposite phenomena plays a rôle, and it is possible for each body to experience either a thrust or a drag. For the leading body, the brief discussion above shows that when deeply submerged (and therefore creating waves of low energy), the body experiences a thrust, whereas if shallowly submerged, the wave resistance may in fact create a net drag. For the trailing body there is a drag when deeply submerged, but when shallowly submerged the horizontal force depends upon the amplitudes of the waves created by each body, and the phase relationship between them. The only restriction is that the combination must have a non-negative drag, since otherwise an input of energy from some source other than the stream is required. One consequence of this is that both bodies cannot simultaneously experience a thrust in the upstream direction.

It is therefore possible for either body to experience zero horizontal force. To achieve this for the leading body, it is only necessary to adjust the depth of submergence so that the wave drag, which is very strongly dependent on depth, is equal and opposite to the local thrust, which is essentially the same for all depths. This is, in principle, possible for any reasonably shaped pair of bodies at any (not too small) separation distance, though most easily realisable for similar or identical bodies. It holds both in two and three dimensions; for example, Xu [44] has shown that the leader of two tandem spheres can have zero (or negative) drag in some circumstances.

In two-dimensional flow, if one combines two linear wave-makers with closely similar properties, it is possible to use destructive interference between phase-shifted separate wave patterns to cancel totally the combined far-downstream waves. For example, this can be done by a combination of thickness and lifting effects for submerged airfoil-like bodies (Tuck and Tulin [39]), and as in the previous section, for a single circular cylinder with appropriately chosen circulation. Even more familiar examples occur for single bodies or pressure distributions of finite extent (Lamb [25, page 404], Tuck and Vanden-Broeck [40]), or finite-length bumps on the bottom of water of finite depth (Forbes [10]), where cancellation occurs essentially via destructive interference between out-of-phase bow and stern-generated waves.

For cases of two separate identical bodies submerged to the same depth in tandem, such cancellation can occur for appropriate separation distances. In such cases, there will be zero net drag on the combination. This is known to be an exact result in the linear theory. According to linear water-wave theory with small-amplitude sinusoidal waves of wavelength $2\pi U^2/g$ (Newman [29, page 270]), exact wave cancellation occurs when the separation ℓ between identical wave-making bodies is an odd multiple of a half-wavelength, namely $\ell = (2n+1)\pi U^2/g$, for $n = 0, 1, 2, \ldots$. The linear theory is valid for bodies that are sufficiently small or sufficiently deeply submerged. Otherwise the waves made are nonlinear and non-sinusoidal, and there is no guarantee that exact and complete cancellation can be expected, nor any prior information about the discrete separations at which such cancellations might occur. Schwartz [33] and Forbes [10] did however give strong numerical evidence for the exact cancellation of nonlinear waves made by pressure distributions and bottom bumps respectively, and it is possible that a similar situation may occur for tandem submerged cylinders.

It is possible, by simultaneous adjustment of both distances, to achieve a situation where each body is subject to zero horizontal force. From the linear theory, one can expect a discrete set of such configurations, parameterised by an integer n as above. Given the shape and size of the identical bodies, for each $n = 0, 1, 2, \ldots$ there will be a unique depth f and a unique separation ℓ for zero horizontal force. Hence the depth-to-separation ratio f/ℓ of the configuration is uniquely determined for each n. The $n = 0$ configuration has the smallest separation (being a half-wavelength), and hence the largest local repulsive force. Therefore it needs the largest wave for cancellation purposes, and so has the least depth of submergence.

As a specific example, the following specialises to a pair of identical submerged circular cylinders of radius a, with their centres at the same depth f, and separated horizontally by a distance ℓ.

5.3.1 THE LINEAR THEORY FOR TANDEM CIRCULAR CYLINDERS

The linear theory for the drag on the leading of two identical circular cylinders in tandem beneath a free surface was given by Tuck and Scullen [38] as

$$C_D = \pi e^{-2kf} - (k\ell)^{-3} + \Im\left(e^{-v}\,\mathrm{Ei}^{-}(v) - v^{-1} - v^{-2} - v^{-3}\right)\ , \tag{5.6}$$

where $v = 2kf - ik\ell$, and C_D is the drag coefficient

$$C_D = \frac{D}{4\pi\rho g a^4 k^2}\ . \tag{5.7}$$

In order to evaluate this force, it is in general necessary to compute values of the exponential integral $\mathrm{Ei}^{-}(v)$ with complex argument v, which can be done reasonably efficiently for moderate values of v by summing its Taylor series (Jahnke and Emde [22, page 2]). However, for the relatively-large values of kf and $k\ell$ of prime interest here, a large-v asymptotic expansion is often sufficient, in which only the two leading terms of equation (5.6) need be retained, namely

$$C_D = \pi e^{-2kf} - (k\ell)^{-3} \ . \tag{5.8}$$

The physical interpretation of this formula is as follows. The first term is just the wave resistance of the leading circle in the absence of the trailing circle, and thus is independent of the separation ℓ. The second term is the main local thrust from the interaction between the two circles. Note that this term is independent of depth of submergence, and indeed can be found by ignoring the free surface, and just combining a stream with two simple dipoles in an infinite fluid. This simple approximate formula thus captures the drag and thrust force components due to far-field waves and local pressures respectively. The only change if one reverts to the full linear formula is to give a slightly more accurate estimate of the local thrust term.

The large-v expansion for the drag on the trailing body is also given as

$$C_D = \pi e^{-2kf}(1 + 2\cos k\ell) + (k\ell)^{-3} \ . \tag{5.9}$$

For large ℓ this oscillates between a drag of three times that for a single circle and a thrust equal but opposite in direction to it. The first case corresponds to maximum constructive interference, where the downstream wave amplitude is doubled, and hence the total wave resistance is increased by a factor of four. The latter case corresponds to that of complete destructive interference, where no downstream wave is produced, and hence the total wave resistance is zero.

The total drag on the combination is the sum of the above forces on the two circles, namely (as an exact linear result, without any far-field approximation)

$$C_D = 2\pi e^{-2kf}(1 + \cos k\ell) \tag{5.10}$$

which vanishes when ℓ is an odd multiple of $\pi U^2/g$, as expected.

According to the approximate formula (5.8), the force on the leading cylinder vanishes when

$$kf = \frac{1}{2}\log\left(\pi\,(k\ell)^3\right) \tag{5.11}$$

and a corresponding graph of f versus ℓ is shown as the dotted curve labelled "$a = 0$ (approx.)" in Figure 5.9. On the other hand, setting $C_D = 0$ in the full linear formula

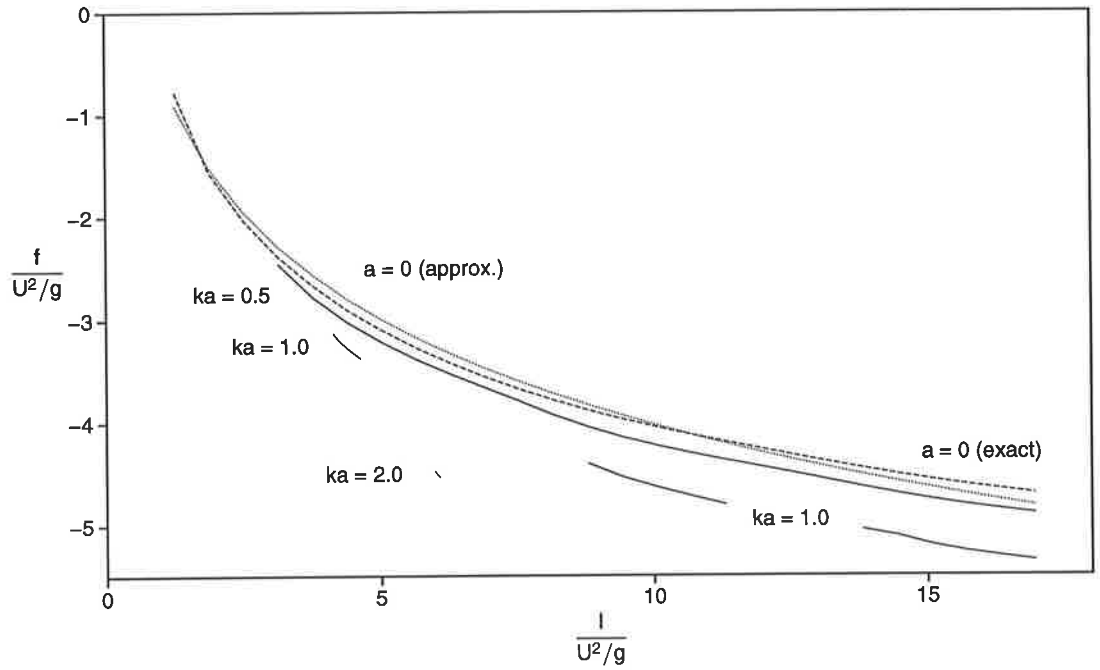

Figure 5.9: Relationship between depth f and separation ℓ yielding zero horizontal force on the leading cylinder, for various dimensionless radii ka. The dotted curve is a far-field approximation (5.11) to the linear ($a = 0$) theory, for which the exact results are shown as the dashed curve.

(5.6), and for each value of ℓ using Newton's method to find the corresponding value of f, gives the dashed curve labelled "$a = 0$ (exact)", the difference from the dotted curve being only a few percent in the range shown. In particular, for the lowest-order wave-cancelling separation $\ell = \pi U^2/g$, the approximate formula gives $kf = \log \pi^2 = 2.289$ whereas the full linear result has $kf = 2.385$, the latter corresponding to a configuration aspect ratio of $f/\ell = 0.7592$. The second wave-cancellation mode $\ell = 3\pi U^2/g$ is such that the far-field approximation $kf = 3.937$ is even closer to the full linear result $kf = 3.974$ (which yields $f/\ell = 0.4216$), and as one moves to higher modes, the separations and depths increase further.

5.3.2 EXACT COMPUTATIONS

The present extension to two submerged tandem cylinders presents no additional difficulties. For a given choice of dimensionless cylinder radius ka and separation $k\ell$, results are first obtained for the drag on the first cylinder as a function of depth f. When the method is applied for cylinders of small radius, the results are close to those given by the linear theory. The secant method is then used to search for the depths f at which the computed force on the leading body vanishes. The results for f as a function of ℓ are in approximately 4-figure agreement with the linear theory at $ka = 0.01$, and still in better than 2-figure agreement at $ka = 0.1$. Thus for all $ka \leq 0.1$, the (dashed) curve labelled "$a = 0$ (exact)" was reproduced to within plotting accuracy by the nonlinear computations.

At higher values of ka, some differences appear. Large cylinders make large waves, and the rate of increase in wave-making (at fixed depth) is greater than the rate at which the thrust due to the local pressure increases with the size of the cylinders. Hence larger cylinders need to be submerged deeper in order to cancel the force on the leading cylinder. Figure 5.9 shows the required depths for $ka = 0.5$, 1 and 2.

Note that the nonlinear computations are incomplete. For example, gaps in the curve for $ka = 1$ are indications that no converged solution could be obtained because of the large amplitude of the waves produced. These waves may indeed have become so steep that there may not even exist solutions in some parameter ranges, the waves having broken at their crests in practice. For the most nonlinear case examined, namely $ka = 2$, the parameter range where solutions are found is so narrow that on the scale of Figure 5.9, it appears as just a very short line segment near $k\ell = 6$, but never-the-less contains interesting results.

There is no guarantee that exact cancellation of the waves made by the combination occurs, since there is no superposition principle for the nonlinear waves that are produced. The wave-cancelling separation values of ℓ depend on f as well as a, whereas in the linear theory they are independent of both. Because the corresponding total drag is non-negative, a parameter search for its near-zero minima is a difficult numerical task. Instead, it is somewhat more convenient to proceed indirectly, as follows. Figure 5.10, like Figure 5.9, contains curves of depth f versus separation ℓ for various fixed values of cylinder radius ka, but now these are depths at which the force on the trailing rather than the leading cylinder vanishes. Configurations with zero force on either cylinder separately are easier to obtain than those for zero total force, since they involve zero-crossings rather than zero minima. Again the results for small radius a agree with the linear theory. Again, for large a, the nonlinear curves are incomplete, but some low-wave results are obtained

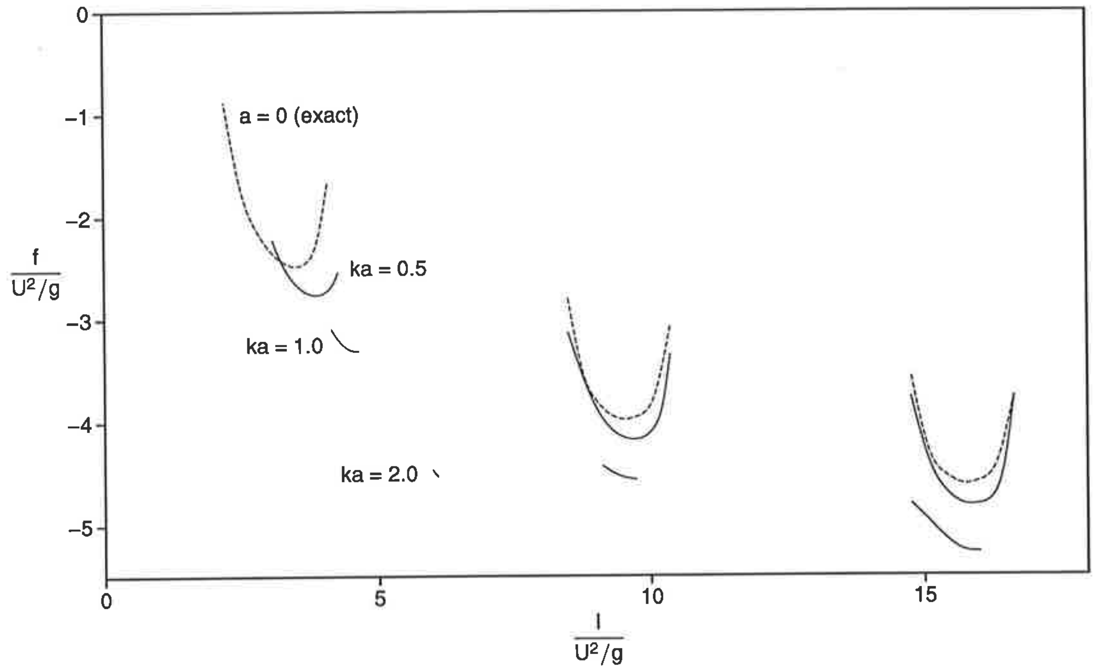

Figure 5.10: Lines of zero horizontal force on the trailing cylinder, for various sized cylinders.

even for ka as large as 2.

For any given cylinder radius a, a configuration with zero force on both cylinders (and hence necessarily with no waves) would be obtained wherever the curves of Figures 5.9 and 5.10 meet. In the linear theory, these curves touch exactly at $\ell = \pi U^2/g$, $3\pi U^2/g, \ldots$, as expected. The nonlinear results indicate that the curves still appear to touch each other, but at larger values of ℓ, which depend on the radius a.

In particular, Figure 5.11 shows an expanded view of a combination of the curves of Figures 5.9 and 5.10, in the neighbourhood of the principal mode $n = 0$ where $\ell = \pi U^2/g$ in linear theory. On the scale of this figure, touching of these two curves appears to occur up to $ka = 1$, and also at $ka = 2$, even though for that radius only a very narrow range of separations from $k\ell = 6.000$ to $k\ell = 6.095$ allows convergence, and the two "curves" appear as indistinguishable short line segments. The depths and separations required for zero force on both cylinders increase quite dramatically with nonlinearity, almost doubling the linear values at $ka = 2$, but their ratio stays almost constant at about 0.75 for the $n = 0$ mode.

Figure 5.12 is a sample of free-surface shapes for cylinders with $ka = 1$. The curves are for a narrow range of values of ℓ as in Figure 5.11, centred about the principal zero-force configuration. At each value of ℓ, the depth f has been chosen as in Figure 5.9 so that

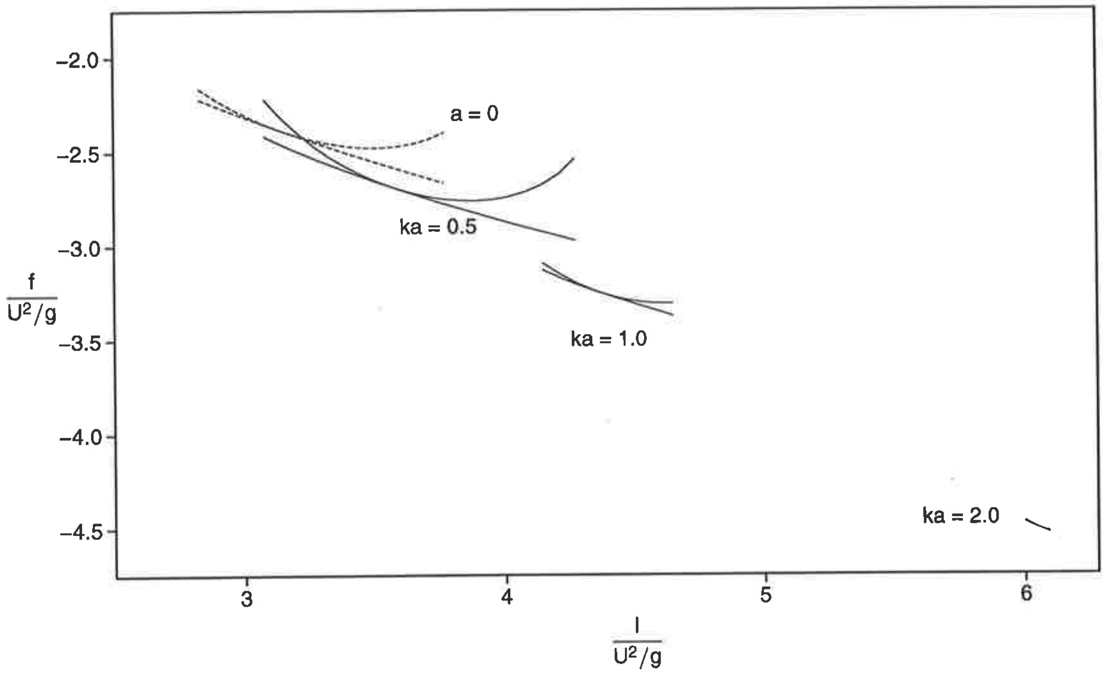

Figure 5.11: Combination of curves of Figures 5.9 and 5.10, in the range of the principal mode n = 0.

there is zero force on the leading cylinder. The least wave amplitude (and hence the least force on the combination) appears to occur at $k\ell = 4.369$ with $kf = 3.254$. This minimum force is zero to within the order of error of the computations.

In Figure 5.12, note the nonlinearity, with sharp crests and broad troughs, of the steepest waves shown, at $k\ell = 4.1$ and $k\ell = 4.7$. The rapid growth of these waves as ℓ departs from the near-zero wave state is a signal for eventual failure of the iterative procedure, and the likely non-existence of non-breaking solutions.

It is also notable in Figure 5.12 that the waves for $k\ell = 4.27$ and $k\ell = 4.46$ are almost out of phase with each other, indicating that a zero-wave state is likely somewhere between them. Indeed, it is possible to find such zero-wave solutions for every value of ℓ by suitable adjustment of f. One point of the present study is that within this family is a unique member having an essentially zero value for the force on each cylinder separately. For $ka = 1$, that member has $k\ell = 4.369$ and $kf = 3.254$.

Similarly, for the even larger cylinders with $ka = 2$, the zero-force member has $k\ell = 6.06$ and $kf = 4.51$. Figure 5.13 indicates the free surface near the cylinders for that member. The flow appears to be fore-aft symmetric. Note the large trough between the cylinders, which has a depth that is more than double the height at which stagnation of the flow would occur. This tandem cylinder configuration is already quite a large local

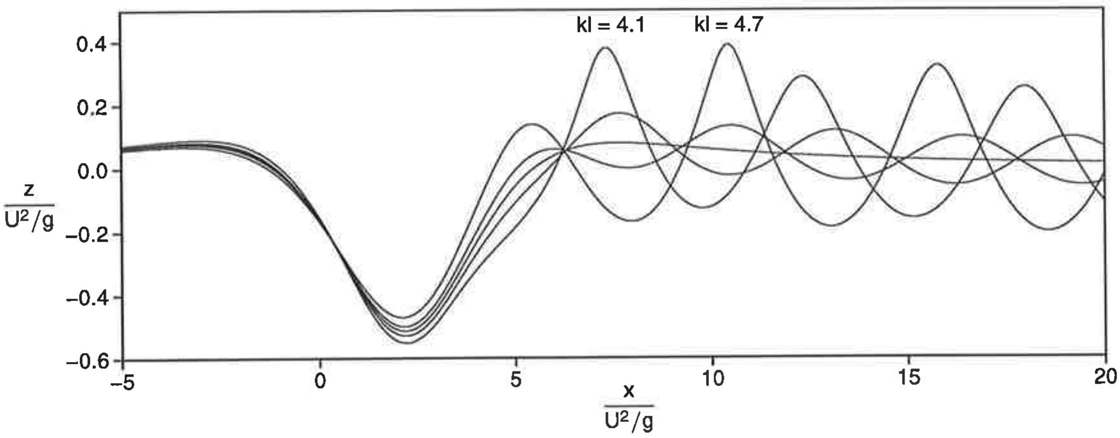

Figure 5.12: Free-surface waves produced by cylinders with $ka = 1$, for $k\ell = 4.1, 4.27, 4.37, 4.46$ and 4.7, all such that there is zero force on the leading cylinder.

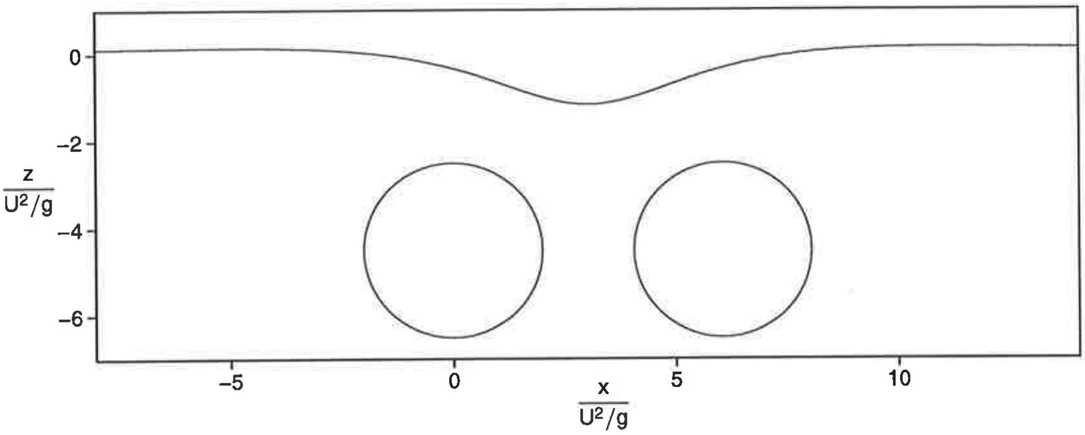

Figure 5.13: Free surface near cylinders with $ka = 2$, $k\ell = 6.06$ and $kf = 4.51$.

free-surface disturber, but never-the-less one which leaves no trailing waves, and has zero horizontal force on each cylinder.

5.3.3 SUMMARY OF OBSERVATIONS

The linear theory applies when a is sufficiently small relative to all other length scales, and suggests that the zero-force configuration is independent of a. A simple far-field expansion based on the theory appears to be of adequate accuracy. The linear conclusion is that, with $\ell = (2n+1)\pi U^2/g$ as discussed above, the zero-force configurations have $f/\ell = 0.759, 0.422, 0.294, \ldots$ for $n = 0, 1, 2, \ldots$.

The linear results are confirmed by use of the present method. For small a, say of the order of a tenth of U^2/g, the asymptotic small-a results are reproduced. By increasing a, the effect of nonlinearity is determined, and results are obtained in a range of values of a up to $2\,U^2/g$. The conclusion is that zero force on either cylinder demands larger depths of submergence and separations when nonlinearity is important, than would be expected from the linear theory.

For depths of submergence yielding non-breaking waves, separations have been found such that the configuration makes no waves far downstream, to within the attainable accuracy. The corresponding flow is fore-aft symmetric, with a large trough between the cylinders and small crests above them. If one compares configurations with separations either just less than or just greater than a waveless value, there is a clear change of phase in the wave produced. In general, for such waveless configurations, there is an equal and opposite force on each of the cylinders separately. However, for each cylinder radius, there is still a discrete set of configurations yielding (to the accuracy of the computations) essentially zero force on both cylinders simultaneously, with the $n = 0$ case having a depth of about three-quarters of the separation.

For very large cylinders, if one further increases or decreases the separation from a waveless value, the wave amplitude rises very steeply and the waves become noticeably non-sinusoidal. For some sufficiently large cylinder radii, computation is feasible only in a very narrow range of separations close to the waveless value. Solutions with non-breaking waves may in fact only exist in this narrow range for such large disturbances.

5.4 CONCLUSION

The flow about a single circular cylinder submerged beneath a free surface has been investigated. The representation of the body, free surface and potential proved to be sufficient for the accurate determination of the solution. For small cylinders, consistency with the linear theories was verified. For larger cylinders, nonlinear effects became apparent, although there was still general agreement with the second order linear theory. There are ranges of Froude number around 0.7 for which solutions cannot be obtained for some large-radius cylinders. Solutions with steep waves were pursued, and some with crest as high as 86% of stagnation height were found.

Attention was then focussed on the submerged circular cylinder with circulation. Consistency with the linear theory, which predicts that wave resistance varies linearly with circulation, was confirmed for cylinders of sufficiently small radius. For larger cylinders however, the range of circulations was increased for which the wave resistance of the cylinder is reduced, sometimes dramatically so.

Finally, the flow past two identical submerged circular cylinders in tandem was considered. The combinations of depth of submergence and separation at which each cylinder feels no horizontal force were determined. Particular attention was given to the discrete combinations at which both cylinders feel no horizontal force simultaneously, and for which there are no waves downstream. The nonlinear effect of nonzero cylinder size is to increase both the depth of submergence and the separation of the two cylinders at which this phenomenon occurs.

THE 1:5 PROLATE SPHEROID

The wave-making properties of the 1:5 prolate spheroid are examined for qualitative consistency with wake properties in general before being compared quantitatively with the appropriate linear theory and other numerical computations. Finally, some interesting nonlinear cases are presented.

6.1 INTRODUCTION

This chapter concentrates solely on a prolate spheroid moving in the direction of its horizontal axis of revolution at a steady speed beneath a free surface. In particular, the spheroid whose radius is one fifth of its length is considered. This case has been investigated previously by others (Doctors and Beck [9], Cao [5], Bertram et al. [4]), and so provides a useful benchmark for the comparison of numerical results. Also, the linear theory proposed by Havelock [17] can be used as a guide to the accuracy of cases of small disturbances.

The content of this chapter is an extension of the research reported previously by Scullen [35]. Some of the results of that paper are reproduced here.

6.2 REPRESENTATION OF THE SPHEROID AND SURFACE

Symmetry of the flow in the plane $y = 0$ is assumed, so only one half of the free surface and body need be represented, with each singularity having an associated image in the other half-space. The surface of one half of the 1:5 spheroid is represented by 15 vertical semi-circles (in half-planes $y < 0$ with x constant), spaced with a cosine weighting in the x-direction so that greater resolution is achieved near the ends. Each of these semi-circles contains 17 nodes that are equally spaced. In addition, nodes are positioned at the leading and trailing ends on the axis of revolution, so that the spheroid is represented by 257 nodes. Singularities are positioned at the points of intersection between the normals to the body nodes and the internal spheroid whose length is 97.4% of the actual spheroids length, and whose diameter at the equator is 15% of the actual spheroids diameter.

This representation was determined from an investigation in which the satisfaction of the Neumann boundary condition was considered for a 1:5 spheroid in a fluid of infinite extent with stream speed U. The boundary condition was enforced at the nodes of the spheroid, and the resulting potential was then used to determine the normal velocities at the nodes when the resolution was doubled, in a similar manner to that which was done for the wave-like body of Chapter 2. Several schemes for the location of singularities were considered, and the intersection of surface normals with an internal spheroid was found to be preferable. Figure 6.1 shows the maximum relative error in the normal velocity on a spheroid of length 1 in a stream of speed 1. The internal lengths shown range from 0.95 to 0.99 in intervals of 0.01, and the internal diameters range from 0.025 to 0.175 in intervals of 0.025. One can see that the minimum error lies near length 0.97 and diameter 0.025. For some cases of small length or diameter, the system of equations cannot be inverted due to poor conditioning. Upon further investigation the optimum is found to be near an internal length of 0.974 with an internal diameter of 0.03, for which the error is less than 0.006 U. The spheroid representation that is used for free-surface flows is based upon this optimum.

For the remaining discussion, the lengths given are for the case where $k = 1$, and hence the fundamental wavelength is 2π. For choices of U and g such that $k \neq 1$, it is necessary to scale all lengths appropriately. The discrete sources associated with the free surface are distributed on a rectangular grid, with 91 rows equally spaced in the x-direction along

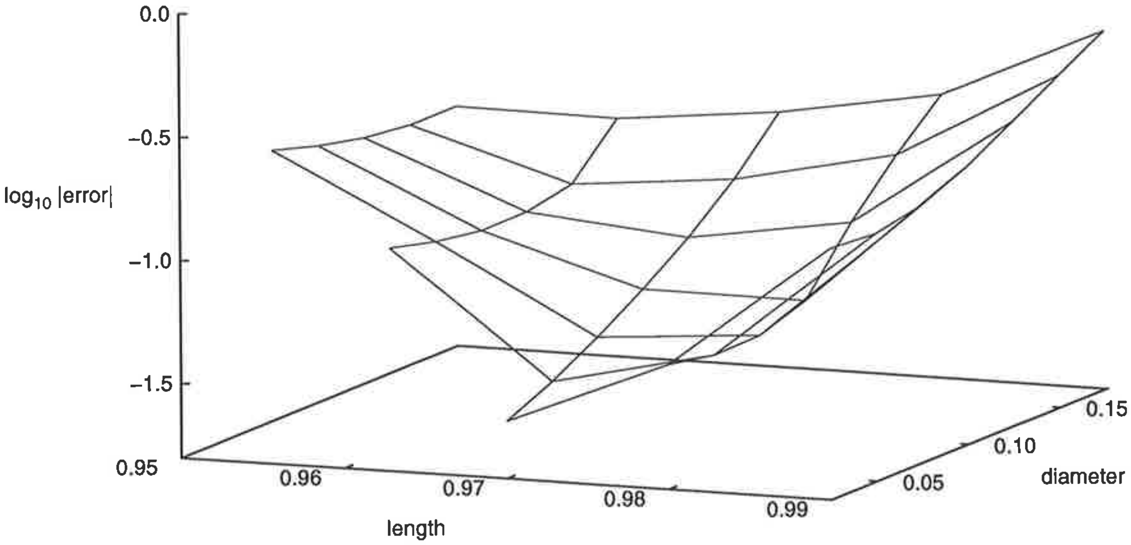

Figure 6.1: Maximum relative error in the Neumann boundary condition on the surface of a 1:5 spheroid of length 1 when the singularities are distributed along normals and on an internal spheroid of various dimensions.

the interval $[-10, 20]$, and 25 columns equally spaced in the y-direction along the interval $[-8, 0]$, and at an offset height of 1.0. Free-surface nodes are located on the plane $z = 0$ beneath each of these singularities, with the exception of the outmost row at both the upstream and downstream ends of the domain. The free-surface boundary condition is enforced at each of the surface nodes, and the radiation condition is enforced at each node in rows 1 and 3, when counted from the upstream end. In total then, there are 2225 free-surface nodes, 257 body nodes, and 2532 singularities.

Preliminary investigations were made in which the forces on a Rankine ovoid were calculated and used as an indication of convergence to the correct solution. This suggested that a domain of length less than 10 is unreliable, with reasonable consistency being observed for domains of length greater than 15. Similarly, grids for which the spacing exceeded 0.7 were inconsistent, with results becoming more reliable as the grid spacing was decreased. Reasonable consistency is found over a range of offset heights. The choices of the parameters for representing the free surface in the above are based in part upon this investigation.

The domain length in the x-direction has also been chosen so that there is a reasonable region upstream of the disturber, and a suitable number of wavelengths (say 4) are captured in the downstream direction. In the y-direction, the domain width is such that the waves are approaching the side of the domain towards the downstream end. The resolution is restricted by practical limitations of current computing facilities. As noted above, the total number of singularities is 2532, and so determination of the flow requires the creation and solution of a system of simultaneous equations of that rank, once per each iteration of the iterative procedure.

The memory requirements of a matrix of this size (on a machine which represents double precision by the usual 64 bits) is approximately 50 megabytes. The nature of the problem is such that an increase in the resolution (in both the x and y directions) by a factor of n results in an increase in memory requirements by a factor of n^4. Consequently, doubling the resolution produces a matrix of size approximately 800 megabytes, and a further doubling would require over 12 gigabytes. One can see that the storage requirements quickly become prohibitive. Additionally, the time required to set up and solve the system grows rapidly (at best in proportion to n^4, and at worst in proportion to n^6 depending upon the inversion routine used), and the process becomes painfully slow. Also, as noted in Section 4.3.3.2, the number of iterations required to reach convergence may also increase as the resolution is enhanced, further increasing the computational burden.

Never-the-less, it is considered that these choices provide an accurate representation of the free surface and spheroid, and this is supported by comparison with the linear theory and numerical computations made by others, as will be shown in Section 6.5.

6.3 QUALITATIVE OBSERVATIONS OF THE WAKE

As a preliminary investigation, the method is tested for qualitative consistency with the properties that are expected to be observed for waves produced by bodies in a three-dimensional flow. Figure 6.2 shows the characteristics of a typical wave pattern. It is produced by a 1:5 spheroid with diameter-to-depth ratio of 0.6, at a Froude number based upon length of 0.8. In particular, one can see both the divergent and transverse wave systems. The wake inhabits a wedge of angle approximately 39°, although exact determination is prevented due to parallax.

The fact that the wake is contained within a wedge that has a half-angle of $\arcsin 1/3$ is intriguing. It is true within the linear theory for all disturbances, irrespective of size,

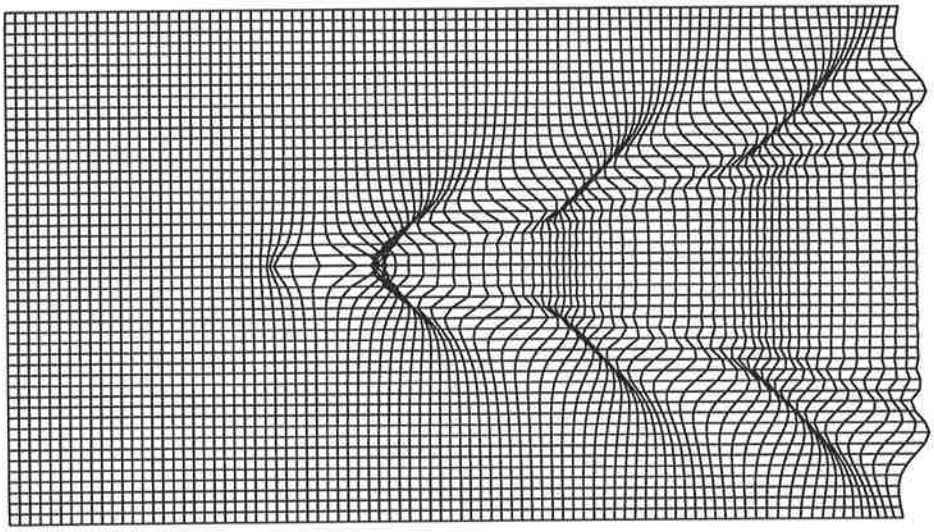

Figure 6.2: The usual characteristics of a wake include the transverse and divergent wave systems contained within a wedge of angle approximately 39°.

shape, speed or depth of submergence. It is a direct consequence of the facts that from the frame of reference of the disturber, the wake appears to be steady state (which therefore determines the velocity at which the waves are moving in any given direction), and that from the frame of reference of the fluid, energy propagates at half the speed at which the waves move. These two points prescribe the envelope within which the waves must be contained. The result applies (reasonably well) to ducks paddling on Adelaide's River Torrens, the hippopotamus swimming in its pool at the Singapore zoo, the twin screw steamer TSS Earnslaw that carries tourists across Lake Wakatipu from Queenstown in New Zealand, and super-tankers in international shipping waters!

Figure 6.3 has a series of surface plots which show the change in the wave pattern as the Froude number $F_l = U/\sqrt{gl}$, based upon the length of the spheroid l, is varied. When interpreting these figures, it is important to realise that the x and y axis are not on the same scale, so the wedge appears significantly less acute than it actually is. Also, the change in Froude number is achieved through a change in depth of submergence, and therefore (since the diameter-to-depth ratio is held constant at 0.6) as the Froude number is increased, the absolute size of the spheroid decreases. Consequently, for the first surface plot (for which $F_l = 0.2$) the body is larger than the computational domain, and this results in non-zero free-surface elevation at the extremes of the domain. (Note however that this situation is accepted only for the qualitative discussions here. For the quantitative results that are to follow, the domain and body lengths are chosen more appropriately.)

The plots show a clear transition from wakes in which the dominant waves are of a transverse nature for low Froude number (for example $F_l = 0.4$), through to those for which the wave pattern consists almost entirely of divergent waves ($F_l = 1.2$). For Froude numbers between these two extremes, the wake consists of both wave systems, as can be seen clearly in the plot for $F_l = 0.8$.

Some grid-scale oscillation in the free surface can be seen in the wake near the downstream end for the case $F_l = 1.2$. The divergent nature of the waves in this region implies a very short wavelength for those waves moving in the lateral directions, and this is the cause of the grid-scale oscillation. This is essentially unavoidable, since the problem will appear inevitably for a larger Froude number even if a finer resolution grid is used. As such, it is expected to be a difficulty that is inherent to three-dimensional flows at high Froude number, and will most probably be encountered irrespective of solution method.

Figure 6.4 shows the disturbance to the free surface as seen from side-on, also for the spheroid of diameter-to-depth ratio 0.6. The largest deviation from the plane $z = 0$ corresponds to the centre line of the domain, with the amplitude tending to decrease towards the outer edges of the domain. At low Froude number, the wave shapes are clearly transverse, and they become progressively more divergent as the Froude number increases.

In each case the domain extends for an interval of $[-10, 20]$ in the x-direction, and the double-headed arrow indicates the length of the spheroid. For the case with $F_l = 0.2$, the body has length 25, and is centred on $x = 0$, so that it extends beyond the upstream end of the domain. One can see that the waves are of small amplitude, and are super-imposed upon the disturbance to the free surface due to the shape of the body. At either end of the spheroid, there is a stagnation point within the fluid, and consequently a region of high pressure, which is reflected by the elevation of the free-surface above these points. By comparison, the fluid moves quickly along the midsection of the spheroid, and the resulting lower pressure creates a depression in the free surface. It is in this context that the corresponding wake pattern for $F_l = 0.2$ in Figure 6.3 is best understood. For higher Froude numbers, the body is smaller, and the effect is less noticeable.

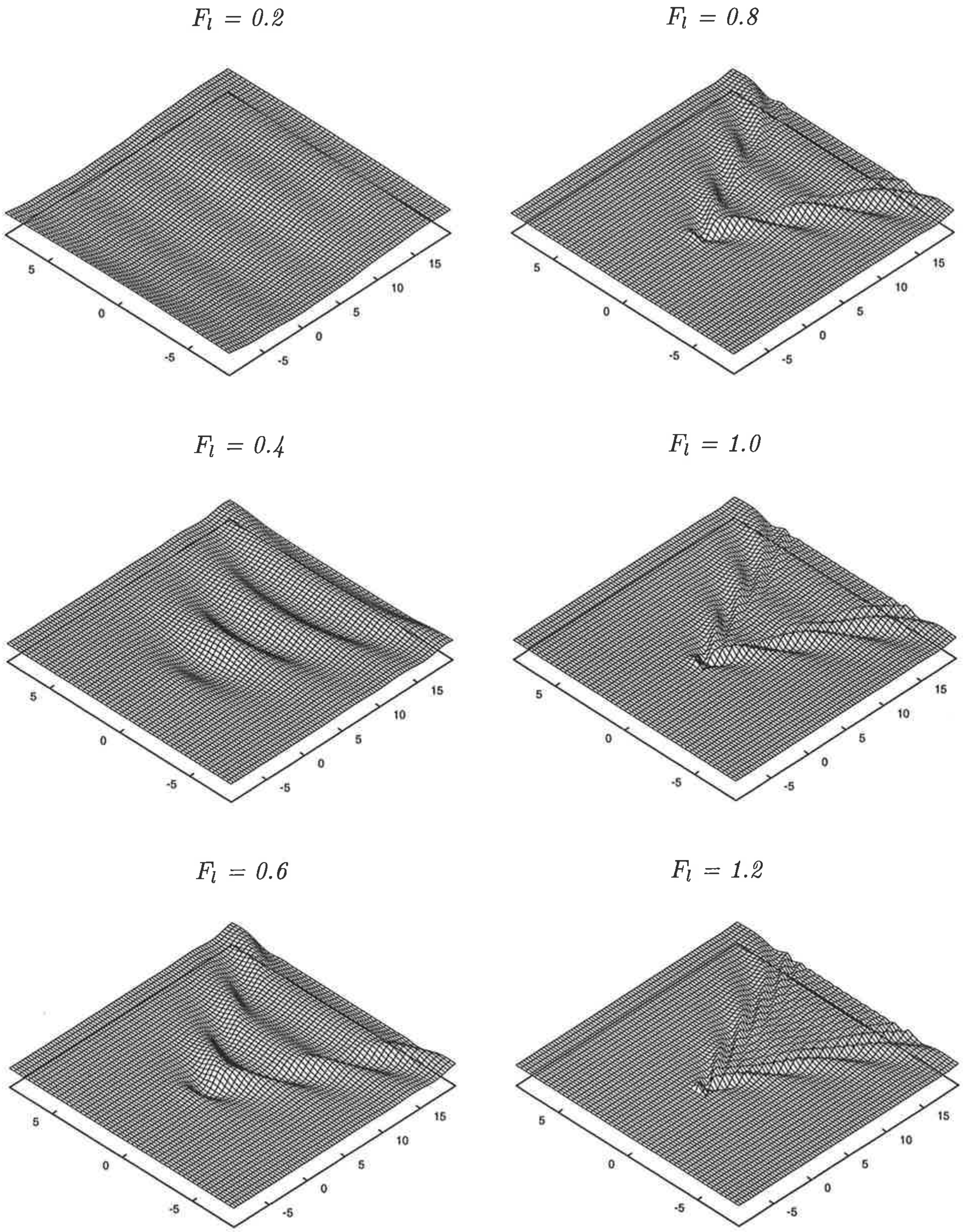
$F_l = 0.2$

$F_l = 0.8$

$F_l = 0.4$

$F_l = 1.0$

$F_l = 0.6$

$F_l = 1.2$

Figure 6.3: The characteristics of the wake change from being composed predominantly of transverse waves to being composed predominantly of divergent waves as the Froude number is increased.

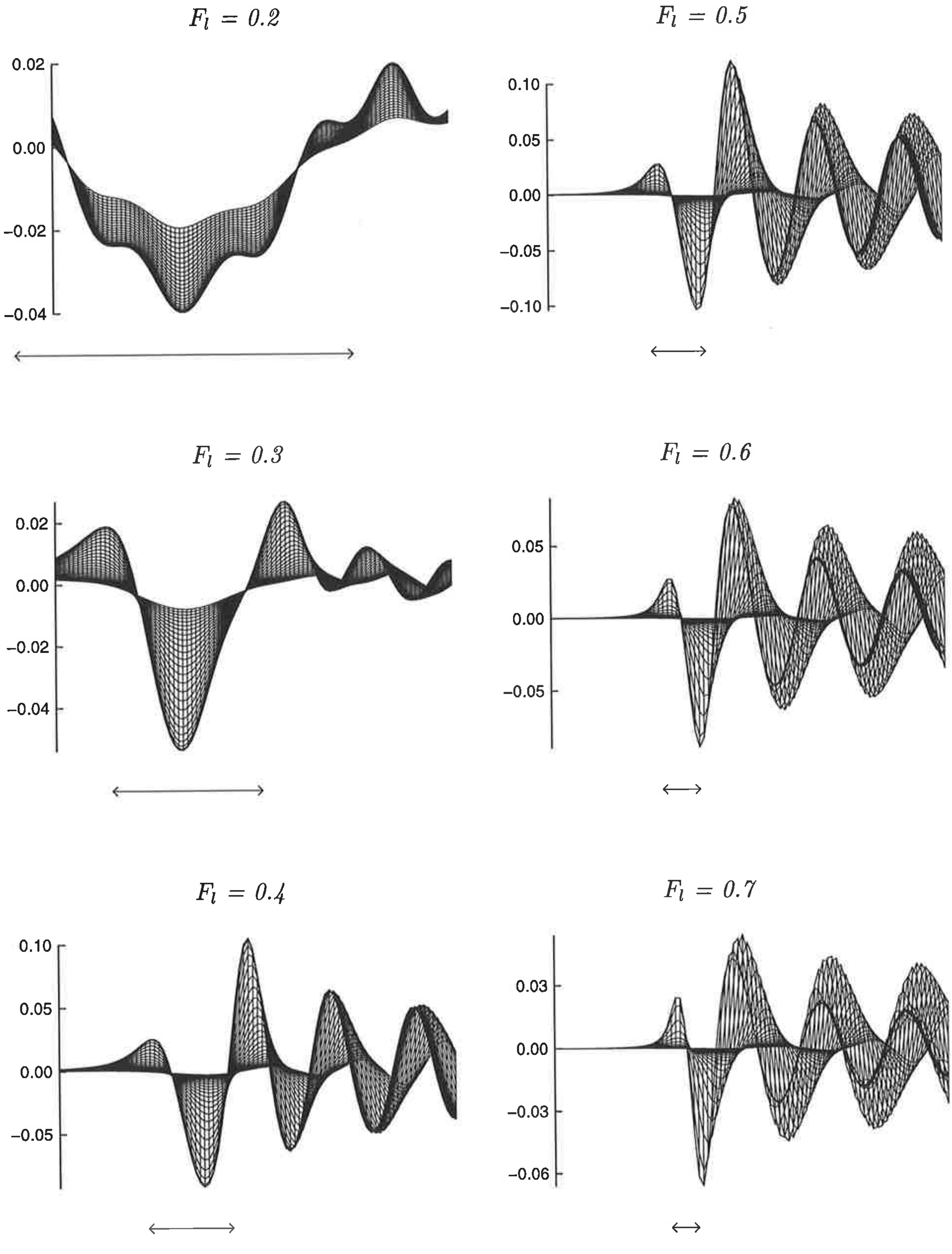

$F_l = 0.2$

$F_l = 0.5$

$F_l = 0.3$

$F_l = 0.6$

$F_l = 0.4$

$F_l = 0.7$

Figure 6.4: The nature of the free surface as seen from the side.

Noticeable along the centre line is the decay in amplitude as the wave moves downstream. The wave energy should decay in proportion to the distance, and therefore the wave amplitude should decay in proportion to square root of distance. The results shown are consistent with this expectation.

In general then, there is reasonable agreement with what can be expected qualitatively for three-dimensional free-surface flows. In particular, the radiation condition is satisfied, and waves do not exist far upstream of the body.

6.4 THE LINEAR THEORY FOR A PROLATE SPHEROID

The linear theory for the forces experienced by a submerged spheroid was determined by Havelock [17] using a distribution of dipoles of appropriate moment between the foci of the spheroid. According to the theory, the wave resistance is

$$R = 16\pi^2 \rho g l^3 \epsilon^3 A^2 \int_0^{\frac{\pi}{2}} e^{kf\sec^2\theta} \left\{ J_{\frac{3}{2}}\left(0.5kl\epsilon\sec\theta\right)\right\}^2 \sec^2\theta \, d\theta \,, \tag{6.1}$$

where ϵ is the eccentricity of the spheroid

$$\epsilon = \sqrt{1-(d/l)^2} \,, \tag{6.2}$$

d is the diameter of the spheroid at its equator, A is defined by

$$A^{-1} = \frac{4\epsilon}{1-\epsilon^2} - 2\log\frac{1+\epsilon}{1-\epsilon} \,, \tag{6.3}$$

and $J_{\frac{3}{2}}$ is the Bessel function of the first kind of order 3/2. The other variables have their usual meanings, with $k = g/U^2$.

One can see at once that the size (characterised by l) of the spheroid is inextricably associated with the integrand, and so there is no "universal curve" independent of spheroid size for a given choice of shape (eccentricity), as there is for a circular cylinder (as given by equation (5.2) on page 80) or a submerged sphere (see equations (7.6) and (7.8) on page 124). This should not be a surprise, since it is only the fact that both the circular cylinder and sphere can be described by singularities located at a single point that allows them this special property. For these two bodies, any variation in size is achieved by a change in the strength of the singularity only. For a spheroid, any variation in size will also require a change in the location of the singularities.

However, the theory can be completely described by three dimensionless parameters, and it is convenient to use d/l, d/f and F_l. The first of these describes the shape of the spheroid and is equivalent to its eccentricity, the second its depth of submergence, and the third is the Froude number based upon spheroid length. In this instance and since there is no universal curve of appropriately scaled wave resistance when plotted versus Froude number as based upon depth of submergence, it seems somewhat more natural to use this alternative definition of Froude number.

In terms of these dimensionless parameters, the wave resistance is given by

$$\overline{R} = 96\pi \, (d/l)^{-2} \, \epsilon^3 A^2 \int_0^{\frac{\pi}{2}} e^{F_l^{-2}(d/l)(d/f)^{-1} \sec^2\theta} \left\{ J_{\frac{3}{2}} \left(0.5 \, F_l^{-2} \epsilon \sec\theta \right) \right\}^2 \sec^2\theta \, d\theta \, , \qquad (6.4)$$

where $\overline{R}$ is the wave resistance when made dimensionless by scaling with respect to the buoyancy of the spheroid, and is therefore defined as

$$\overline{R} = \frac{R}{\frac{\pi}{6}\rho g l d^2} \, . \qquad (6.5)$$

This dimensionless wave resistance is shown in Figure 6.5 as a function of Froude number for the 1:5 prolate spheroid over a range of values of the parameter d/f. It is observed that for small or deep spheroids such that $d/f = 0.2$, the maximum occurs near $F_l = 1.0$, and that the Froude number of maximum resistance decreases as d/f is increased, until for $d/f = 1.2$ it appears near $F_l = 0.6$.

6.5 WAVE RESISTANCE AND LIFT RESULTS

Initially, verification of consistency between the linear theory as predicted by Havelock and the results as computed by the current method is sought. In particular, the wave resistance of the spheroid whose diameter is 0.2 of the depth of its submergence is investigated. With this choice of d/f, the length of the body is in fact equal to the depth of submergence, and some small discrepancies due to nonlinear effects may still be anticipated.

As noted above, the domain length of $[-10, 20]$ is inappropriate for accurate computation in many cases, since it is possible at low Froude number that the body extends beyond the edge of the domain. Similarly, at high Froude number the body may become small in comparison to the size of the free-surface grid size. A more appropriate choice for domain length is based upon the length of the body. For this purpose, a singularity

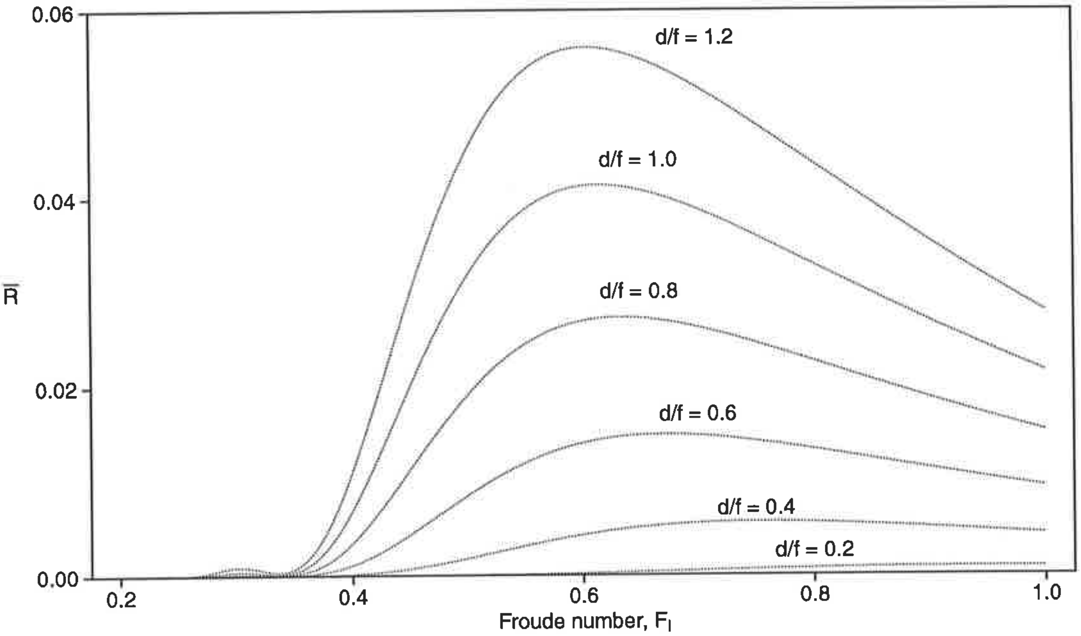

Figure 6.5: The dimensionless wave resistance as predicted from the linear theory for a range of Froude numbers and ratios of diameter to depth of submergence.

grid that extends from $-1.25\,l$ to $2.5\,l$ with 61 rows in the x-direction and from $-0.75\,l$ to zero with 16 columns in the y-direction is adopted. An offset height of 3 times the grid spacing in the x-direction is used to determine the height at which the singularities are located. The free-surface nodes are initially positioned relative to the singularity grid in the manner described above. The representation of the spheroid remains unaltered.

The results are shown in Figure 6.6, and are generally in good agreement, with the discrepancy being about 2% of the wave resistance at $F_l = 1.0$.

The solution is determined subsequently for Froude numbers in the range $[0.3, 1.0]$ and for diameter-to-depth ratios of d/f = 0.2, 0.4, 0.6, 0.8, 0.9, 1.0, 1.1 and 1.2. The wave resistance is calculated, and Figure 6.7 shows the results. The solid curves represent the nonlinear wave resistance, and the dotted lines represent the linear theory. Note that the curves are not complete for the values of d/f greater than 0.8, since for some of these cases converged results cannot be obtained.

The present method shows that for larger disturbances, the linear theory under-predicts the wave resistance at low Froude number, and over-predicts at high Froude number. The largest inaccuracies occur for large diameter-to-depth ratios at low Froude number, for example $d/f = 1.0$ at $F_l = 0.4$, for which the wave resistance is under-

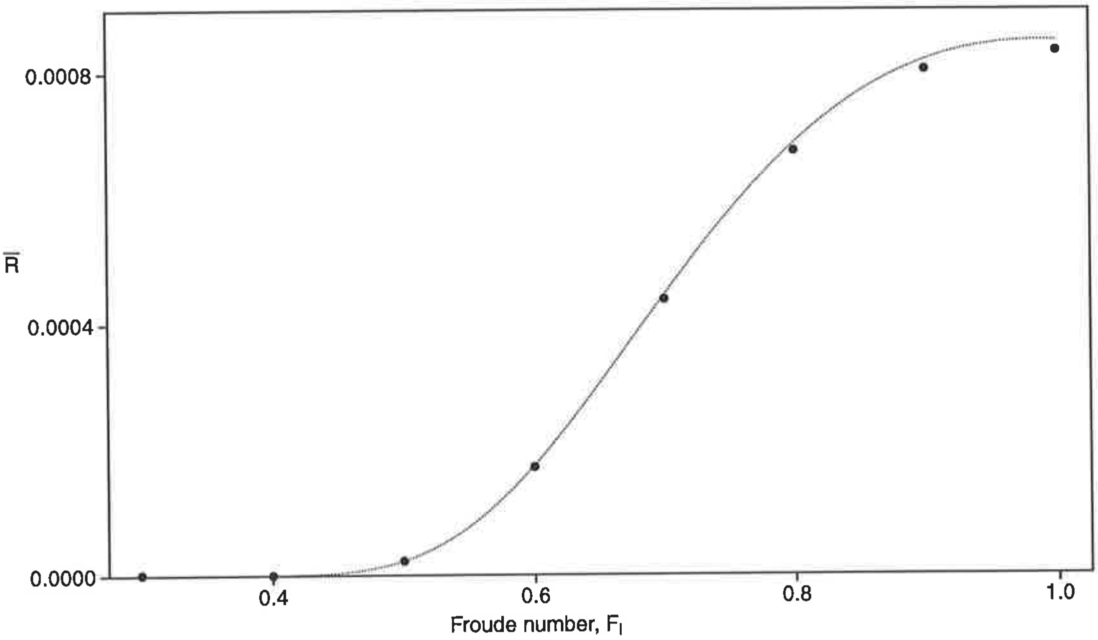

Figure 6.6: Comparison of wave resistance as determined by the current method with that predicted by the linear theory for the case $d/f = 0.2$.

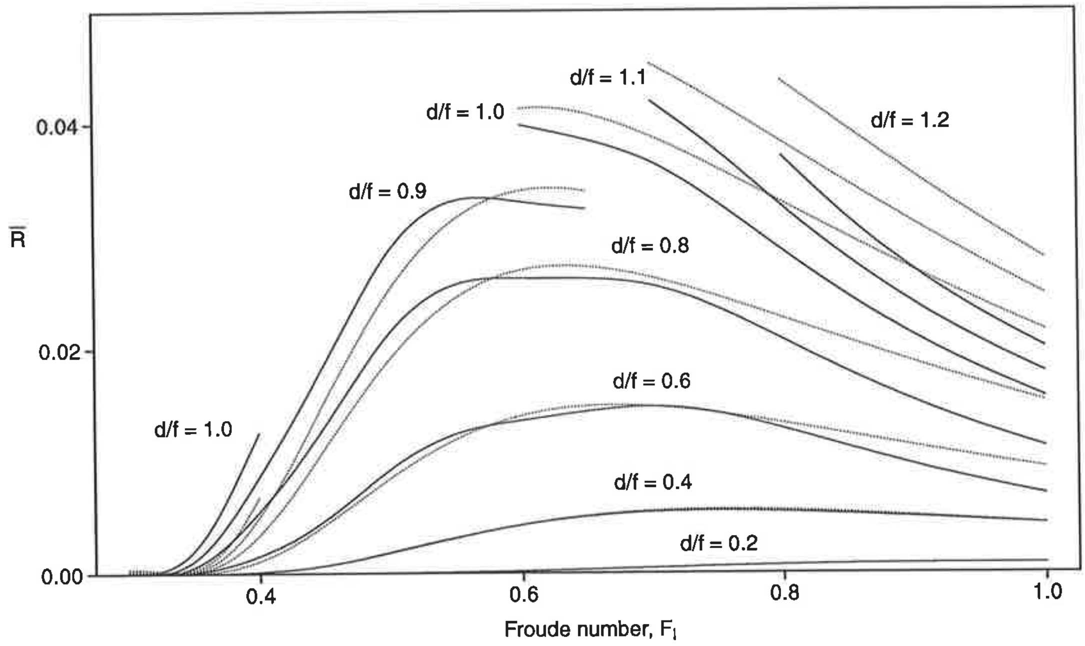

Figure 6.7: Comparison of wave resistance as determined by the present method (solid lines) with that predicted by the linear theory (dotted lines) for various values of d/f.

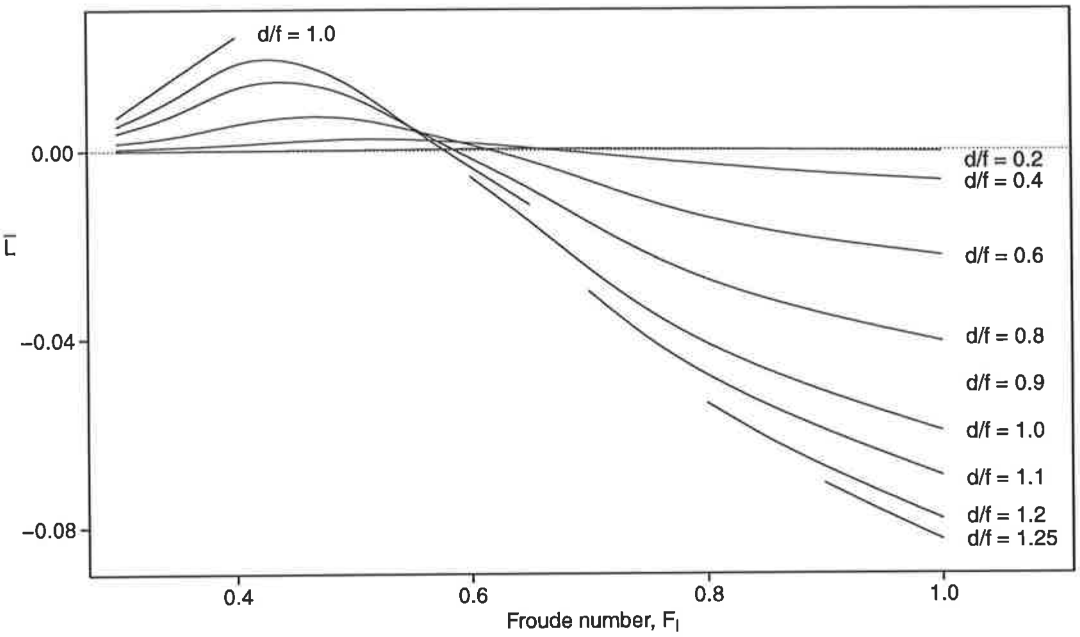

Figure 6.8: Dimensionless lift force as determined by the present method.

predicted significantly. Never-the-less, the investigation shows that the linear theory provides quite a reasonable approximation to the drag for much of the ranges of Froude number and d/f considered.

The lift forces for these same cases are shown in Figure 6.8. The lift force has also been made dimensionless by scaling with respect to buoyancy. For each value of d/f, there is a transition from a lift to a down-force, usually at a Froude number of approximately 0.6.

As mentioned in the introduction, the case of the 1:5 spheroid has been studied previously by others, and as such is a useful benchmark. Figure 6.9 shows the results of the present method in comparison those reported by Cao [5] which included results produced by Doctors and Beck [9], and Bertram et al. [4]. The particular case reported here is that of a spheroid with a depth-to-length ratio of 0.245, which corresponds to a diameter-to-depth ratio of approximately 0.816. All five methods are in good agreement for forces of both wave resistance and lift. The numerical methods employed by Doctors and Beck and Cao were time dependent formulations that were extrapolated to approximate the steady state. The method employed here, being a steady state calculation, is computationally inexpensive by comparison.

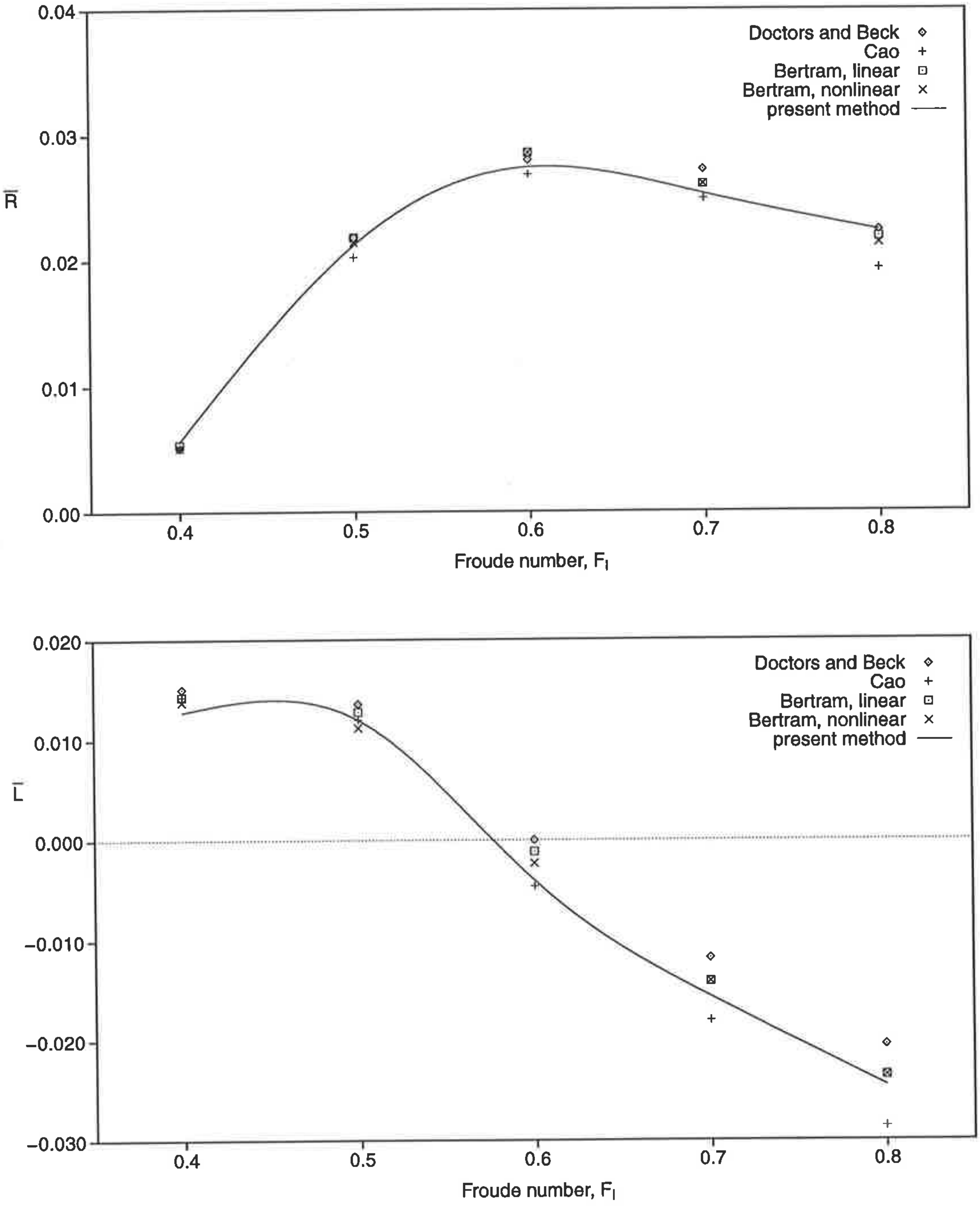

Figure 6.9: Comparison with numerical results obtained by Cao and others for the case of a spheroid with a diameter-to-length ratio of 0.245, which corresponds to a diameter-to-depth ratio of approximately 0.816.

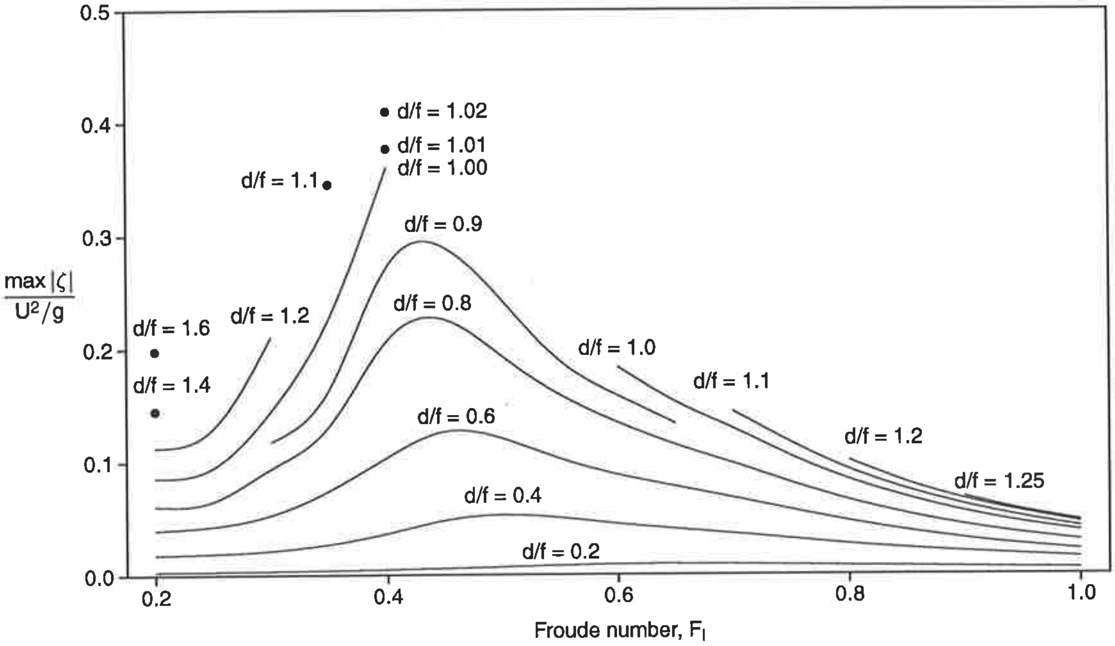

Figure 6.10: Maximum deviation of the free surface from the plane $z = 0$ for various values of d/f. The amplitude is scaled with respect to U^2/g so that 0.5 is the stagnation height, and hence an unobtainable upperbound.

6.6 WAVE HEIGHT AND CASES OF SPECIAL INTEREST

Figure 6.10 shows the maximum deviation (made dimensionless by scaling with respect to U and g) of the free surface from the plane $z = 0$ for several cases. Solutions can be obtained throughout the range of Froude numbers from 0.2 to 1.0 for values of d/f up to and including 0.9, for which the spheroid is submerged shallowly. For larger disturbances (greater values of d/f), solutions at Froude numbers between 0.4 and 0.6 cannot be obtained. At the Froude number of 0.20, a solution was found for a spheroid with a d/f value of 1.6. This is a particularly shallow body, as the depth of the top of the body is only one eighth of its diameter.

Of particular interest here are the regimes in which the flows show strongly-nonlinear characteristics, as it is in these cases that the nonlinear nature of the solution method has its greatest advantage. One such case is that of a body that is submerged shallowly in comparison to both its diameter and the amplitude of the waves that it creates. The spheroid with a diameter-to-depth ratio of 1.25 and Froude number of 1.0 is a suitable example of this. The top of the body is at a depth that is 0.3 of the diameter, and is

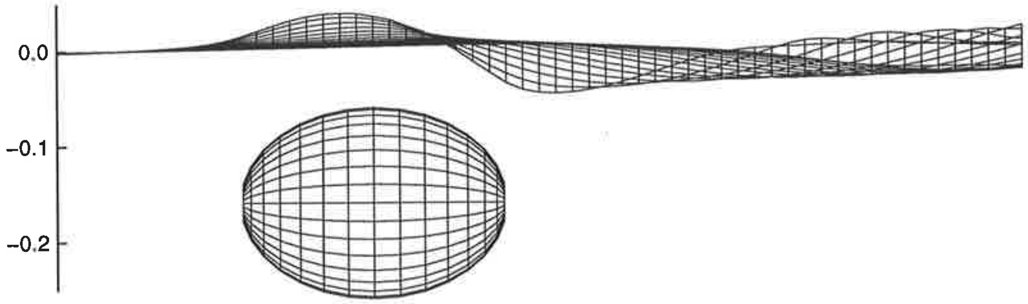

Figure 6.11: Side view of the free surface above a spheroid with d/f = 1.25 at Froude number 1.0. The top of this body is at a depth comparable to that of the first trough.

roughly the same as the depth of the first trough. This can be seen clearly in Figure 6.11. Note that the x and z axes are not drawn to scale, but recall that the ratio of diameter to length for the spheroid is 1:5.

Also of interest is the rapid growth in wave amplitude as the disturbance becomes large. In such a regime, small changes in depth produce large changes in wave height, the waves display significantly nonlinear characteristics since the first crest is considerably sharpened, and it can be argued that the waves are nearing a steepness at which they would break. Example of such cases are d/f values of 1.00, 1.01 and 1.02 at a Froude number of 0.4, for which the maximum crest heights are shown in Figure 6.10. Note the rapid growth, and recall that in these dimensionless units, the stagnation height is 0.5. It is likely that a wave breaks before its crest reaches stagnation height. Figures 6.12 and 6.13 show the case where the diameter-to-depth ratio is 1.02. It is reasonable to expect that only a small increase in the disturbance would result in a breaking wave.

It is also important to note that the achievable maximum height is dependent upon Froude number. The wake can be considered to be composed of an infinite number of planar wave systems, each moving at some angle to the direction of the body's movement. For an infinitely deep fluid, the wavelength for a system of waves at angle θ is given by $2\pi \cos^2\theta\, U^2/g$, and therefore decreases as θ is increased. Since there is a maximum obtainable steepness (approximately 0.14) for such Stokes-wave systems, they will break before their crests reach a height of $0.5 \cos^2\theta\, U^2/g$. (This height may be exceeded at isolated points in the wake due to constructive interference, but would be an exception rather than the rule.) Consequently, one can expect the achievable maximum height to

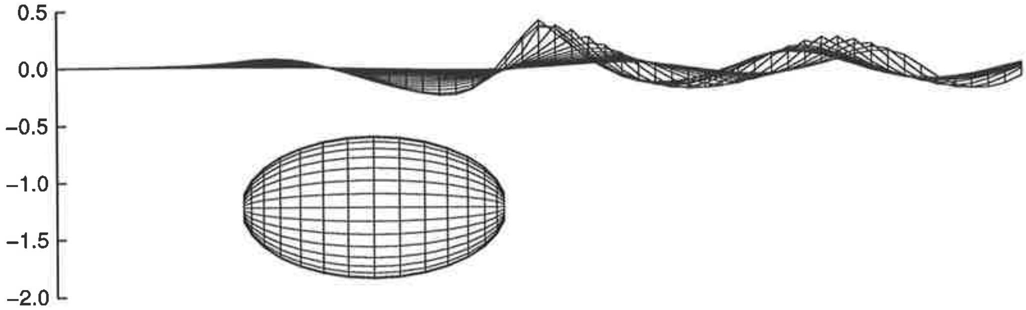

Figure 6.12: The steep wave produced by a spheroid with $d/f = 1.02$ at a Froude number of 0.4.

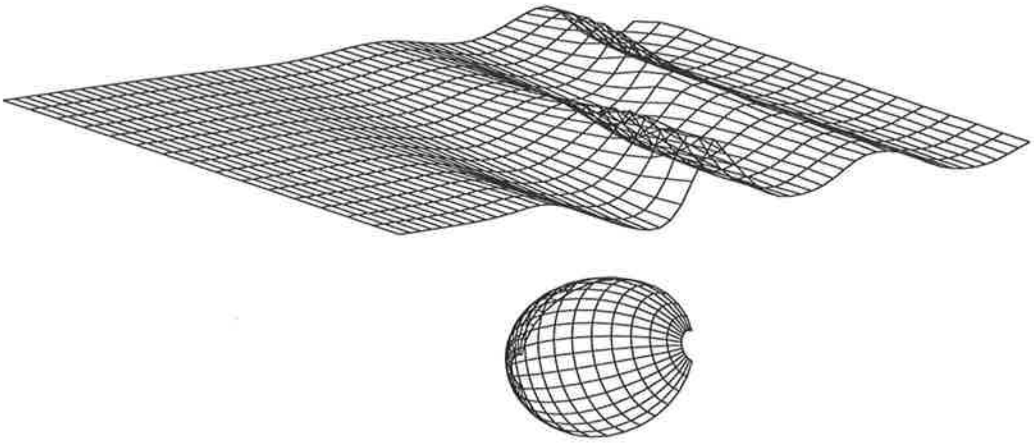

Figure 6.13: A different view of the same case as for Figure 6.12.

be greater for wakes that are composed predominantly of transverse wave systems (that is, for low Froude numbers) than for those composed predominantly of divergent wave systems (high Froude number), and this trend can be observed clearly in Figure 6.10.

6.7 CONCLUSION

Results produced by the current method are consistent with the linear theory approximation for sufficiently small disturbances. The present method shows that for larger disturbances the linear theory under-predicts the wave resistance at low Froude number, and over-predicts at high Froude number. Never-the-less, the investigation shows that the linear theory provides quite a reasonable approximation of drag over the range of Froude numbers and disturbances considered. Additionally, the current method compares well with numerical results produced previously by others. The results obtained are of greatest value when considering cases for which the solution exhibits strongly-nonlinear characteristics, as accurate solutions for such cases cannot be obtained from the linear theory. Some interesting examples of such flows have been presented.

DISTURBANCES IN A FLUID OF FINITE DEPTH

The wave-making of spheres and spheroids in a fluid of finite depth is investigated, and the resulting forces are calculated. For the case of the submerged sphere, consistency is established with the linear theory for flows in a semi-infinite fluid, and also for subcritical flows in a finite-depth fluid, before nonlinear effects are determined. For the spheroid, consistency is shown with the linear theory in a semi-infinite fluid, and finite depth flows are subsequently considered.

7.1 INTRODUCTION

One of the main objectives of this chapter is to investigate the effects of a bed on the wave resistance of a submerged 1:5 spheroid. However, in the absence of a linear theory with which to show consistency, it is considered best to infer accuracy of the results by obtaining supporting evidence from other related flows. The approach taken is as follows.

Firstly, flows about spheres in a semi-infinite fluid are considered, and consistency with the linear theory is established. In doing so, the representations of the sphere, free surface and velocity potential are shown to be suitable. Then, a fluid bed is introduced, and again numerical results are compared with the linear theory, this time being that for a finite-depth fluid. It is found that due to reflection of wave energy from the sides of the computational domain, the results are inaccurate for supercritical flows. The subcritical flows are, however, quite reasonable.

Next, attention is directed to spheroids, and the semi-infinite fluid case is revisited briefly, again establishing the suitability of the body, surface and potential representations. Finally, restricting attention to subcritical flows (for which the results for a sphere are accurate), finite depth effects for flows about submerged spheroids are considered.

7.2 EFFECTS OF A FINITE-DEPTH FLUID

The analyses so far have been of disturbances beneath the free surface of a semi-infinite fluid. The situation becomes somewhat more interesting if a bed is introduced, so that the fluid is of finite depth.

In the early part of this century, Havelock completed several valuable investigations into the nature of waves in a stream of finite depth. In an early paper [12], he considered a point impulse acting on the surface of a fluid of finite depth. His results include the angle of the wedge within which the wake must be confined. He noted that the wedge angle has a limiting value consistent with that of a semi-infinite fluid (that is, approximately 39°) for fluid-depth-based Froude numbers $F_h = U/\sqrt{gh}$ (where h represents the fluid depth) nearing zero, but that in general the wedge angle is different to this, and has a maximum of 180° at the critical fluid-depth-based Froude number $F_h = 1$, and decreases to zero with further increase in F_h. More specifically, he determined that the half-angle of the wedge is given by

$$\alpha = \begin{cases} \arccos \frac{\sqrt{8(1-n)}}{3-n} & \text{for} \quad F_h < 1 \\ \arcsin F_h^{-1} & \text{for} \quad F_h > 1 \end{cases}, \tag{7.1}$$

where

$$n = \frac{2F_h^{-2}}{\sinh\left(2F_h^{-2}\right)}. \tag{7.2}$$

Figure 7.1 shows the curve produced by these equations, with the angle converted to degrees for ease of interpretation. Note that the curve is sharply cusped at the critical Froude number $F_h = 1$, where the maximum value of 90° is obtained. The half-angle is less than 55° at $F_h = 0.99$, and less than 65° at $F_h = 0.999$. By comparison, the supercritical branch decays slowly to zero, with the half-angle being approximately 65° at $F_h = 1.10$, and 55° at $F_h = 1.22$.

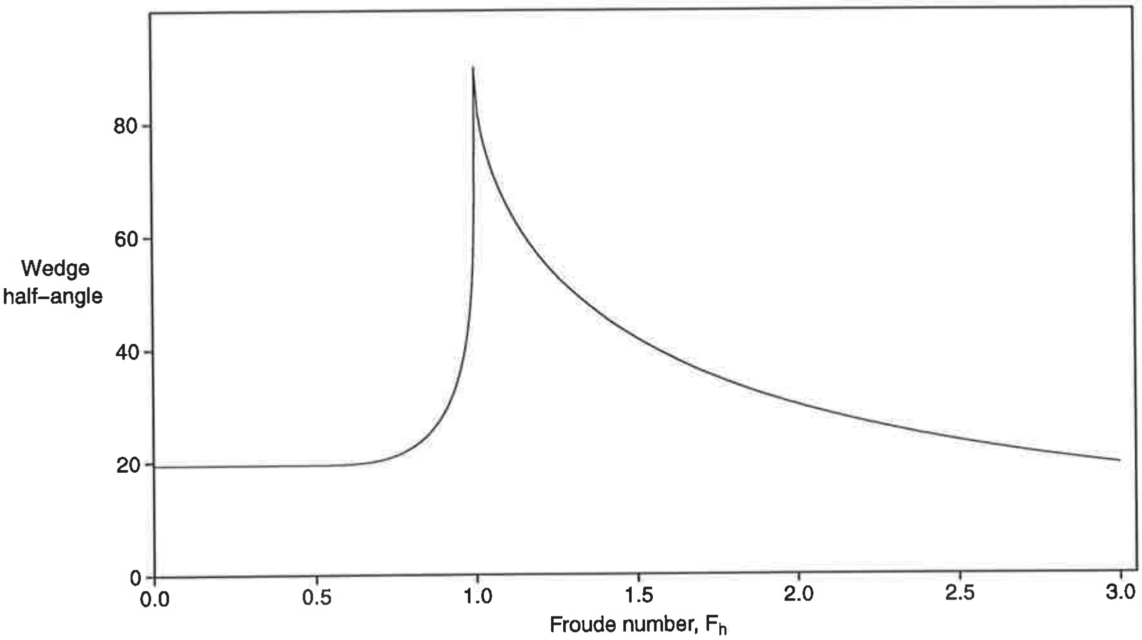

Figure 7.1: Curve representing the half-angle of the wedge within which the wake produced by a point impulse in a fluid of finite depth must be contained.

He also made the point that the wavelength along the centre-line of the wedge increases as a function of fluid-depth-based Froude number, until at the critical value, the wavelength is infinite. Furthermore, for supercritical flows (that is, those for which the fluid-depth-based Froude number exceeds unity), only the divergent wave system exists, the transverse waves having vanished.

Later, Havelock [13] determined the wave resistance of a symmetrical surface pressure distribution about a point moving over a surface of a fluid of finite depth, and included a figure showing wave resistance for several choices of a fluid-depth parameter. He noted that as this parameter tends to infinity, the result for the semi-infinite fluid case is obtained. For finite values of the fluid-depth parameter, regions of increased wave resistance can be observed, and in some instances, the region becomes a second local maximum. At large values of fluid-depth-based Froude number, the wave resistance is diminished. It is anticipated that these characteristics may also be observed in problems involving flow around submerged bodies.

7.3 QUALITATIVE BEHAVIOUR OF THE WAKE

The method was modified to incorporate an impermeable horizontal boundary. This was achieved in an analogous way to lateral symmetry, by incorporating for each singularity an image beneath the boundary, such that the combination satisfied exactly the Neumann boundary condition on the bed. It was then a simple matter to generate flows about bodies submerged in a fluid of finite depth. The current application is to the wave-making properties of spheres and spheroids.

Qualitative observations are made first. Figure 7.2 shows the wakes generated by a spheroid at various fluid-depth-based Froude numbers spanning the critical value of one. These can be compared to those shown in Figure 6.3 on page 107, for which the fluid is of infinite depth. Specifically, the 1:5 spheroid has diameter-to-depth ratio $d/f = 0.6$, and the fluid depth is chosen to be the same as the length of the spheroid. With these choices, F_l and F_h are equal, and the ratio of fluid depth to body depth is $h/f = 3$. The wedge widens as F_h increases from 0.80 to 0.90 and 0.95, the change being manifested in the growth in amplitude of the leading waves near the side of the computational domain. At $F_h = 1.00$, the wedge is clearly not as wide as predicted, and this is perhaps due to the steepness of the wedge-angle curve of Figure 7.1 at the critical Froude number, in combination with some nonlinear effects (recall that at $F_h = 0.999$, the wedge half-angle is less than 65°). As the fluid-depth-based Froude number increases from 1.0 the wedge gradually narrows again, observable in the shift downstream of the leading wave. In addition, there are no transverse waves for the supercritical flows. The cases for larger values of F_l suffer from grid-scale oscillation for the same reasons as was discussed in the previous chapter. The results do, however, appear to be in qualitative agreement with those that can be anticipated from the linear theory.

7.4 SPHERES

Having established the general characteristics that can be expected for flows in a fluid of finite depth, and showing that the method is capable of producing results that appear to be qualitatively consistent with these expectations, attention is directed to the quantitative evaluation of some of the properties of flows about spheres. The sphere proves to be

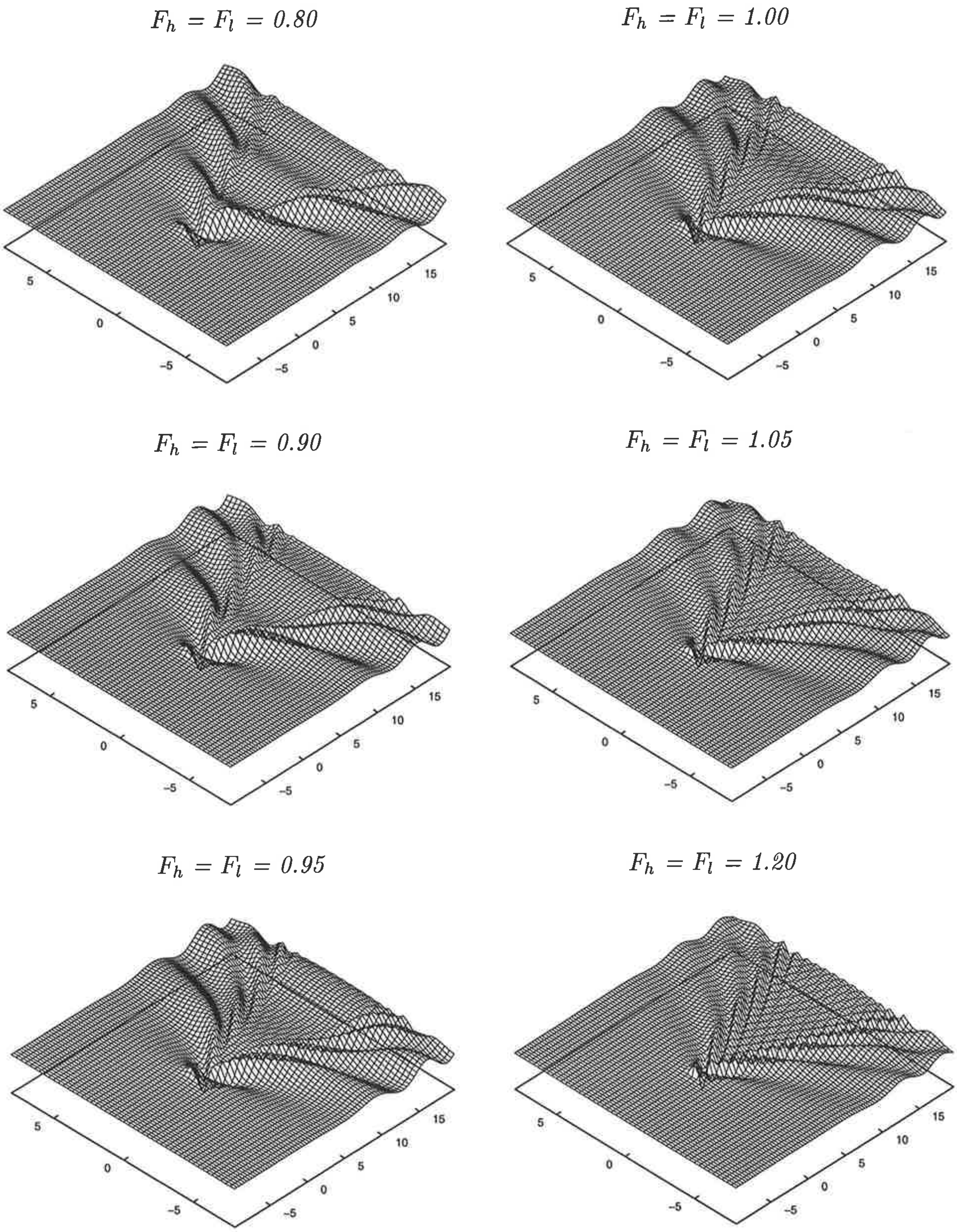
$F_h = F_l = 0.80$

$F_h = F_l = 1.00$

$F_h = F_l = 0.90$

$F_h = F_l = 1.05$

$F_h = F_l = 0.95$

$F_h = F_l = 1.20$

Figure 7.2: The wake broadens as the fluid-depth-based Froude number is increased to the critical value of one, before narrowing as the Froude number is increased further. For supercritical flows, only the divergent waves exist.

of significant value in establishing the reliability of the method, since there exist linear theories for the wave resistance about spheres in both semi-infinite fluids and fluids of finite depth.

7.4.1 THE LINEAR THEORY FOR A FLUID OF FINITE DEPTH

In a paper which is of greater relevance to the current topic, Havelock [16] derived an expression for the wave resistance of a submerged dipole in a fluid of finite depth and suggested that the resulting curves would have characteristics similar to those for a symmetric surface pressure distribution, as discussed above. That is, each curve would have a region of increased wave resistance, relative to the semi-infinite-fluid case. The process of derivation was correct, but the final result contained an error, which he later made mention of in [18] when he derived by an alternative method a second expression which is consistent with the corrected earlier result.

According to the theory, for a sphere of radius a submerged at depth f in a fluid of depth h with stream speed U, the wave resistance can be determined from (Havelock [16])

$$R = 4\pi\rho U^2 a^6 k \int_{\theta_0}^{\frac{\pi}{2}} \frac{k_\theta^3 e^{-2k_\theta h} \cosh^2(k_\theta(h-f))\ (1+\tanh k_\theta h)^2}{1 - kh\sec^2\theta\,\mathrm{sech}^2 k_\theta h} \cos\theta\, d\theta\ , \tag{7.3}$$

where the lower bound of the integration is

$$\theta_0 = \arccos\sqrt{kh} \tag{7.4}$$

and k_θ is the root of

$$k_\theta = k\sec^2\theta\,\tanh k_\theta h\ , \tag{7.5}$$

and all other symbols have their usual meanings. Since k represents the wave number for waves propagating in the direction of motion in a semi-infinite fluid, k_θ is the wave number for those propagating at an angle of θ relative to the centre-line in a fluid of depth h.

For the current purposes, the wave resistance is expressed better as

$$\frac{R}{\frac{4}{3}\pi\rho g a^3} = 3\left(\tfrac{a}{f}\right)^3 \int_{\theta_0}^{\frac{\pi}{2}} \frac{F_\theta^{-6}\cosh^2((\frac{h}{f}-1)F_\theta^{-2})}{\cosh^2(\frac{h}{f}F_\theta^{-2}) - \frac{h}{f}F^{-2}\sec^2\theta} \cos\theta\, d\theta\ , \tag{7.6}$$

where $F = U/\sqrt{gf} = 1/\sqrt{kf}$ is the Froude number based upon the depth of the sphere and F_θ is the root of

$$F_\theta^{-2} = F^{-2}\sec^2\theta\tanh\frac{h}{f}F_\theta^{-2}\ . \tag{7.7}$$

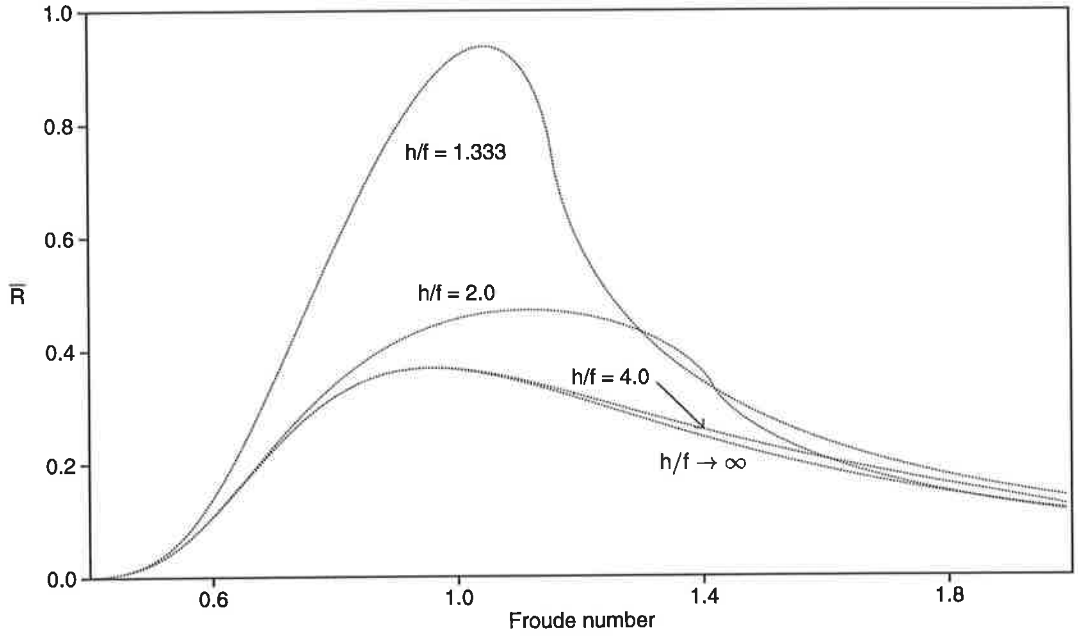

Figure 7.3: Dimensionless wave resistance as predicted by the linear theory for a sphere submerged in a finite-depth fluid.

In this form, it becomes clear that the integral is dependent only upon the choices of F and the dimensionless fluid-depth parameter h/f. (For clarity, in the following the term "Froude number" will refer to the body-depth-based Froude number F, and is to be distinguished from the fluid-depth-based Froude number F_h.)

Further, scaling with respect to $(a/f)^3$ defines the dimensionless quantity

$$\overline{R} = \frac{R}{\left(\frac{4}{3}\pi\rho g a^3\right)\left(\frac{a}{f}\right)^3}, \tag{7.8}$$

which has the desirable property that for each choice of h/f, there exists a single curve which represents all values of the radius-to-depth ratio.

Reasonable care is required when numerically evaluating the integral, since as θ tends to $\pi/2$, both the numerator and denominator of the integrand grow infinitely large, while the quotient vanishes. Figure 7.3 shows curves produced by equations (7.6) and (7.8) for fluid-to-body-depth ratios of 1.333, 2.0, and 4.0. They correspond to the sphere being positioned above the fluid bed by factors of one quarter, one half, and three quarters of the fluid depth respectively. The curve $h/f \to \infty$ represents the limit as the fluid depth becomes infinite, and is produced from the linear theory for a sphere in a semi-infinite fluid (as given by Havelock [16]).

The cases which provide the greatest contrast with the semi-infinite fluid case are of course those for which the sphere is located near the bed; that is, for values of h/f near one. As the sphere nears the surface, the curves rapidly approach the semi-infinite fluid case, so much so that there is no observable difference for values of h/f in excess of 10. For values of h/f greater than approximately 3, the curves follow closely the major hump of the semi-infinite fluid case, but then grow marginally by comparison, before again approaching the semi-infinite-fluid curve. This is analogous to the "second maximum" described by Havelock for his surface pressure disturbance, and occurs near a fluid-depth-based Froude number of one. For smaller values of h/f these two effects are combined, and lead to the relatively large wave-resistance curves shown. Thus, it is clear that over the range of Froude numbers considered, the presence of a bed increases the wave resistance of the body, the effect being most noticeable near the (critical) fluid-depth-based Froude number of one.

7.4.2 RESULTS OF NUMERICAL COMPUTATIONS

In the following, attention will be directed to the finite-depth case where the body is submerged midway between the free surface and the fluid bed, that is, $h/f = 2$, for which according to the linear theory, the effect of the bed can be to increase the wave resistance by as much as 50% relative to the semi-infinite fluid case. For this case, the critical fluid-depth-based Froude number of one corresponds to $F = \sqrt{2}$. Accordingly, numerical computations will be made for flows with F in the interval $[0.5, 2.0]$, for both the semi-infinite-fluid case and the finite-depth case.

7.4.2.1 SPHERES IN A SEMI-INFINITE FLUID

The domain is represented in much the same way as for that above the spheroid in the previous chapter, except that the various dimensions are changed. Again, and without loss of generality, both the free-stream speed and the gravitational acceleration are set to unity, and lateral symmetry is assumed. The free-surface singularity grid has 91 rows and 25 columns. The length of the domain is $35/F^2$, with one third of the domain laying upstream, and two thirds downstream. This choice of domain length ensures that, for any fixed choice of a/f, the domain remains in fixed proportion to the size of the body as the Froude number is varied. It is also chosen so that the waves are reasonably represented over the range of Froude numbers, in terms of both the number of nodes per wavelength and the number of waves captured by the domain. The half-width of the domain is one quarter of its length, so that the waves meet the side boundaries near the downstream end, and the widthwise grid spacing is similar to that in the flow direction. The singularities are set at a height that is one thirtieth of the domain length, which is equivalent to an offset height ratio of 3 (when based upon the lengthwise grid spacing). Free surface nodes originally lie on the plane $z = 0$ directly beneath each of the free-surface singularities, except for the upstream and downstream rows. The hemisphere is represented in a manner that is analogous to the spheroid, except that the radius of the inner sphere on which the singularities lie is chosen to be one half that of the body.

As part of the exercise, it was a simple matter to generate the results for comparatively large spheres, and these are included in Figure 7.4 for later comparison with the finite-fluid results. The figure shows the numerical results in comparison to the linear theory. The results for a sphere of radius-to-depth ratio 0.05 are graphically indistinguishable from the universal curve predicted by the linear theory, which is shown by the dotted curve. In fact, the relative error is less than 2% for all the choices of Froude number considered. The solid curves represent spheres with radius-to-depth ratios of 0.2, 0.4 and 0.5. Once again, for large disturbances, there exist some Froude numbers for which converged results could not be obtained. Figure 7.5 shows the associated lift force for the same cases. Note that the lift in made dimensionless by scaling with the same factor as that for the wave resistance, and that the force does not include the hydrostatic component that is due to the displacement of fluid by the sphere.

As the radius-to-depth ratio is increased, the effects of nonlinearity become more noticeable. The general trend is to increase the wave resistance for Froude numbers less than approximately 0.9, and to decrease the wave resistance for Froude numbers greater than this. The proportional change (relative to the linear theory predictions) is greatest for small Froude numbers. For the vertical force, the nonlinear effect tends to decrease the lift for Froude numbers less than approximately 1.0, and to increase the lift for Froude numbers greater than this.

The results of the investigation indicate that the current method is capable of accurately producing results that are consistent with the linear theory for a sphere in a semi-infinite fluid, over the range of Froude numbers $[0.5, 2.0]$.

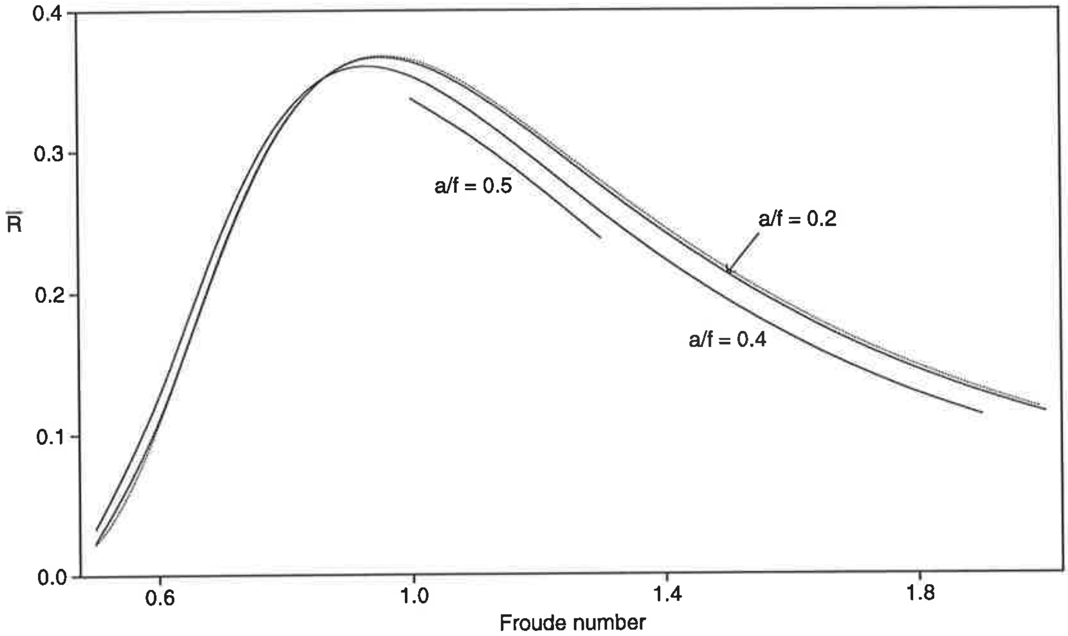

Figure 7.4: Dimensionless wave resistance as determined by the current method for spheres of radius-to-depth ratios of 0.2, 0.4, and 0.5. The dotted line represents the linear theory, from which the results for $a/f = 0.05$ are graphically indistinguishable.

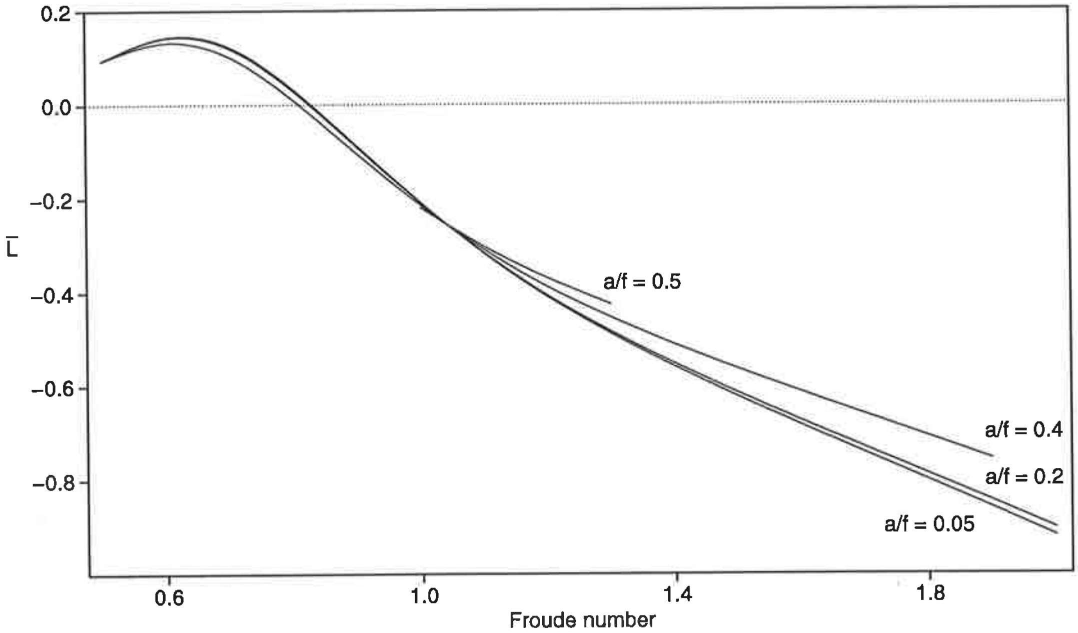

Figure 7.5: Dimensionless lift as determined by the current method for spheres of radius-to-depth ratios of 0.05, 0.2, 0.4, and 0.5.

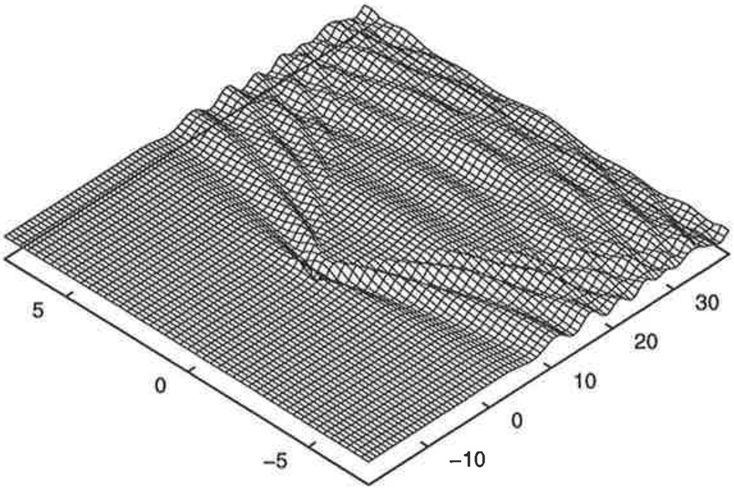

Figure 7.6: For flows with a Froude number near the critical value, waves are reflected from the sides of the computational domain. This problem may be reduced by adopting a wider computational domain, but this is currently computationally prohibitive.

7.4.2.2 THE FINITE-DEPTH CASE $h/f = 2$

A bed is introduced, at a depth such that the sphere is located midway between the bed and surface; that is, with $h/f = 2$. The same representations of the free surface, body and potential are implemented, the exception being that each singularity has an associated image, the combination of which satisfies the Neumann boundary condition on the bed exactly. For comparison to the semi-infinite fluid case, the same cases of radius-to-depth ratio and Froude number as above are considered.

An initial investigation, for a sphere of radius-to-depth ratio 0.05, indicated there was some disagreement with the linear theory for Froude numbers near the critical value, for which $F = \sqrt{2}$. Further investigation revealed that this was due to reflection of the waves at the sides of the domain of representation, since a significant amount of energy was contained in the waves found there. Consequently, the wave pattern became corrupted and the force results were unreliable. This may be surmountable by extending the width of the domain, but with the current computing capabilities, is a resource and time-consuming task. Figure 7.6 shows the reflection of such waves for one particular case.

An associated difficulty is that the wavelength of waves with small angle of propagation becomes large (tending towards infinity), and as such it is impossible to capture these waves. This is not of such concern, since these waves contain relatively little energy, and therefore the force computations are only affected slightly.

The problem of reflected waves only occurs for cases in which the wedge is widened significantly. Since there is rapid growth in the wedge angle as the critical Froude number is approached, compared with gradual reduction as the Froude number is further increased, the flows can be determined accurately for most subcritical flows. For this reason, nonlinear results are given only for Froude numbers less than the critical Froude number, the understanding being that the results are less reliable as the critical Froude number is approached, but that an indication of reliability can be drawn from the comparison of the linear-theory curve and the small-radius sphere $a/f = 0.05$.

Figure 7.7 shows the wave resistance as determined by the current method for the cases considered, and for which a converged solution could be obtained. The appropriate linear theory curve (that for $h/f = 2$) is shown dotted, and it can be seen that there is strong agreement between this curve and the numerical results obtained by the current method for the case $a/f = 0.05$. There is however some small discrepancy for Froude numbers in the range $[1.1, 1.4]$, and this should be taken into account when interpreting the results in this range for larger spheres. Again the effect of increased sphere radius is to increase the wave resistance for low Froude numbers (less than approximately 1.0), and to decrease it for larger Froude numbers. For large spheres, this effect can be quite considerable. For example, there is a reduction in wave resistance of approximately 25% for spheres with $a/f = 0.6$ at a Froude number of 1.4. The linear theory for spheres in a semi-infinite fluid is represented by the dashed curve, and is included here for the purposes of comparison also.

Similarly, the vertical force experienced by the sphere is shown in Figure 7.8. The tendency of increased radius-to-depth ratio is to decrease the lift for Froude numbers less than approximately 1.1, and to increase it thereafter.

7.5 SPHEROIDS

The linear theory for the wave resistance of a spheroid in a semi-infinite fluid was stated as equation (6.1) on page 109 in Chapter 6. Havelock did not determine a linear theory for the corresponding finite-depth fluid problem, and the author is not aware of any existing

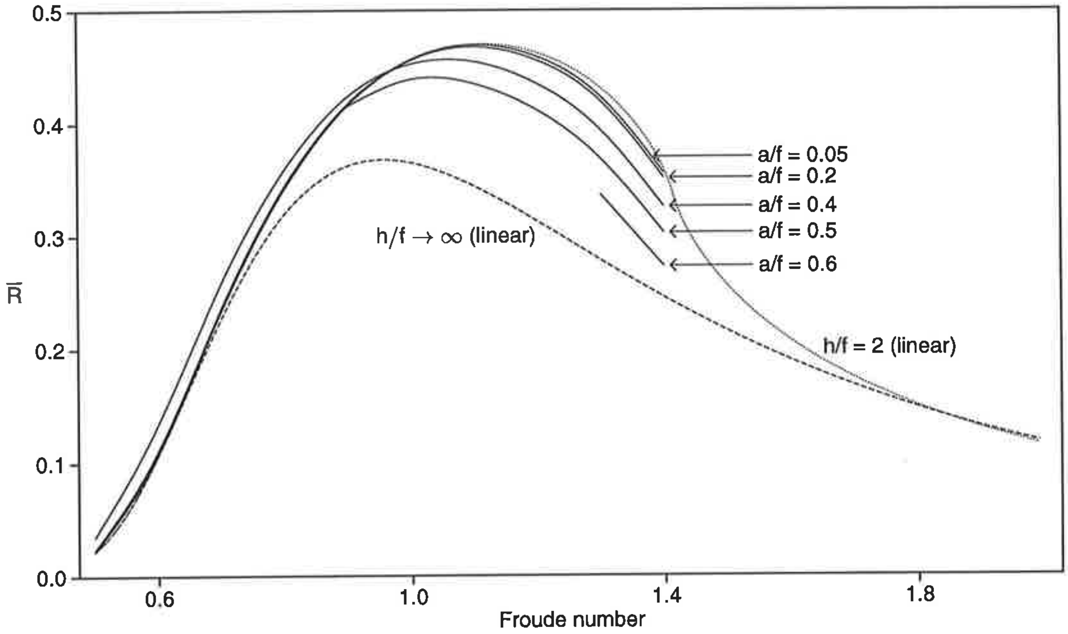

Figure 7.7: Dimensionless wave resistance for subcritical flows about spheres in a fluid of finite depth, with $h/f = 2$. The dotted line represents the appropriate linear theory — that for a sphere in a semi-infinite fluid is also included for comparison (dashed).

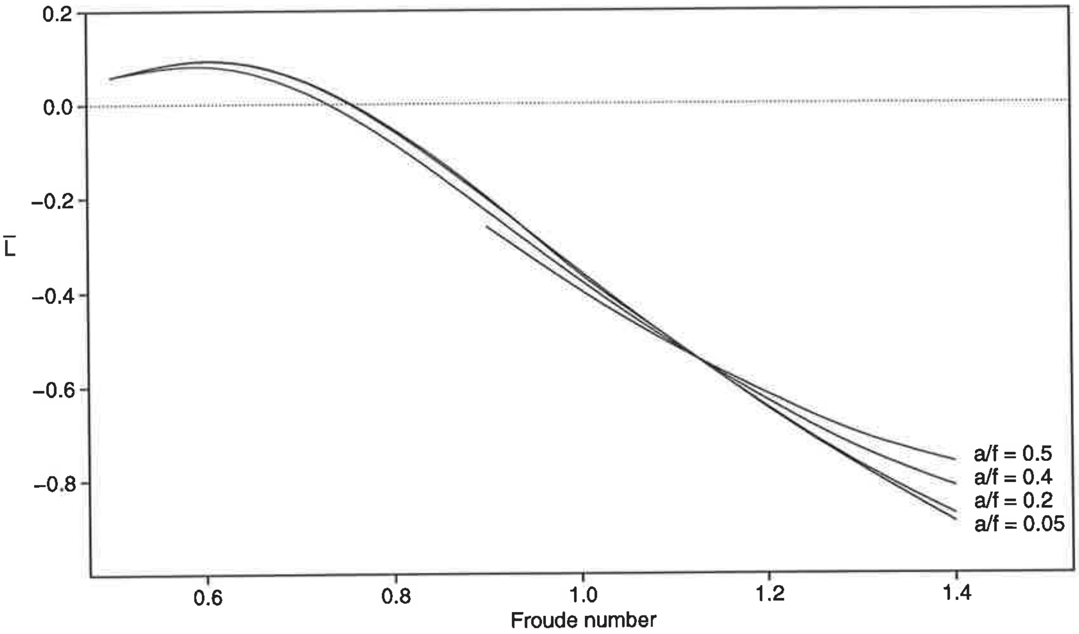

Figure 7.8: Dimensionless lift as determined by the current method for spheres in a fluid of finite depth with $h/f = 2$.

result. However, it is felt that based upon the strength of consistency with the linear theory for the semi-infinite fluid case (established in Chapter 6 and to be revisited here), coupled with the evidence indicating the ability to solve accurately subcritical flows about spheres in a finite-depth fluid, it is justified to investigate finite-depth effects for spheroids.

7.5.1 FORCES ON A SPHEROID

The program was exercised for a range of values of d/f, for both the semi-infinite fluid case ($h/f \to \infty$) and the finite-depth fluid case $h/f = 2$. Again, attention was restricted to subcritical flows, the decision being based upon the experience gained from investigating finite-depth flows about spheres. The results of wave-resistance calculations are shown in Figure 7.9. The dotted lines represent the linear theory for the semi-infinite fluid case. The dashed lines represent the numerical results obtained for spheroids of various sizes in a semi-infinite fluid, and the solid curves are the corresponding results for cases with $h/f = 2$.

Note that for spheroids, the dimensionless wave resistance is redefined to be

$$\overline{R} = \frac{R}{\frac{1}{6}\pi \rho g l d^2 \left(d/f\right)^3} \tag{7.9}$$

in a manner that is analogous to that for spheres. Although this does not give curves independent of the spheroid's diameter-to-depth ratio, it does allow curves for a wide range of d/f values to be plotted on the same set of axes.

Similarly, the vertical force experienced by the spheroid is shown in Figure 7.10. The lift has been scaled with respect to the same factor as the wave-resistance.

Considering the wave-resistance curves, for the spheroid with $d/f = 0.10$ in a semi-infinite fluid, the results are in close agreement throughout with the linear theory, with the maximum relative error being less than 2%. It is clear that the effect (in a semi-infinite fluid) of increasing diameter-to-depth ratio is to increase the wave resistance at low Froude number, but to decrease it at high Froude number. The Froude number at which the transition occurs depends upon the value of d/f, but typically increases as d/f increases. By comparison, the effect of a finite-depth fluid is to increase the wave resistance (in some instances considerably) throughout the range of (subcritical) Froude numbers considered. The general manner in which this happens is consistent with what could have been predicted based upon the results produced by Havelock in the papers

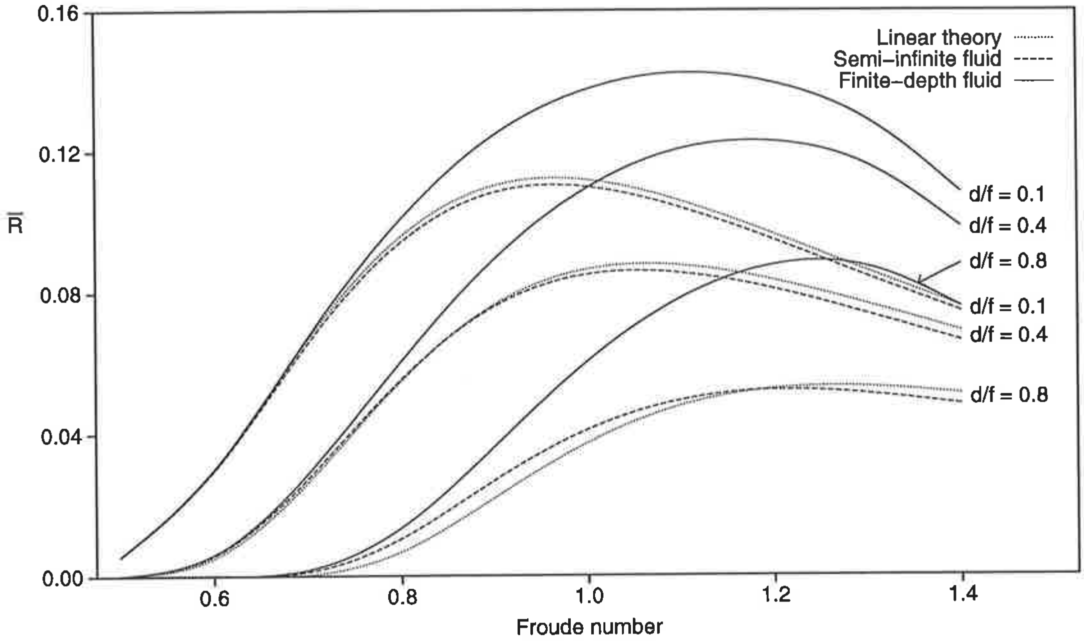

Figure 7.9: Dimensionless wave resistance for spheroids. The dotted lines represent the linear theory for the semi-infinite-fluid case, and the dashed lines are the corresponding results from the current method. The solid curves are for the same cases except in a finite-depth fluid, with $h/f = 2$.

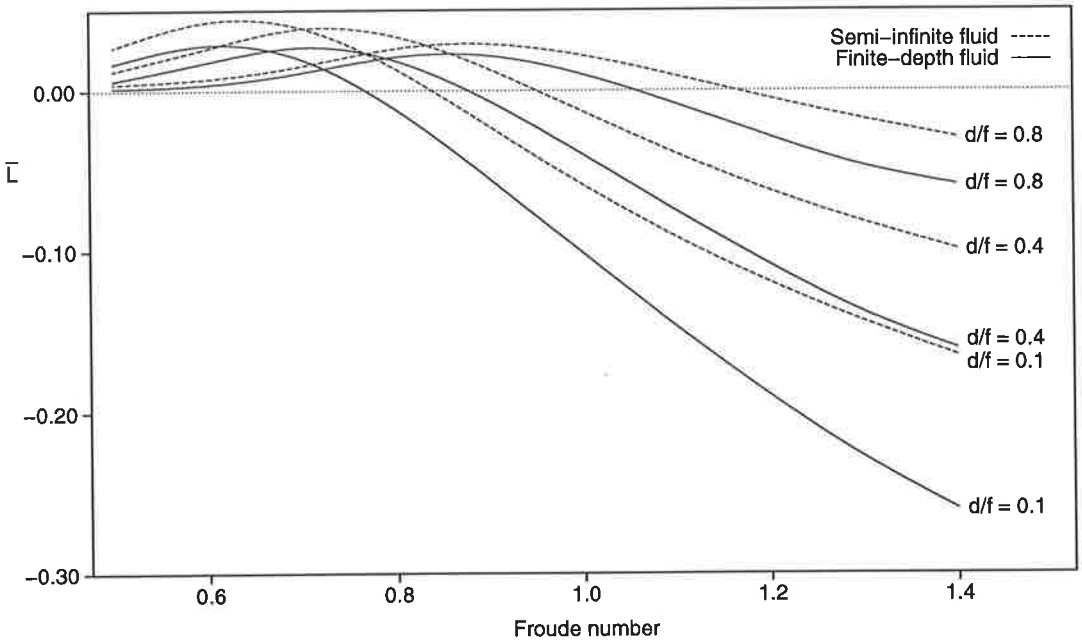

Figure 7.10: Vertical force acting on the spheroids for the same cases as described above.

already mentioned, coupled with the results of the nonlinear numerical computations for the sphere in the previous section.

For the vertical force, the effect of a finite-depth fluid is to decrease the lift for all diameter-to-depth ratios considered throughout the range of Froude numbers $[0.5, 1.4]$.

7.6 CONCLUSION

Various theories predict interesting behaviour of flows in fluids of finite depth. One can anticipate that the wake can be affected greatly, with the angle of the wedge within which the wake is contained growing to a maximum of 180° at the critical fluid-depth-based Froude number of one. Beyond this, the transverse waves vanish. One could expect that the wave resistance would be increased relative to the semi-infinite fluid case over a range of Froude numbers, the effect being most noticeable near the critical Froude number. For large fluid-depth-based Froude numbers, the wave resistance is diminished.

The current method performs well in accurately reproducing such flows. Qualitative consistency with the wake characteristics predicted by the linear theory is observed. The method does however suffer from a difficulty associated with reflection of wave energy at the sides of the computational domain, but this is a computational difficulty that may be overcome by extension of the domain boundaries. Given current computing capabilities, this is a resource-consuming task.

For situations in which these reflected waves occur to a lesser extent (that is, for subcritical flows), the results are quantitatively consistent with that which is to be expected from the linear theory for a sphere. Based upon this investigation, it was meaningful to investigate the effects of finite-depth fluids for spheroids, for which the author is not aware of any existing linear theory.

CONCLUSION

A method for the solution of steady-state nonlinear free-surface flow problems has been presented. The method uses a distribution of discrete sources located external to the fluid domain to represent the potential. An important advantage of desingularisation, as was seen to be the case in Chapter 2, is that it provides a smoother representation of the potential, and therefore provides better satisfaction of the boundary conditions over the free surface and body. Another advantage is that the influences of the singularities on the boundary conditions are never singular, and as such are easier to formulate. Sources are shown to provide accurate representation, and have the added benefit that their associated potential and derivatives are simple to evaluate exactly, thus removing the need for quadrature rules and other approximate methods.

The effect on accuracy of resolution of the free surface has been discussed. Naturally, the steeper the wave, the more collocation points that are needed to represent it. Also discussed was the effect of the location of the singularities, relative to the collocation points. The conclusion is that sources are best placed along normals to collocation points, since it is in these locations that the greatest accuracy is obtained. In the context of an iterative procedure, however, it may be desirable to position them on a plane directly above the collocation points. A procedure for determining the offset for the singularities and the resolution of the free surface has been presented.

Several options for the formulation of the radiation condition were considered. The preference is for one that states that the vertical component of velocity decays exponentially in the upstream direction. Correct selection of the particular waveless solution is reasonably independent of the location of implementation of the radiation condition, provided that the two points at which it is enforced are not separated by an integer multiple of a quarter wavelength, or a distance near one of these.

In general, it was found that the effect of domain truncation was the dominant cause of error. Increasing the domain length will increase the accuracy, but at an increased computational cost, in terms of both the size of the system of simultaneous equations that is to be solved, and the number of iterations required within the iterative procedure. Indeed, due to the nonlinear effect of shortening wavelength, an extended domain may destroy convergence.

Several alternatives for the formulation of the free-surface boundary condition were considered and evaluated for speed and reliability. The preference is for a formulation that exhibits a quadratic rate of convergence to the desired solution. The formulation requires that derivatives of the potential up to third order are known.

Coupled with the boundary-condition formulation were options by which the new free-surface approximation could be determined. The only appropriate choice was for one based upon the dynamic free-surface boundary condition.

The effects of shifting singularities between iterations was also considered. In general, this is an expensive computational practice, since either the number of iterations required to achieve convergence, or the size of the system of simultaneous equations, will increase as a result. For small amplitude disturbances to the free surface, and indeed for most free-surface flows, it is unnecessary. All of the applications shown in this thesis used singularities held fixed on a plane throughout the solution process.

Appropriate test conditions for convergence, based upon the free-surface boundary conditions, were stated in a dimensionless form, so that they are suitable irrespective of the choices made for other parameters of scale such as stream speed and gravitational acceleration.

Note that the appendix gives a detailed description of the formulation of the solution method, including the iterative algorithm, the condition that is to be enforced on the free-surface approximations, and the manner in which the next approximation is to be determined.

The method was subsequently applied to flows around various submerged bodies. The first application was for a circular cylinder. The wave resistance was compared to that predicted by the first-order and second-order linear theories, and for sufficiently small cylinders, consistency was found. The vertical force experienced by the cylinder was also determined. The nonlinear effects produced by larger cylinders were discussed. Solutions with large amplitude waves were sought, and some with maximum crest heights of up to 86% of the stagnation height were found. Circulation about the cylinder was then introduced, and the effects of this upon the wave-making were investigated. The conclusion is that circulation has an ability to reduce the waves over a greater range than is predicted by the linear theory. The corresponding reduction in wave resistance was also noted. Flows about two cylinders in tandem were then investigated. The linear theory predicts that there are discrete choices of depth and separation such that both cylinders are free of horizontal force, and the combination does not produce waves downstream. The effect of increasing cylinder radius is that the phenomenon occurs at greater depths and separations than is predicted by the linear theory. To within the accuracy of the calculations, the combinations still occur at discrete locations, rather than existing over a continuous range of values.

The 1:5 prolate spheroid was then considered. The variation in pattern of the wake with changes in speed was briefly demonstrated, and other qualities of the wake were observed. The wave resistance was compared to the linear theory, and again good agreement was found for spheroids of small enough size. The lift force was also investigated. The effects of increasing spheroid size were demonstrated. The numerical results were also compared with those produced by other methods, and a general agreement was found. Some interesting results for which the surface disturbance is considerable and the spheroid is shallowly submerged were then presented.

Finally, flows about spheres and spheroids in a fluid of finite depth were considered. The wake was shown to widen near the critical fluid-depth-based Froude number, and to narrow as the fluid-depth-based Froude number was increased further. The forces were calculated and comparisons were made to the semi-infinite fluid results. By comparing with the linear theory, the results were found to be unreliable for cases in which the wake had widened considerably, due to reflection of wave energy at the sides of the computational domain. As a consequence, finite-depth fluid effects were only investigated for subcritical Froude numbers, for which the results are accurate. Again, the effects of increased body size were discussed.

Naturally, there are ways in which this work can be extended. Surface-piercing flows, such as those produced by ships, are an important application. The difficulty associated with such flows is that they often produce a splash near the bow, or a breaking wave near the stern. It would, however, be of value to investigate further the possibility of capturing surface-piercing flows for which the region of overturning fluid is not too large.

Another refinement of the method would be to introduce a technique, such as multipole acceleration, which reduces both the memory and cpu requirements. As was noted earlier, storage of a large matrix quickly becomes a limiting factor on the resolution and length of domain, and hence the accuracy that can be achieved by the method. Increasing the resolution by a factor of n results in an increase in matrix size by a factor of n^4, and an associated increase of cpu requirements by a factor of n^6. Multipole techniques have the possibility to reduce both these to an increase by a factor of only n^2.

Another possibility of expansion would be to introduce time-dependency, so that unsteady problems could be considered. The details of the solution method would be considerably different, but the manner in which the potential and free surface are represented could remain largely the same.

In summary then, a method of solution for steady nonlinear free-surface flows about submerged bodies has been presented. After careful design, experimentation and verification, and in a variety of applications, the method has been shown to be fast, reliable and accurate.

APPENDIX

THE ITERATIVE PROCEDURE REVISITED

A more descriptive derivation of the free-surface boundary condition, which involves the linearisation of the perturbation potential, is given. Subsequently, an algorithm for the iterative procedure is stated. Finally, the terms in the free-surface boundary condition are discussed in greater detail.

A.1 FORMULATION OF THE FREE-SURFACE BOUNDARY CONDITION

An overview of the free-surface boundary condition and iterative procedure was given in Chapter 4. The purpose of the current section is to give greater clarity to the formulation that was the preferred method as determined by the analysis of that chapter.

Consistent with the notation used in that chapter, the free surface solution is denoted by $z = \zeta^*(x, y)$, and the solution potential by $\phi = \phi^*(x, y, z)$. However, due to the lengthy nature of some of the mathematical statements which are to follow, a couple of abbreviations to the notation are made. Specifically, the material derivative of pressure $\frac{Dp}{Dt}$ will be replaced by E, and the operator $\frac{\partial}{\partial\zeta}$ will be replaced by a subscript z. So, for example, the expression $\frac{\partial}{\partial\zeta}\frac{Dp}{Dt}$ will be expressed more concisely as E_z.

The pair of equations that are to be satisfied on the free surface are now

$$E(\phi^*, \zeta^*) = 0 \qquad \text{and} \tag{A.1}$$

$$p(\phi^*, \zeta^*) \;=\; 0\,. \tag{A.2}$$

The free surface ζ^* is approximated closely by ζ^0, with the small error in the approximation being ζ^1. That is, $\zeta^* = \zeta^0 + \zeta^1$.

Using a Taylor series expansion in ζ for $E(\phi^*, \zeta^*)$ about the approximate free surface ζ^0 gives

$$0 = E(\phi^*, \zeta^*) = E(\phi^*, \zeta^0) + \zeta^1 E_z(\phi^*, \zeta^0) + \mathrm{O}((\zeta^1)^2)\,, \tag{A.3}$$

which can be rearranged to yield

$$\zeta^1 = -E(\phi^*, \zeta^0)/E_z(\phi^*, \zeta^0) + \mathrm{O}((\zeta^1)^2)\,. \tag{A.4}$$

Similarly, the pressure on the free surface can be approximated by

$$0 = p(\phi^*, \zeta^*) = p(\phi^*, \zeta^0) + \zeta^1 p_z(\phi^*, \zeta^0) + \mathrm{O}((\zeta^1)^2)\,, \tag{A.5}$$

which can also be rearranged to give

$$\zeta^1 = -p(\phi^*, \zeta^0)/p_z(\phi^*, \zeta^0) + \mathrm{O}((\zeta^1)^2)\,. \tag{A.6}$$

Equating equations (A.4) and (A.6) and rearranging yields

$$E(\phi^*, \zeta^0) p_z(\phi^*, \zeta^0) - E_z(\phi^*, \zeta^0) p(\phi^*, \zeta^0) = \mathrm{O}((\zeta^1)^2)\,, \tag{A.7}$$

which is a boundary condition that is satisfied on ζ^0, the approximation to the free surface.

A.2 LINEARISATION IN THE PERTURBATION POTENTIAL

Suppose the potential ϕ is closely approximated by ϕ^0 with an error of ϕ^1. That is, $\phi = \phi^0 + \phi^1$. Then, expanding $E(\phi^*, \zeta^0)$ about ϕ^0 in powers of ϕ^1 indicates

$$E(\phi^*, \zeta^0) = E(\phi^0 + \phi^1, \zeta^0) = E(\phi^0, \zeta^0) + E^1 + \mathrm{O}((\phi^1)^2)\,, \tag{A.8}$$

where E^1 contains all terms that are linearly dependent upon ϕ^1. Defining $E^0 = E(\phi^0, \zeta^0)$ (which contains all terms that are independent of ϕ^1) allows this to be written more succinctly as

$$E(\phi^*, \zeta^0) = E^0 + E^1 + \mathrm{O}((\phi^1)^2)\,. \tag{A.9}$$

Similarly, defining $p^0 = p(\phi^0, \zeta^0)$, and p^1 to contain all terms that vary linearly with ϕ^1, allows for $p(\phi^*, \zeta^0)$ to be expressed as

$$p(\phi^*, \zeta^0) = p^0 + p^1 + \mathrm{O}((\phi^1)^2)\ . \tag{A.10}$$

Thus, equation (A.7) can be re-expressed as

$$(E^0 + E^1)(p_z^0 + p_z^1) - (E_z^0 + E_z^1)(p^0 + p^1) = \mathrm{O}((\zeta^1)^2, (\phi^1)^2)\ . \tag{A.11}$$

Expanding and rearranging yields

$$E^0 p_z^0 - E_z^0 p^0 = -(E^0 p_z^1 - E_z^0 p^1 + E^1 p_z^0 - E_z^1 p^0) - (E^1 p_z^1 - E_z^1 p^1) + \mathrm{O}((\zeta^1)^2, (\phi^1)^2) \tag{A.12}$$

where the terms on the left hand side are independent of ϕ^1, and the terms within the first set of parentheses are linearly dependent upon it. Neglecting terms of order $\mathrm{O}((\zeta^1)^2, (\phi^1)^2)$ (which include both $E^1 p_z^1$ and $E_z^1 p^1$) yields the equation

$$E^0 p_z^0 - E_z^0 p^0 = -(E^0 p_z^1 - E_z^0 p^1 + E^1 p_z^0 - E_z^1 p^0) \tag{A.13}$$

which is a condition that is linear in the perturbation potential ϕ^1.

A.3 THE ITERATIVE ALGORITHM

The condition (A.13) forms the basis of an iterative procedure by which the solution potential and free surface can be determined. The appropriate algorithm is:

- Given an approximation $z = \zeta^0$ to the free surface, and some approximation $\phi = \phi^0$ to the solution potential, determine the perturbation potential ϕ^1 that satisfies the condition

  $$E^0 p_z^0 - E_z^0 p^0 = -(E^0 p_z^1 - E_z^0 p^1 + E^1 p_z^0 - E_z^1 p^0) \tag{A.14}$$

  on that surface.
- Set the new approximate potential to be

  $$\phi^0 \leftarrow \phi^0 + \phi^1\ . \tag{A.15}$$

- Using the new approximate potential, determine the perturbation to the free surface from

  $$\zeta^1 = -p^0 / p_z^0\ , \tag{A.16}$$

and set the new approximate surface to be

$$\zeta^0 \leftarrow \zeta^0 + \zeta^1 \; . \tag{A.17}$$

- If, on the new approximate surface,

$$\left|E^0\right| < \epsilon_E \qquad \text{and} \qquad \left|p^0\right| < \epsilon_p \; , \tag{A.18}$$

  where ϵ_E and ϵ_p are some desired tolerances, then ϕ^0 is a suitable approximation to the desired solution potential, and ζ^0 is a suitable approximation to the desired free surface.
- Otherwise, repeat the process.

The iterative procedure demonstrates a quadratic rate of convergence, since the truncation error of both the free-surface boundary condition (A.14) and the surface-update condition (A.16) are of order $\mathrm{O}((\zeta^1)^2, (\phi^1)^2)$, as can be seen from equations (A.12) and (A.6).

A.4 FORM OF BOUNDARY-CONDITION COMPONENTS

Although the free-surface boundary condition, surface-update procedure, and convergence criteria are succinctly stated in terms of their eight components (p^0, p^1, p^0_z, p^1_z, E^0, E^1, E^0_z and E^1_z), it is not immediately clear how these components are represented in terms of the potentials ϕ^0 and ϕ^1. The purpose of this section is to give such representations.

From the Bernoulli equation

$$p(\phi, \zeta) = \tfrac{1}{2}(U^2 - \nabla^2\phi) - g\zeta \; , \tag{A.19}$$

it follows, using the definition of p^0, that

$$p^0 = p(\phi^0, \zeta^0) = \tfrac{1}{2}(U^2 - \nabla^2\phi^0) - g\zeta^0 \; . \tag{A.20}$$

The expansion of $p(\phi^0 + \phi^1, \zeta^0)$ in powers of ϕ^1, namely

$$\begin{aligned} p(\phi^0 + \phi^1, \zeta^0) &= \tfrac{1}{2}(U^2 - \nabla^2(\phi^0 + \phi^1)) - g\zeta^0 \\ &= \tfrac{1}{2}(U^2 - \nabla^2\phi^0 - 2\underset{\sim}{\nabla}\phi^0.\underset{\sim}{\nabla}\phi^1 - \nabla^2\phi^1) - g\zeta^0 \\ &= p^0 - \underset{\sim}{\nabla}\phi^0.\underset{\sim}{\nabla}\phi^1 - \tfrac{1}{2}\nabla^2\phi^1 \; , \end{aligned} \tag{A.21}$$

makes it apparent that p^1, which contains all terms that vary linearly with ϕ^1, is

$$p^1 = -\underset{\sim}{\nabla}\phi^0.\underset{\sim}{\nabla}\phi^1 \; . \tag{A.22}$$

In a similar manner, expressions for the remaining six quantities can be found. In summary then, the components are:

$$\begin{align*}
p^0 &= \tfrac{1}{2}(U^2 - \nabla^2\phi^0) - g\zeta^0 \tag{A.23}\\
p^1 &= -\underset{\sim}{\nabla}\phi^0.\underset{\sim}{\nabla}\phi^1 \tag{A.24}\\
p^0_z &= -\underset{\sim}{\nabla}\phi^0.\underset{\sim}{\nabla}\phi^0_z - g \tag{A.25}\\
p^1_z &= -\underset{\sim}{\nabla}\phi^0.\underset{\sim}{\nabla}\phi^1_z - \underset{\sim}{\nabla}\phi^1.\underset{\sim}{\nabla}\phi^0_z \tag{A.26}
\end{align*}$$

$$\begin{align*}
E^0 &= \underset{\sim}{\nabla}\phi^0.\underset{\sim}{\nabla}p^0 \tag{A.27}\\
&= -(\phi^0_x\underset{\sim}{\nabla}\phi^0.\underset{\sim}{\nabla}\phi^0_x + \phi^0_y\underset{\sim}{\nabla}\phi^0.\underset{\sim}{\nabla}\phi^0_y + \phi^0_z\underset{\sim}{\nabla}\phi^0.\underset{\sim}{\nabla}\phi^0_z + \phi^0_z g) \tag{A.28}
\end{align*}$$

$$\begin{align*}
E^1 &= \underset{\sim}{\nabla}\phi^0.\underset{\sim}{\nabla}p^1 + \underset{\sim}{\nabla}\phi^1.\underset{\sim}{\nabla}p^0 \tag{A.29}\\
&= -(\phi^0_x\underset{\sim}{\nabla}\phi^0.\underset{\sim}{\nabla}\phi^1_x + \phi^0_y\underset{\sim}{\nabla}\phi^0.\underset{\sim}{\nabla}\phi^1_y + \phi^0_z\underset{\sim}{\nabla}\phi^0.\underset{\sim}{\nabla}\phi^1_z\\
&\quad + \phi^0_x\underset{\sim}{\nabla}\phi^1.\underset{\sim}{\nabla}\phi^0_x + \phi^0_y\underset{\sim}{\nabla}\phi^1.\underset{\sim}{\nabla}\phi^0_y + \phi^0_z\underset{\sim}{\nabla}\phi^1.\underset{\sim}{\nabla}\phi^0_z\\
&\quad + \phi^1_x\underset{\sim}{\nabla}\phi^0.\underset{\sim}{\nabla}\phi^0_x + \phi^1_y\underset{\sim}{\nabla}\phi^0.\underset{\sim}{\nabla}\phi^0_y + \phi^1_z\underset{\sim}{\nabla}\phi^0.\underset{\sim}{\nabla}\phi^0_z\\
&\quad + \phi^1_z g) \tag{A.30}
\end{align*}$$

$$\begin{align*}
E^0_z &= \underset{\sim}{\nabla}\phi^0.\underset{\sim}{\nabla}p^0_z + \underset{\sim}{\nabla}\phi^0_z.\underset{\sim}{\nabla}p^0 \tag{A.31}\\
&= -(\phi^0_x\underset{\sim}{\nabla}\phi^0.\underset{\sim}{\nabla}\phi^0_{xz} + \phi^0_y\underset{\sim}{\nabla}\phi^0.\underset{\sim}{\nabla}\phi^0_{yz} + \phi^0_z\underset{\sim}{\nabla}\phi^0.\underset{\sim}{\nabla}\phi^0_{zz}\\
&\quad + \phi^0_x\underset{\sim}{\nabla}\phi^0_z.\underset{\sim}{\nabla}\phi^0_x + \phi^0_y\underset{\sim}{\nabla}\phi^0_z.\underset{\sim}{\nabla}\phi^0_y + \phi^0_z\underset{\sim}{\nabla}\phi^0_z.\underset{\sim}{\nabla}\phi^0_z\\
&\quad + \phi^0_{xz}\underset{\sim}{\nabla}\phi^0.\underset{\sim}{\nabla}\phi^0_x + \phi^0_{yz}\underset{\sim}{\nabla}\phi^0.\underset{\sim}{\nabla}\phi^0_y + \phi^0_{zz}\underset{\sim}{\nabla}\phi^0.\underset{\sim}{\nabla}\phi^0_z\\
&\quad + \phi^0_{zz} g) \tag{A.32}
\end{align*}$$

$$\begin{align*}
E^1_z &= \underset{\sim}{\nabla}\phi^0.\underset{\sim}{\nabla}p^1_z + \underset{\sim}{\nabla}\phi^0_z.\underset{\sim}{\nabla}p^1 + \underset{\sim}{\nabla}\phi^1.\underset{\sim}{\nabla}p^0_z + \underset{\sim}{\nabla}\phi^1_z.\underset{\sim}{\nabla}p^0 \tag{A.33}\\
&= -(\phi^0_x\underset{\sim}{\nabla}\phi^0.\underset{\sim}{\nabla}\phi^1_{xz} + \phi^0_y\underset{\sim}{\nabla}\phi^0.\underset{\sim}{\nabla}\phi^1_{yz} + \phi^0_z\underset{\sim}{\nabla}\phi^0.\underset{\sim}{\nabla}\phi^1_{zz}\\
&\quad + \phi^0_x\underset{\sim}{\nabla}\phi^0_z.\underset{\sim}{\nabla}\phi^1_x + \phi^0_y\underset{\sim}{\nabla}\phi^0_z.\underset{\sim}{\nabla}\phi^1_y + \phi^0_z\underset{\sim}{\nabla}\phi^0_z.\underset{\sim}{\nabla}\phi^1_z\\
&\quad + \phi^0_{xz}\underset{\sim}{\nabla}\phi^0.\underset{\sim}{\nabla}\phi^1_x + \phi^0_{yz}\underset{\sim}{\nabla}\phi^0.\underset{\sim}{\nabla}\phi^1_y + \phi^0_{zz}\underset{\sim}{\nabla}\phi^0.\underset{\sim}{\nabla}\phi^1_z\\
&\quad + \phi^0_x\underset{\sim}{\nabla}\phi^1.\underset{\sim}{\nabla}\phi^0_{xz} + \phi^0_y\underset{\sim}{\nabla}\phi^1.\underset{\sim}{\nabla}\phi^0_{yz} + \phi^0_z\underset{\sim}{\nabla}\phi^1.\underset{\sim}{\nabla}\phi^0_{zz}\\
&\quad + \phi^0_x\underset{\sim}{\nabla}\phi^1_z.\underset{\sim}{\nabla}\phi^0_x + \phi^0_y\underset{\sim}{\nabla}\phi^1_z.\underset{\sim}{\nabla}\phi^0_y + \phi^0_z\underset{\sim}{\nabla}\phi^1_z.\underset{\sim}{\nabla}\phi^0_z
\end{align*}$$

$$\begin{aligned}
&+ \phi^0_{xz}\utilde{\nabla}\phi^1.\utilde{\nabla}\phi^0_x + \phi^0_{yz}\utilde{\nabla}\phi^1.\utilde{\nabla}\phi^0_y + \phi^0_{zz}\utilde{\nabla}\phi^1.\utilde{\nabla}\phi^0_z \\
&+ \phi^1_x\utilde{\nabla}\phi^0.\utilde{\nabla}\phi^0_{xz} + \phi^1_y\utilde{\nabla}\phi^0.\utilde{\nabla}\phi^0_{yz} + \phi^1_z\utilde{\nabla}\phi^0.\utilde{\nabla}\phi^0_{zz} \\
&+ \phi^1_x\utilde{\nabla}\phi^0_z.\utilde{\nabla}\phi^0_x + \phi^1_y\utilde{\nabla}\phi^0_z.\utilde{\nabla}\phi^0_y + \phi^1_z\utilde{\nabla}\phi^0_z.\utilde{\nabla}\phi^0_z \\
&+ \phi^1_{xz}\utilde{\nabla}\phi^0.\utilde{\nabla}\phi^0_x + \phi^1_{yz}\utilde{\nabla}\phi^0.\utilde{\nabla}\phi^0_y + \phi^1_{zz}\utilde{\nabla}\phi^0.\utilde{\nabla}\phi^0_z \\
&+ \phi^1_{zz}g) \qquad \text{(A.34)}
\end{aligned}$$

These then, are the forms of the eight components from which the iterative procedure can be constructed, expressed in terms of the approximate potential ϕ^0, and the correction to that approximation ϕ^1. All terms are linear in ϕ^1. Note that both E^0_z and E^1_z require derivatives of the potential up to third-order to be known. It is a characteristic of the desingularised discrete-source method that the task of computing such derivatives is straight-forward.

A.5 CONCLUSION

An iterative procedure has been formulated, and an algorithm for its implementation has been presented. It comprises a boundary condition, linearised in the potential, which is to be applied on an approximation to the free surface, rules for determining the new free surface and potential, and a test for convergence. It converges to the desired solution with a quadratic rate of exponential decay in error. The components of the boundary condition have been given in detail, and it is clear that third derivatives of the potential are required for its implementation.

BIBLIOGRAPHY

[1] R.F. Beck, *Time-domain computations for floating bodies*, Applied Ocean Research **16** (1994), 267–282.

[2] R.F. Beck, Y. Cao, S.M. Scorpio, and W.M. Schultz, *Nonlinear ship motion computations using the desingularized method*, Twentieth Symposium on Naval Hydrodynamics (Santa Barbara, USA), 1994.

[3] R.F. Beck and S.M. Scorpio, *A desingularized boundary integral method for fully nonlinear water wave problems*, Twelfth Australasian Fluid Mechanics Conference (Sydney, Australia), 1995.

[4] V. Bertram, W.W. Schultz, Y. Cao, and R.F. Beck, *Nonlinear computations for wave drag, lift and moment of a submerged spheroid*, Ship Technology Research **38** (1991), 3–5.

[5] Y. Cao, *Computations of nonlinear gravity waves by a desingularised boundary integral method*, Ph.D. thesis, Department of Naval Architecture and Marine Engineering, The University of Michigan, 1991.

[6] Y. Cao, W.W. Schultz, and R.F. Beck, *Three-dimensional desingularized boundary integral methods for potential problems*, International Journal for Numerical Methods in Fluids **12** (1991), 785–803.

[7] C.W. Dawson, *A practical computer method for solving ship-wave problems*, Second International Conference on Numerical Ship Hydrodynamics (Berkeley, USA), 1977.

[8] F. Dias and E.O. Tuck, *Weir flows and waterfalls*, Journal of Fluid Mechanics **230** (1991), 525–539.

[9] L.J. Doctors and R.F. Beck, *Convergence properties of the Neumann-Kelvin problem for a submerged body*, Journal of Ship Research **31** (1987), 227–234.

[10] L.K. Forbes, *Nonlinear drag-free flow over a submerged elliptical body*, Journal of Engineering Mathematics **16** (1982), 171–180.

[11] ———, *An algorithm for 3-dimensional free-surface problems in hydrodynamics*, Journal of Computational Physics **82** (1989), no. 2, 330–347.

[12] T.H. Havelock, *The propagation of groups of waves in dispersive media, with applications to waves on water produced by a travelling disturbance*, Proceedings of the Royal Society of London, Ser. A **81** (1908), 398–430.

[13] ———, *The effect of shallow water on wave resistance*, Proceedings of the Royal Society of London, Ser. A **100** (1922), 499–505.

[14] ———, *The method of images in some problems of surface waves*, Proceedings of the Royal Society of London, Ser. A **115** (1926), 268–280.

[15] ———, *The vertical force on a cylinder submerged in a uniform stream*, Proceedings of the Royal Society of London, Ser. A **122** (1928), 387–393.

[16] ———, *Wave resistance*, Proceedings of the Royal Society of London, Ser. A **118** (1928), 24–33.

[17] ———, *The wave resistance of a spheroid*, Proceedings of the Royal Society of London, Ser. A **131** (1931), 275–285.

[18] ———, *The calculation of wave resistance*, Proceedings of the Royal Society of London, Ser. A **144** (1934), 514–521.

[19] ———, *The collected papers of Sir Thomas Havelock on hydrodynamics*, Office of Naval Research, Department of the Navy, 1963, C. Wigley (ed.).

[20] D. Hendrix and F. Noblesse, *Recipes for computing the steady free-surface flow due to a source distribution*, Journal of Ship Research **36** (1992), no. 4, 346–359.

[21] J.L. Hess and A.M.O. Smith, *Calculation of nonlifting potential flow about arbitrary three-dimensional bodies*, Journal of Ship Research **8** (1964), 22–44.

[22] E. Jahnke and F. Emde, *Tables of functions*, 4th ed., Dover, New York, 1945.

[23] G. Jensen, V. Bertram, and H. Söding, *Ship wave-resistance computations*, Fifth International Conference on Numerical Ship Hydrodynamics (Hiroshima, Japan), 1988.

[24] D.C. Kring, D.A. Mantzaris, G.B. Tcheou, and P.D. Sclavounos, *A time-domain seakeeping simulation for fast ships*, Fourth International Conference on Fast Sea Transportation (Sydney, Australia), 1997.

[25] H. Lamb, *Hydrodynamics*, 6th ed., Dover, New York, 1932.

[26] M. Longuet-Higgins, *The instabilities of gravity waves of finite amplitude in deep water. II Subharmonics*, Proceedings of the Royal Society of London, Ser. A **360** (1978), 489–505.

[27] L.M. Milne-Thomson, *Theoretical hydrodynamics*, MacMillan & Co Ltd. 1960.

[28] J.N. Newman, *Swimming of slender fish in a non-uniform velocity field*, Journal of the Australian Mathematical Society, Ser. B **19** (1975), 95–111.

[29] ______, *Marine hydrodynamics*, The MIT Press, Cambridge, Massachusetts, and London, England, 1977.

[30] H.C. Raven, *A practical nonlinear method for calculating ship wavemaking and wave resistance*, Nineteenth Symposium on Naval Hydrodynamics (Seoul, Korea), 1992.

[31] ______, *Nonlinear ship wave calculations using the RAPID method*, Sixth International Conference on Numerical Ship Hydrodynamics (Iowa City, USA), 1993.

[32] J.M. Robertson, *Hydrodynamics in theory and application*, Prentice Hall, Inc. Englewood Cliffs, N.J., 1965.

[33] L.W. Schwartz, *Nonlinear solution for an applied overpressure on a moving stream*, Journal of Engineering Mathematics **15** (1981), 147–156.

[34] S.M. Scorpio, *Fully nonlinear ship-wave computations using a multipole accelerated, desingularized method*, Ph.D. thesis, The Department of Naval Architecture and Marine Engineering, The University of Michigan, 1997.

[35] D.C. Scullen, *Three-dimensional steady state nonlinear free-surface flow computation*, Gazette of the Australian Mathematical Society **23** (1996), 80–84.

[36] D.C. Scullen and E.O. Tuck, *Nonlinear free-surface flow computations for submerged cylinders*, Journal of Ship Research **39** (1995), 185–193.

[37] E.O. Tuck, *The effect of non-linearity at the free surface on flow past a submerged cylinder*, Journal of Fluid Mechanics **22** (1965), 401–414.

[38] E.O. Tuck and D.C. Scullen, *Tandem submerged cylinders each subject to zero drag*, Journal of Fluid Mechanics (1998), In press.

[39] E.O. Tuck and M.P. Tulin, *Submerged bodies that do not generate waves*, Seventh International Workshop on Water Waves and Floating Bodies (Bassin d'Essais des Carenes, Val de Reuil, France) (R. Cointe, ed.), 1992, pp. 275–279.

[40] E.O. Tuck and J.-M. Vanden-Broeck, *Waveless free-surface pressure distributions*,

Journal of Ship Research **27** (1985), 151–158.

[41] J.-M. Vanden-Broeck and J.B. Keller, *Weir flows*, Journal of Fluid Mechanics **176** (1987), 283–293.

[42] J.V. Wehausen and E.V. Laitone, *Surface waves. Handbuch der Physik*, vol. 9, Springer-Verlag, Berlin, 1960, S. Flugge (ed.).

[43] L.H. Wiryanto, *Some nonlinear shallow-water flows*, Ph.D. thesis, Department of Applied Mathematics, The University of Adelaide, 1998.

[44] G.X. Xu, *Wavemaking resistance of a group of submerged spheres*, Journal of Ship Research **40** (1996), 1–10.